№2, 2024

ISSN 2706-977X

MATERIAL AND MECHANICAL ENGINEERING TECHNOLOGY

Editorial board of the journal

Content

Ilesaliev D.I. Design of Ultrasonic Technology to Improve the Efficiency of Car Exhaust Gas Cleaning System….3
Kubich V.I., Cherneta O.G., Yurov V.M., Portnov V.S., Amangeldikyzy A., Kopobayeva A.N., Madisheva R.K., Askarova N.S. Influence of PolytronTMC Composition on the Tribological State of the System of materials "40Ch - Transmission Oil - HCh15" when Simulating Friction Modes and Lubrication Conditions………………....8
Sakhapov R. L. Method of Cleaning Internal Combustion Engine Radiator Tubes with Ultrasound………………18
Berg A.S., Nurzhanova O.A., Vytautas T., Berg A.A., Vitushenko D.V Improvement of Base Sets for Complex Configuration Parts when Assessing their Manufacturability within Industry 4.0………………………...25
Akulovich L. M., Sergeev L. E., Mendalieva S. I., Sherov K. T., Mazdubai A.V., Tussupova S.O., Ainabekova S.S The Mechanism of Orientation of Ferro-abrasive Grains in the Working Gap During Magnetic Abrasive Treatment………………………………………………………………………………………...36
Marcinkiewicz J., Spadło M., Staszak Ż.. Strength analysis by the Finite Element Method (FEM) of a modular line…………………………………………………………………………………………………….44
Pak I. Experimental Study of the Ultrasonic Muffler Efficiency for Improving the Exhaust Gas Cleaning System of Internal Combustion Engines of Automobile……………………………………………….………….53
Al-Khafaji Z., Kazem M., Radhi N., Falah M., Hadi Z. Reducing the Issues of Implements in the Human Body by Applying Hydroxyapatite (HAP) in Modern Biomedicine: Review……………………………….64
Dalavi A., Gomes A., Husain A. Weight Reduction of a Speed Reducer using Modified Particle Swarm Optimization and Shuffled Frog Leaping Algorithm………………………………………………………………79
Seitkazenova K.K, Pechersky V.N., Arapov B.R., Myrzaliev D.S., Kholmakhanov B.S. Wear Resistance Criteria for Various Types of Wear……………………………………………………………………………..91

DOI 10.52209/2706-977X_2024_2_3 **IRSTI 55.20.23** **UDC 629.021**

Design of Ultrasonic Technology to Improve the Efficiency of Car Exhaust Gas Cleaning System

Ilesaliev D.I.*
Tashkent State Transport University, Tashkent, Uzbekistan
*corresponding author

Abstract. The article investigates the problem of harmful emissions into the environment from vehicles with internal combustion engines. It describes the application of ultrasonic action for cleaning exhaust gases in order to reduce their toxicity and reduce emissions into the atmosphere. The experimental stand of ultrasonic muffler is presented, as well as the results of research confirming the effectiveness of ultrasonic action. Preliminary calculations are developed and a 3D model of the ultrasonic muffler design is created, which represents an innovative solution for improving the exhaust gas cleaning system.

Keywords: internal combustion engine, exhaust gas cleaning system, car muffler design, ultrasonic gas cleaning, ultrasonic emitter

Introduction

In today's world, road transport plays a significant role in people's daily lives, providing mobility and comfort. However, along with its benefits, it also brings significant negative consequences for the environment [1,2]. Automobiles with internal combustion engines, widespread throughout the world, are the main source of emissions of harmful substances that pollute the atmosphere and threaten human health [3,4]. This problem is particularly acute in large cities and on motorways where vehicle concentrations are high.

Exhaust gases contain hundreds of different components, many of which are toxic and lead to various chronic and severe diseases [5,6]. The existing method of internal combustion exhaust gas purification is not always reliable during long-term vehicle operation due to the limited service life of catalytic converters [7,8]. A promising approach to improve the efficiency of exhaust gas cleaning can be the application of various industrial methods such as adsorption, absorption, filtration, electropulse and ultrasonic cleaning [9,10]. However, not all of these methods can be effectively applied in exhaust gas cleaning systems due to the nature of automotive engines. To solve this problem, innovative approaches to improve the environmental friendliness of automobiles are needed. One of the promising solutions is the improvement of the exhaust gas cleaning system with the help of ultrasonic action.

Ultrasonic impact on gas is an effective method of cleaning based on the use of elastic vibrations of high frequency. This method can significantly increase the degree of exhaust gas cleaning by intensifying the process of coagulation of toxic particles [11, 12]. The use of ultrasound also allows for a more effective impact on aggressive impurities, which makes it promising for integration into the design of a car muffler [13,14].

2. Methods and Experiments

The scientific group of the Department of "Transport equipment and Logistics Systems" of Karaganda Technical University has developed an experimental stand of ultrasonic muffler, consisting of a metal case and having a total length of 2 metres and a diameter of 108 mm. This stand was made to conduct research to determine the effectiveness of ultrasonic impact on exhaust gases from cars in order to reduce their toxicity and reduce emissions into the atmosphere (Figure 1).

Fig. 1. – Experimental stand of ultrasonic muffler

A chematic diagram of a full-sized Ultrasonic Vehicle Muffler Stand is shown in Figure 2.

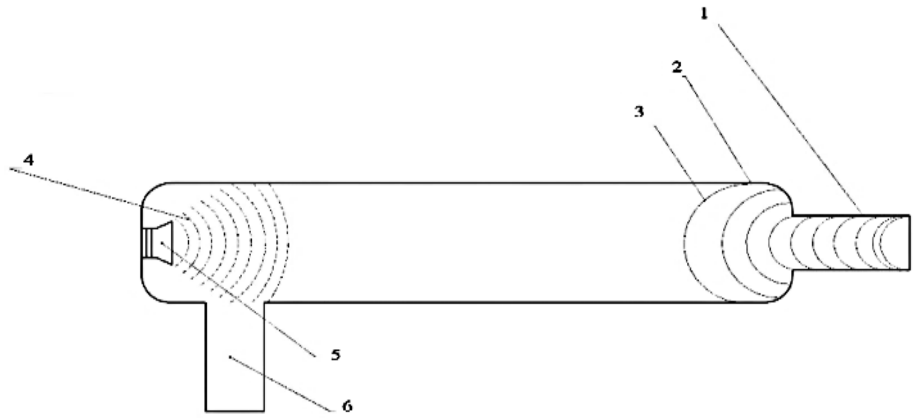

1 - exhaust gas inlet; 2 - muffler body; 3 - pressure from the side of the engine manifold; 4 - ultrasonic wave; 5 - ultrasonic emitter; 6 - exhaust pipe.

Fig. 2. – Schematic diagram of a full-sized Ultrasonic Vehicle Muffler Stand

The stand consists of ultrasonic equipment, namely an ultrasonic generator and an ultrasonic emitter (Figure 3).

Fig. 3. – Ultrasonic equipment of the experimental stand

Experimental research was carried out in the laboratory of the department of "Transport Equipment and Logistics Systems". Experiments on ultrasonic car muffler were conducted with and without ultrasonic equipment for a minute each, at different crankshaft speeds (1200, 1400, 1600 rpm) on the car VW Passat B3 with an engine capacity of 1800 cc. and the use of petrol as fuel. After 60 seconds of muffler operation without and with ultrasonic action, gas analyser readings were taken. The exhaust gas was directed to the ultrasonic muffler through the inlet pipe under pressure, depending on the values of engine crankshaft speed. In the muffler, when the ultrasonic equipment was switched on, the exhaust gas was affected by ultrasonic waves of longitudinal direction. This resulted in ultrasonic intensification of the coagulation and exhaust gas cleaning processes by increasing the particle size at the particulate gas collection point. The purified exhaust gas was discharged through the outlet pipe.

3. Results and discussion

The experimental results are summarised in Table 1.

Table 1. Experimental results

Indicators	Engine crankshaft speed (rev/min)					
	1200		1400		1600	
	Without ultrasound	With ultrasound	Without ultrasound	With ultrasound	Without ultrasound	With ultrasound
Oxygen (O_2), %	17,11	17,41	17,75	17,97	18,23	18,36
Carbon monoxide (CO), %	0,31	0,22	0,36	0,32	0,51	0,47
Gas moisture (%)	46	51	53	56	57	58

Based on the results obtained, graphs of changes in oxygen, carbon monoxide and gas moisture indices as a function of changes in engine crankshaft speed were drawn up (Figures 4-6).

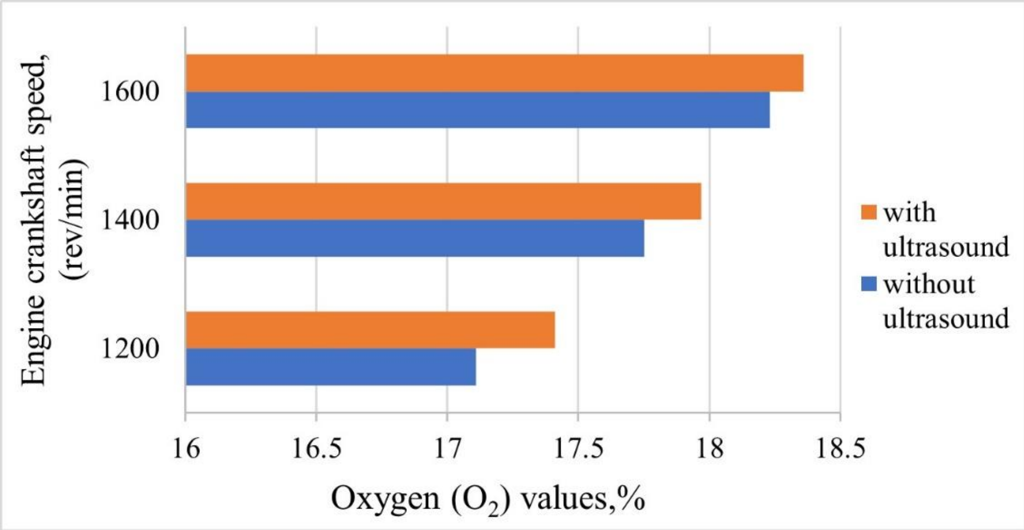

Fig. 4. – Changes in oxygen values (O_2) without exposure and with ultrasound

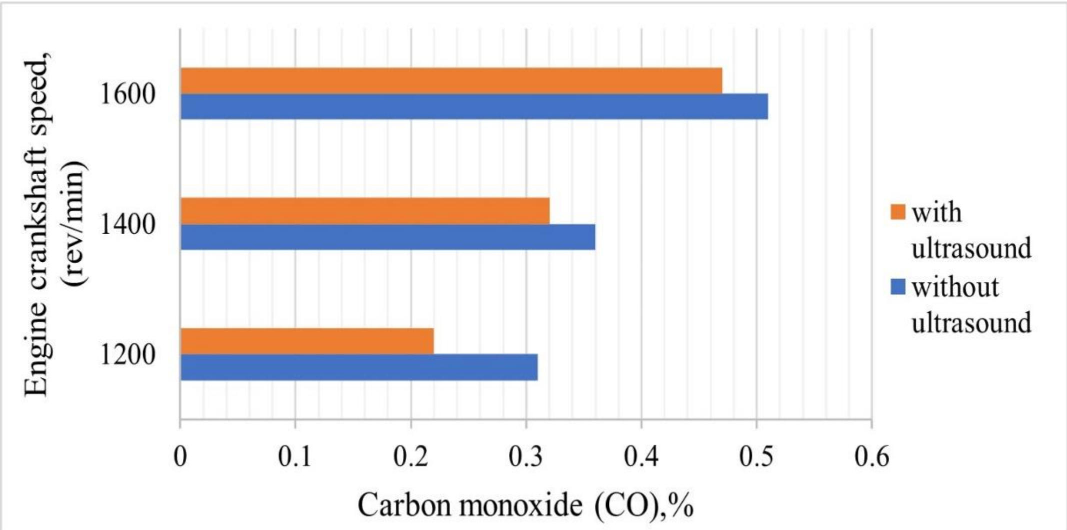

Fig.5. – Changes in carbon monoxide (CO) without exposure and with ultrasound

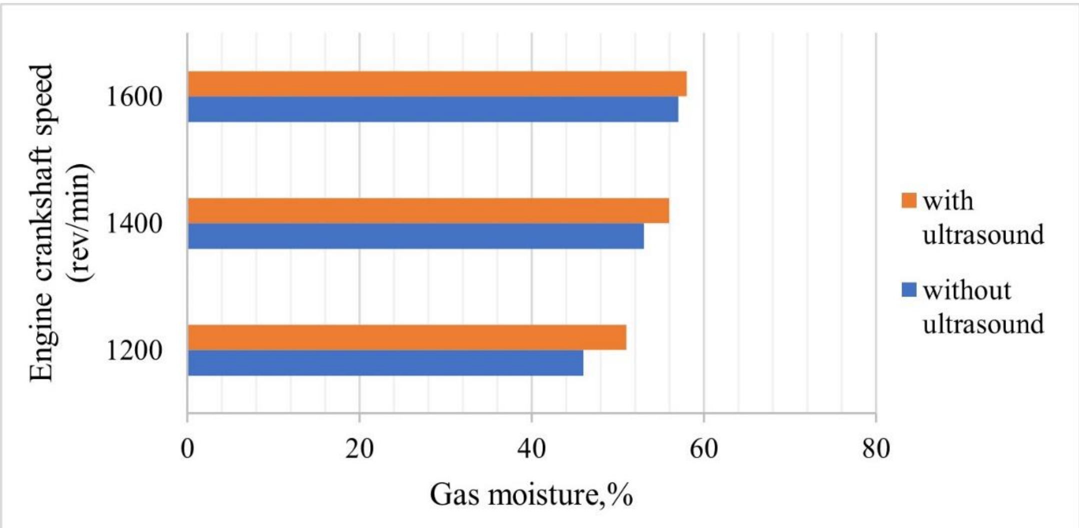

Fig.6. – Changes in gas moisture without exposure and with ultrasound

According to the graphs in Figures 4-6, the effect of ultrasound on the gas leads to a decrease in carbon monoxide content and an increase in oxygen content and moisture content. These changes are due to the mechanical effect of ultrasound on the gas molecules. The increase in the rate of coagulation between harmful gas particles caused by the effect of ultrasound promotes exhaust gas cleaning, resulting in an increase in oxygen and a decrease in carbon monoxide. In addition, the ultrasonic effect also increases the temperature of the gas, resulting in an increase in its moisture content. These indicators indicate the effectiveness of ultrasonic action on the exhaust gas and makes it possible to develop ultrasonic mufflers for the exhaust gas cleaning system of internal combustion engines.

Based on the experimental results obtained, which confirmed the feasibility and applicability of ultrasound for cleaning exhaust gases, we developed the design of ultrasonic muffler. Preliminary calculations of the main parameters of its design were carried out, the results of which are presented in Table 2.

Table 2. Main design parameters of the ultrasonic muffler

№	Design parameters	Units of measurement	Values
1	Muffler volume	m^3	0,015
2	Muffler length	m	0,4
3	Muffler diameter	m	0,21

According to the obtained calculated values of the main design parameters of the ultrasonic muffler, its 3D model was developed (Figure 7).

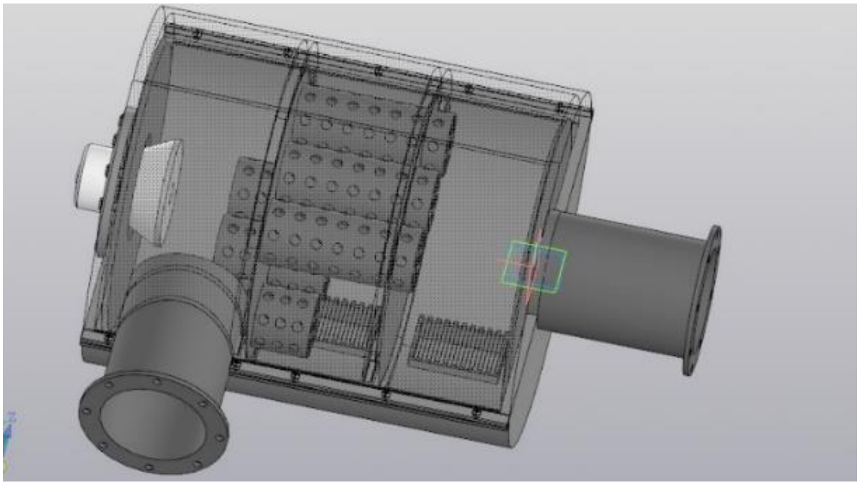

Fig.7. –3D model of the ultrasonic muffler design

The presented "3D model" of the ultrasonic muffler is a general design solution to improve the operation of the exhaust gas cleaning system of internal combustion engines.

Conclusion

On the basis of the conducted research, a conclusion was formed about the significant potential of ultrasonic impact to reduce the toxicity of exhaust gases and reduce their impact on the environment. Experimental results show that the application of ultrasound helps to increase the oxygen content and humidity in the gas stream, as well as reducing the concentration of carbon monoxide, which indicates the effectiveness of ultrasonic action. Predagayuemaya design ultrasonic muffler is an innovative solution, the use of which is appropriate for modernising the design and improving the operation of exhaust gas cleaning systems in cars with internal combustion engines. In general, the results of research confirm the prospects of application of ultrasonic technology in the automotive industry in order to reduce the negative impact on the environment.

References

[1] Kozina A., Radica G., Nizetic S. Analysis of methods towards reduction of harmful pollutants from diesel engines //Journal of Cleaner Production, Vol. 262, Issue 121105, 2020. – P. 1-20

[2] Pak I., Kadyrov A., Askarov B., Suleyev B., Karsakova A. Developing and studying the method of ultrasonic purification and utilization of internal combustion engine exhaust gases //Communications - Scientific Letters of the University of Zilina, Vol. 25, Issue 3, 2023. – P. 245-258

[3] Kukesheva A., Kadyrov A., Kryuchkov Y. Establishing the parameters of the operation mode of the electric pulse automobile muffler //Journal of Applied Engineering Science. Vol. 22, Issue 1, 2024. – P.89–99

[4] Yessenbayeva A., Kadyrova I, Aukenov N., Shaimardanov N. Apsalikov B., Massabayeva M., Kazymov M., Shakhanova A., Mussazhanova Zh., Biomarkers of immunothrombosis and polymorphisms of IL2, IL6, and IL10 genes as predictors of the severity of COVID-19 in a Kazakh population //PLoS ONE, Vol. 18, Issue 6, 2023. – P. 61-67

[5] Akhmaltdinova L., Korshukov I., Kolesnikova Ye., Kolesnichenko S., Babenko D., Kadyrova I., Kabildina N., Sirota V., Zhumaliyeva V., Taizhanova D., Vazenmiller D., Turmukhambetova A. Association of four genetic variants with colorectal cancer in Kazakhstan population //Oncotarget, Vol. 12, Issue 21, 2021. – P. 2215-2222

[6] Korshukov I., Barkhanskaya V., Sultanbekova A., Kadyrova I., Kolesnichenko S., Kolesnikova Ye., Babenko D. SARS-COV-2 detection in MALDI-TOF mass spectra by machine learning. // AIP Conf. Proc., Vol. 2872, Issue 1, 2023. – P. 1-13

[7] Pak I., Baurova N., Kurmasheva B., Karsakova A., Kadyrova I. Technical and Economic Efficiency of Devices for Ultrasonic Cleaning of City Bus Exhaust Gases //Bulletin of L.N. Gumilyov Eurasian National University Technical Science and Technology Series. Vol.139, Issue 2, 2022. – P. 133–142

[8] Kyzylbaeva E.Zh., Kukesheva A.B., Kunaev V.A. Mathematical model of plate movement in thixotropic mud // Material and Mechanical Engineering Technology, Vol. 2, Issue 2, 2020. – P. 26-30

[9] Kadyrov A., Kryuchkov Ye., Sinelnikov K, Ganyukov A., Sakhapov R., Kukesheva A. Studying the process of the internal combustion engine exhaust gas purification by an electric pulse // Communications - Scientific Letters of the University of Zilina, Vol. 24, Issue 4, 2022. – P. 275-287

[10] Kadyrov A., Kukesheva A., Kryuchkov Ye., Pak I., Kurmasheva B, Kabikenov S. Development of Calculation Methodology for Optimizing the Operating Mode of an Electric Pulse Unit for Cleaning Exhaust Gases //Communications - Scientific Letters of the University of Zilina, Vol. 26, Issue 1, 2024. – P. 41-53

[11] Kadyrov A., Sarsembekov B., Ganyukov A., Suyunbaev Sh., Sinelnikov K. Ultrasonic unit for reducing the toxicity of diesel vehicle exhaust gases //Communications - Scientific Letters of the University of Zilina, Vol. 24, Issue 3, 2022. – P. 189-198

[12] Kadyrov A., Kurmasheva B., Suyunbaev Sh., Sinelnikov K., Sakhapov R., Ganyukov A. Studying the process of transport equipment cooling system ultrasonic cleaning //Communications - Scientific Letters of the University of Zilina, Vol. 24, Issue 4, 2022. – P. 288-300

[13] Kadyrov A., Bembenek M., Sarsembekov B., Kukesheva A., Nurkusheva S. The Influence of the Frequency of Ultrasound on the Exhaust Gas Purification Process in a Diesel Car Muffler //Appl. Sci. Vol.14, Issue 12, 2024. – P. 1-19.

[14] Kadyrov A., Sarsembekov B., Ganyukov A., Zhunusbekova Z., Alikarimov K. Experimental research of the coagulation process of exhaust gases under the influence of ultrasound //Communications - Scientific Letters of the University of Zilina, Vol. 23, Issue 4, 2021. – P. 288-298

Information of the author

Ilesaliev Daurenbek Ikhtiyarovich, d.t.s., professor, Tashkent State Transport University
e-mail: ilesaliev@mail.ru

DOI 10.52209/2706-977X_2024_2_8 **IRSTI 55.09.81** **UDC 621.762**

Influence of Polytron^{TMC} Composition on the Tribological State of the System of materials "40Ch - Transmission Oil - HCh15" when Simulating Friction Modes and Lubrication Conditions

[1]Kubich V.I., [2]Cherneta O.G., [3]Yurov V.M., [1]Portnov V.S., [4]Amangeldikyzy A.*, [4]Kopobayeva A.N., [4]Madisheva R.K., [4]Askarova N.S.

[1]National University "Zaporozhye Polytechnic", Zaporozhye, Ukraine
[2]Dnieper State Technical University, Kamenskoye, Ukraine
[3]Vostok LLP, Karaganda, Kazakhstan
[4]Abylkas Saginov Karaganda Technical University, Karaganda, Kazakhstan
*corresponding author

Abstract. In this work, definitive tribological tests were carried out on the material system "40Ch - gear oil - HCh15" to assess the nature of the action of the additional composition POLYTRON$^{\mathbf{MTC}}$ for its adaptability to high-speed, power loading conditions and the ability to form reliable lubricating formations in conditions of insufficient lubrication. Physical modeling of the manifestation of friction in the upper boundary of boundary lubrication with a friction coefficient of $0.12 \leq \mu_g \leq 0.2$, as well as semi-dry and dry friction was performed. It was established that high contact pressures in the range from 4.2 MPa to 8.6 MPa at the beginning of running-in created features of resistance to the flow of oil components into the zones of the contour areas of friction interaction, which determined to a greater extent mechanical metal connections when sliding with a sufficiently high coefficient of friction $\mu c = 0.3\text{-}0.7$. In this case, the conditional point contact at sliding speeds determined the number of oil molecules that were directed to the diffuser contact zone, i.e. behind the ball along the friction path on the surface of the rotating disk. A fundamental difference in the manifestation of POLYTRON^{MTC} was revealed when it is added to Opet Fullgear FRM 75W-80, CastrolSyntraxUniversal 80W-90 oils, which have a synthetic base, and Castrol ATF MultiVehicle 75W-80 oil, which has a mineral base. Graphic patterns of changes in friction and wear characteristics have been constructed for the model conjugation "moving disk-fixed ball".

Keywords: transmission oil, dynamic coefficient of friction, temperature, pressure, test time, ball, disk, lubricant formations

Introduction

Oils used in machine units and mechanisms are often subjected to heavy loads, especially during cyclic start-stop operation, which leads to high temperatures and pressures. This leads to unacceptable damage to the working surfaces and, accordingly, to catastrophic failures. The reduction in thermomechanical stress in the contact interaction zones of the surfaces of parts that operate when changing lubrication modes is determined by a number of factors. One of them is the recommended use of additive compositions (AC) in transmission oils for the lubrication of industrial engineering parts, for example, gear transmissions of automobiles and tractors. The list of such ACs is quite wide, and each of the proposed compositions differs in the content and direction of manifestation of the implemented mechanisms for reducing friction and wear [1-4]. Nanoparticles have become a new type of composition due to their size, shape and other properties. A significant number of researchers have noted that the addition of nanoparticles, such as MoS_2 and SiO_2 nanoadditives to lubricant compositions, effectively reduces wear and friction [3, 5, 6].

Recommendations from DC manufacturers do not fully take into account the possible features of the manifestation of their tribological action when changing loading and lubrication modes in standard mechanisms of mechanical engineering objects, for example, in the same gears. Indicators of lubricity and tribological characteristics of oils are determined using standard methods [9]. At the same time, the contact geometry and simulated conditions do not always correspond to the operational geometry of the contact of real friction pairs. Based on the establishment of patterns of changes in the characteristics of the tribological state of known systems of structural metals that operate in extreme loading and lubrication modes from the used DCs, it seems to be a relevant scientific and technical task considered in tribology. In this case, the emphasis should be on determining the ability of DC to significantly improve the antifriction and antiwear properties of lubricants, which can be obtained using conventional manufacturing technology.

Process fluid POLYTRON^{MTC} is one of the representatives of DC [7]. MTC (Metal Treatment Concentrate) is a petroleum-based metal treatment concentrate, which is recommended to be added to transmission oils for lubrication systems of units and mechanisms [8]. As a result of micrometallurgical processes occurring at the peaks of irregularities, the thinnest layers of the base metal are transformed into a new type of metal, which is much harder and has significantly greater wear resistance. This secondary layer protects the main softer metal from wear [7]. With this mechanism, a certain role will be played by base oil molecules, which, depending on their origin, have different structures and polarities. Based on the above, contact pressure and the structure of the base oil seem to be the main factors in the manifestation of the active action of Polytron^{MTC}. An advertising demonstration of the lubrication capabilities of the above-mentioned POLYTRON^{MTC} DC comes down to setting up an experiment on a friction pair "rotating disk - stationary cylindrical roller", which contact through the tested lubricant compositions when the disk is partially immersed in them [10]. In this case, the rotational resistance is determined using a dial ammeter, and loading is carried out with a torque wrench-loader, which does not make it possible to obtain a more detailed and objective picture of the manifestation of the lubrication effect behind the classical friction coefficient when changing the rotation speed. This is especially important to know and understand when it comes to high contact loads when changing lubrication modes. This approach is used by a number of researchers, for example in [11], the mechanism of tribofilm formation and destruction was carefully monitored by monitoring the friction coefficient throughout the test. Tribological tests carried out with limited amounts of lubricant showed a direct relationship between the amount of lubricant and the time it takes for the tribofilm to break down, with tests with less amount of lubricant showing shorter life. In [12], the authors evaluate the severe operating conditions of sliding surfaces in some modes in which self-organization processes on friction surfaces are ineffective. This negatively affects the continuity and resistance of the resulting lubricating formations to destruction, and it is under such conditions that the lubrication effects need to be improved. In work [13], the authors carried out definitive tribological tests of the material systems "CuCrNiZrTi- 85W90 – 40Ch", "CuCrNiZrTi- 85W90 - KCh50" to assess the nature of the manifestation of the action of DC ABRO GT-409 and POLYTRON^{MTC} in them on adaptability to loading and lubrication modes, the manifestation of parameters of adhesive properties when modeling shear on small-sized samples. It has been established that a more significant influence on the reduction in the parameters of adhesive properties is exerted by the POLYTRON^{MTS} components, which cause the formation of secondary lubricating formations with denser structures at the adhesion boundary with metal surfaces and reduced resistance to movement within the formed cohesive bonds between them. The claimed uniqueness of enhancing the lubricating effect of ordinary lubricants and the formation of secondary wear-resistant structures on metal surfaces [7, 8, 10] when using POLYTRON^{MTS} predetermines the need for further more applied tribological tests. This will make it possible to supplement recommendations for its use based on the characteristics of operating modes and operating conditions of specific friction pairs of mechanisms and machine units.

The purpose of the work is to determine the effect of the POLYTRON^{MTC} composition when added to transmission oils of various viscosity classes and bases on the pattern of changes in the characteristics of the tribological state of the interface "rotating disk - transmission oil - stationary ball" during physical modeling of high-speed, force loading on lubricant formations that form on friction surfaces under various lubrication conditions.

1. Research methodology

The physical modeling of the tribological state is based on the preliminary formation of lubricating formations on the metal surfaces of small-sized samples from transmission oils of different viscosity classes with the addition of the POLYTRON^{MTS} composition with abundant lubrication of the contact zone, followed by their stepwise loading to the boundary conditions of lubrication in the absence of additional oil supply to the friction zone. This mode is considered as a type of lubricant film starvation, when the concentrated volume of lubricant is not enough to replenish layers of lubricant formations that are destroyed by friction. This approach simulates contact interaction modes when parts move relative to each other at the beginning of power flow transmission, when there is no full-fledged process of supplying lubricant to friction zones. This is especially significant when there are large contact normal pressures with a tangential component, which certainly destroy lubricant formations and the material of the working surfaces of parts. The addition of the POLYTRON^{MTC} composition in accordance with the manufacturer's recommendations was 10% of the volume of oils for manual transmissions and 5% for automatic transmissions [7], and was aimed at the formation of lubricating formations with significantly improved anti-wear and anti-friction characteristics. To determine the nature of the influence of the POLYTRON^{MTC} composition on the tribological state of model tribocouplings, depending on the basis and viscosity of the interaction medium in a certain mode of contact interaction of friction surfaces, transmission oils were selected and used, the performance characteristics of which are given in Table 1.

Table 1. Characteristics of transmission oils

Oil name	Brief characteristics of the oil	Density ρ at 15 ^{0}C	Kinematic viscosity γ at 40 ^{0}C, mm^2/s	Kinematic viscosity γ at 100 ^{0}C, mm^2/s	Viscosity index
Castrol ATFMultiVehicle 75W-80	synthetic, for highly loaded manual transmissions of vehicles	0,87	40	7,5	159
OpetFullgear FRM 75W-80	synthetic, for manual transmissions and highly loaded vehicle gearboxes	0,857	58,2	9,8	153
CastrolSyntrax Universal 80W-90	mineral, for automatic transmissions, power steering of vehicles	0,893	168	17,0	108

Tribotechnical tests were carried out on a SMC-2 machine according to the "rotating disk - stationary ball" friction scheme in a cycle consisting of two stages, Figure 1 a. Stage No. 1 - test with abundant lubrication. Stage No. 2 – testing on pre-created lubricating formations without additional oil supply. After the first stage, the oil drained from the surface of the disk, and its excess amount was removed by soaking with felt paper. At each stage, the friction moment and temperature were recorded, and the wear rate was calculated based on the result of the integral wear of the ball at two stages. The disk rotation frequency was 300 min-1 and 1000 min-1. The normal load on the moving contact changed stepwise and was 13N, 22N, 45N, 67N, 90N, 115N, 140N, 160N, 180N. The holding time at the indicated normal loads was 2 minutes. With a sharp increase in movement resistance, as indicated by the friction machine recorder, the experiment stopped. The rotating disk was installed on the lower shaft of the friction machine, had dimensions of diameter d=50 mm, width b=12 mm and was made of steel 40X with a hardness of 42-46 HRC, Figure 1 f. A ball with a diameter of d=9.3 mm was made of steel HCh 15 , with a hardness of 55-60 HRC, was fixed by gluing a disk into the blind holes, which was fixedly mounted on the upper shaft of the friction machine, Figure 1 b-d, f. The choice of materials for small-sized samples and hardness is due to the similarity with materials that are used for the manufacture of gears, for example, for mechanisms and transmission units of cars and tractors.

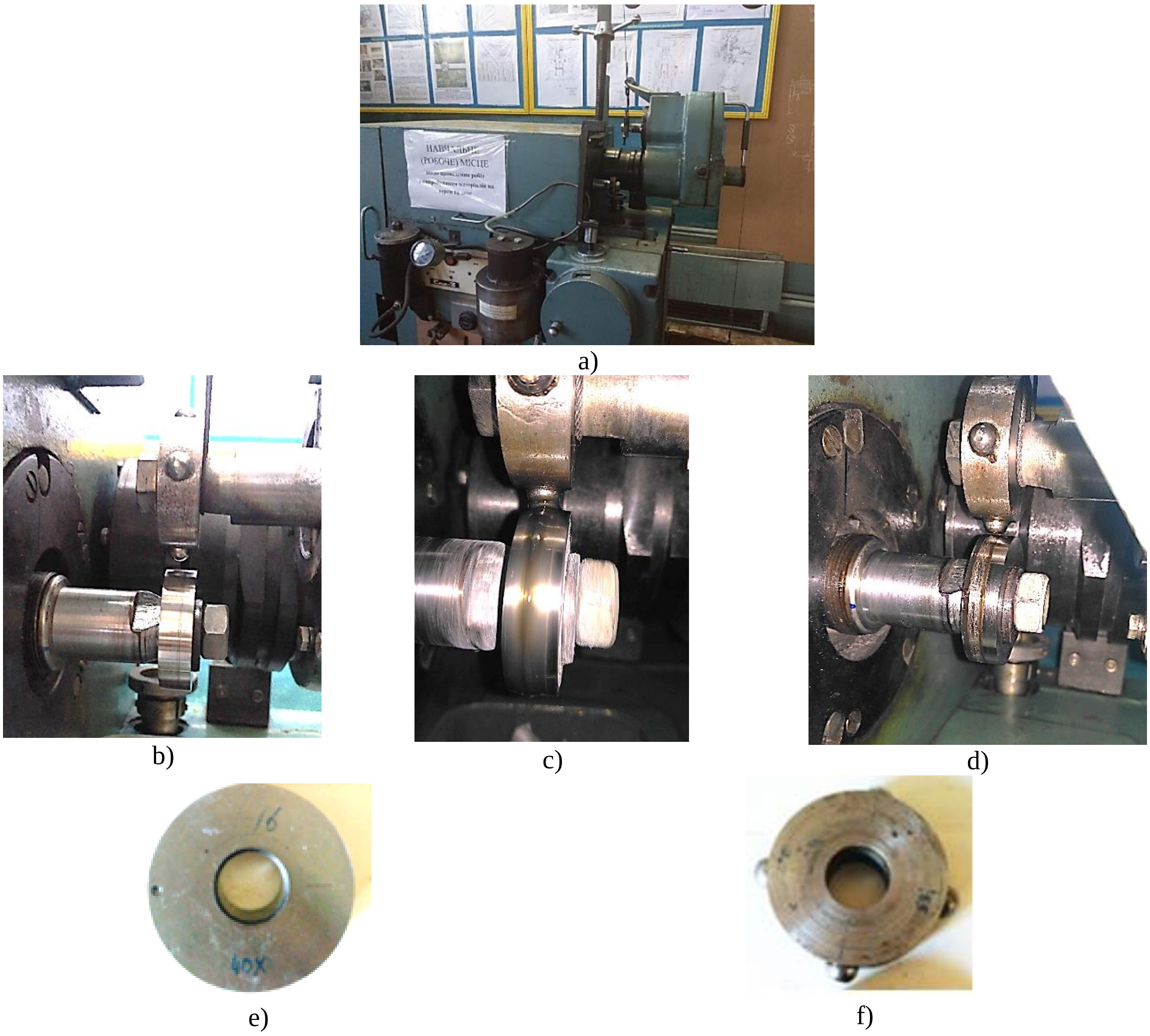

Fig. 1. Methodological support for experimental tests:
(a) – general view of the SMC-2 friction machine with additional equipment;
(b) – contact of sample surfaces without oil; (c) – contact of sample surfaces when lubricated with oil; (d) – contact of sample surfaces when the surface of a rotating disk is damaged; (e) – rotating disk;
(f) - a stationary disk with balls.

To assess the tribological state, the following characteristics were used:

- dynamic friction coefficient μ (hereinafter referred to as friction coefficient), as a criterion for changing the antifriction properties of lubricating formations and their ability to operate at maximum contact pressure conditions;
- the intensity of wear of the ball surface, as an indirect criterion of the ability of lubricating formations to resist their own destruction and counteract mechanical wear of the ball surface;
- volumetric temperature of the zone of interaction of the ball with the surface of the disk, as a criterion for assessing the general temperature state of the friction pair.

The friction coefficient was determined by the friction moment from tribograms in accordance with the load in contact and the geometric size of the roller according to expression (1), the calculation accuracy was: $\Delta\mu = 0.003$.

$$\mu = \frac{M_t}{N * r} . \qquad (1)$$

where M_t - friction moment, N m, 1 grid division of the tribogram field was 0.18 0.001 N m;
r - disk radius, m;
N – normal load, N.

The number of experiments for each of the gear oils shown in Table 1 was n=3. To evaluate the proposed characteristics using the graphic-analytical method, arithmetic mean values of the physical quantities under study were used. The wear rate of the ball surface was determined by the geometric parameters of ball wear along the friction path in accordance with expression (2). In this case, the wear rate is considered as a reduced reduction in the diameter of the ball to the plane of its wear.

$$I_S = \frac{S_1 - S_2}{2\pi r \cdot t \cdot n}. \quad (2)$$

where S_1 - value of the area before the experiment, mm^2;
S_2 - area values after the experiment, mm^2;
t – hour of the experiment, min;
r – disk diameter, m;
n – rotation frequency of the friction machine shaft, min^{-1}.

To determine the degree of ball wear when testing oils, prints of the ball wear area on a horizontal surface were used. In this case, the areas of the prints before and after the experiments were taken into account. To carry out this operation, the method of pressing the ball through tracing paper onto the surface of graph paper was used. Based on the results of determining the areas of indentations under corresponding normal loads, normal contact pressures were calculated. At the same time, under loads of 11N-45N, the standard deviation of the contact pressure was σ_p=1.2 MPa, that is, 8% of the average design pressures. At loads of 67N-180N, the standard deviation of the contact pressure was σ_p=3.9 MPa, i.e. 11% of calculated average pressures. Within the specified deviations, the wear area of the ball changed with each stepwise increase in the normal load. Thus, it was possible to estimate the contact pressure in the friction zone. The temperature state of the contact was determined in a non-contact manner using a Wintact WT319B infrared pyrometer with a measurement temperature of up to 600 °C and was assessed by the average values of the following indicators, Figure 2:

- rate of temperature increase υ_T, $^0C\ min^{-1}$;
- temperature at the end of the heavy lubrication experiment T_{max}, ^0C;
- relative temperature difference according to lubrication conditions ΔT, ^0C.

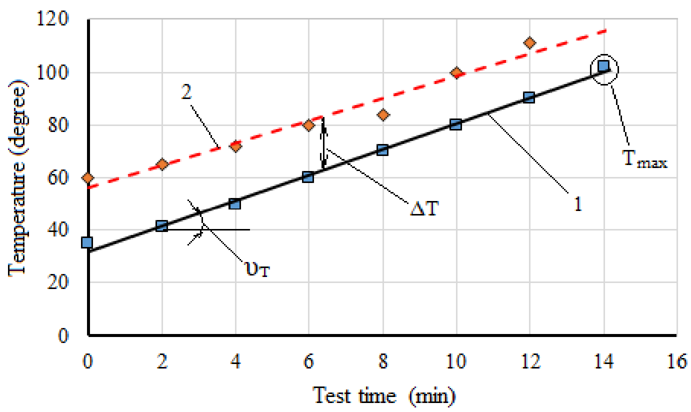

1 - tests with abundant lubrication; 2 - tests on formed lubricating formations without additional oil supply

Fig. 2. - Indicators for assessing the temperature state of the contact

Since the patterns of changes in the temperature state obeyed linear patterns, their graphical form was not given, and only the indicated indicators were considered.

2. Results and discussion

As a result of processing the obtained tribograms using Microsoft Excel Worksheet and Paint applications, graphical patterns of changes in the dynamic coefficient of friction (Figures 3-5) and the wear rate of ball samples depending on the viscosity of the transmission oil (Figure 6) were constructed using arithmetic average values.

In general, based on the simulated lubrication conditions and test conditions for load and sliding speed, the following was determined. Firstly, there is a manifestation of boundary friction according to lubrication conditions in the upper limit limit (0.01-0.08) ≤ μ_g ≤ (0.1-0.15) and semi-dry friction. High contact pressures from 4.2 MPa to 8.6 MPa created conditions of resistance to the flow of oil components into the contour areas of friction interaction, which largely determined the mechanical metal connections during sliding with a fairly high coefficient of friction of 0.3-

0.7. In this case, the conditional point contact at sliding speed determined the number of oil molecules that were directed to the diffuser contact zone, that is, behind the ball along the friction path.

Secondly, there was an achievement of a constant friction regime by stabilizing the friction coefficient in the range of 0.12-0.22, but no stabilization of the temperature state was observed. During the experiments, the temperature constantly increased at average rates from 1.5 ^{0}C min^{-1} to 5 ^{0}C min^{-1}, and ranged from 24 ^{0}C to 120 ^{0}C. This indicated the incompleteness of the processes of adaptability of the surface structures of the sample materials and the interaction environment to an energetically favorable direction.

Thirdly, it has been determined that in some cases, a simulated contact made from the materials under study is capable of operating on the created lubricating formations without additional oil supply, but with increased resistance to movement. At the same time, the Polytron^{MTC} DC can both positively and negatively influence friction stabilization in the presence of boundary lubrication components that are concentrated and retained in the microprofiles of the contact surfaces. This indicated that the use of Polytron^{MTC} DC is compatible with all transmission oils on a basic basis, as stated by the manufacturer. However, there are peculiarities in the manifestation of the properties of DC when it is added to mineral and synthetic oils, since Polytron^{MTC} DC (hereinafter referred to as DC) appears to be a completely petroleum-based mixture [7].

2.1 Tribological state of a model tribological coupling, which was tested with synthetic gear oil Opet FullgearFRM 75W-80

The patterns of change in the friction coefficient shown in Figure 3 indicate the following.

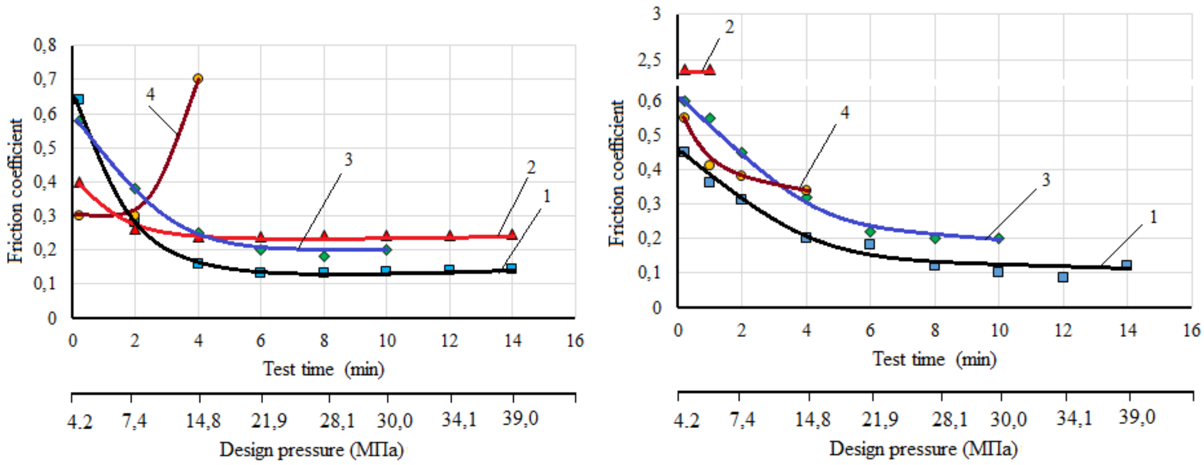

a) b)

1 – tests with heavy lubrication, n=300 min^{-1}; 2 – tests on formed lubricating formations without additional oil supply, n=300 min-1; 3 - tests with abundant lubrication, n=1000 min^{-1}; 4 - tests on formed lubricating formations without additional oil supply, n=1000 min^{-1}

Fig. 3. - The influence of load and rotation speed on the friction coefficient of a model tribocoupling when testing OpetFullgear FRM 75W-80 oil: a – tribological contact without DC; b - tribological contact with DC

When tested under conditions of abundant lubrication, persistent lubricating layers are formed on the friction surfaces between the surfaces, which are run-in for 6 minutes without DC, and for 8 minutes with DC, reaching a constant friction coefficient μ=0.12 at a rotation speed of n=300 min^{-1} and μ=0.2 at a rotation speed of 1000 min^{-1}. That is, there was no significant effect of DC on the change in the tribological state.

When tested without additional oil supply without DC, a constant friction process is observed from 4 min. tests at rotation speed n=300 min^{-1} with reaching a constant friction coefficient μ=0.22. However, at a frequency of n=1000 min^{-1}, from the second minute there was a rapid increase in the friction coefficient to μ=0.7, and the experiments were stopped. In this case, a constant friction process took place with a friction coefficient μ=0.3. Tests with DC at a frequency of n=300 min^{-1} did not result in a friction reduction effect; there was a fairly high but stable friction coefficient μ=2.5, which caused catastrophic wear of the ball sample, and the experiments stopped in the second minute. However, an increase in frequency to n=1000 min^{-1} caused a slight decrease in friction and the ability to operate a model tribocoupling with a decrease in the friction coefficient from 0.55 to 0.32. At the fourth minute the experiments stopped. This effect is explained by the creation of current conditions for the occurrence of hydraulic lift in the contact zone.

According to the indicators of the temperature state given in Table 2, no significant changes were observed, with the exception of an increase in the rate of temperature increase by 1.4 times at a frequency of n=300 min-1 with the addition of DC.

Table 2. Temperature indicators when testing Opet Fullgear FRM 75W-80 oil

	without DC	with DC

Rotation speed n, min^{-1}	υ_T, ^{0}C хв$^{-1}$	T_{max}, ^{0}C	ΔT, ^{0}C	υ_T, ^{0}C·хв$^{-1}$	T_{max}, ^{0}C	ΔT, ^{0}C
300	1,4	50	6	2	55	15
1000	5	100	20	5	60	20

In terms of wear intensity, the values are given in Table 3, there are differences that are due to both the suspension of experiments with obvious jumps in resistance to movement on the recorder, and the manifestation of the addition of DC. Apparently, DC significantly reduces friction and wear at a frequency of n=1000 min^{-1}, but does not work at n=300 min^{-1}.

Table 3. Wear rate Is of the ball sample, 10^{-10} m

Rotation speed n, min^{-1}	without DC	with DC
300	0,4	25,3
1000	31,8	4,9

2.2 Tribological state of a model tribological coupling, which was tested with Castrol Syntrax Universal 80W-90 synthetic gear oil

The patterns of change in the friction coefficient shown in Figure 4 indicate the following.

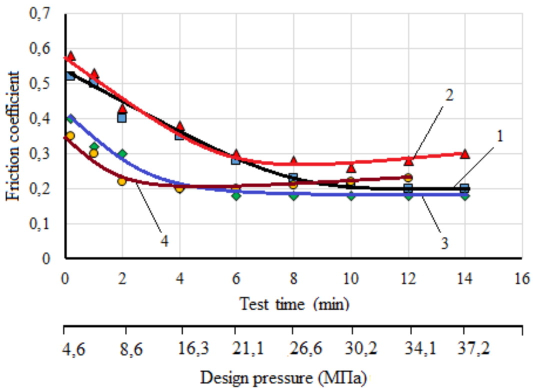

a)

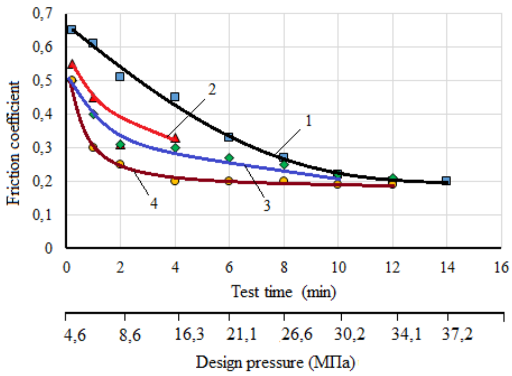

b)

1 – tests with abundant lubrication, n=300 min^{-1}; 2 – tests on formed lubricating formations without additional oil supply, n=300 min^{-1}; 3 - tests with abundant lubrication, n=1000 min^{-1}; 4 - tests on formed lubricating formations without additional oil supply, n=1000 min^{-1}

Fig. 4. - The influence of load and rotation speed on the friction coefficient of a model tribocoupling when testing CastrolSyntraxUniversal 80W-90 oil:a – tribological contact without DC; b - tribological contact with DC

When tested under heavily lubricated conditions, thinner lubricating layers are formed on the friction surfaces compared to Opet Fullgear FRM 75W-80 oil. Depending on the rotation speed and the presence of DC, the surfaces of the samples are not run in equally. In this case, the output of the tribocoupling to a constant friction coefficient, which had a value of $\mu \approx 0.2$ without DC at n=300 min^{-1}, is 10 minutes, with DC – 12 minutes. At the same time, at a rotation speed of n=1000 min^{-1} without DC, the running-in time was 4 minutes, and with DC, reaching a constant coefficient was not determined. This is explained by the viscosity-temperature properties of the tested oil, since its viscosity index is significantly lower than that of OpetFullgear FRM 75W-80 oil, Table 1 (108-153), although Castrol Syntrax Universal 80W-90 oil is higher in viscosity class. The mechanical properties of the lubricating formations that are formed in this case are not sufficient to resist the convergence of surfaces to provide boundary lubrication with a low coefficient of friction. The addition of DC delays the running-in of surfaces at low rotation speeds, and causes dispersion of oil molecules at the peaks of microprofiles at high rotation speeds , causing lubricant-depleted contact between metal surfaces. And as a consequence of what has been described, there is a greater coefficient of friction. Thus, for 4 minutes of testing tribocoupling with a DC at a rotation speed of n=1000 min^{-1}, the friction coefficient had a value of 0.3, and without a DC – 0.2, respectively.

When tested without additional oil supply without adding DC, the stable process of boundary friction was short-lived and was observed within 2 minutes. At a disk rotation frequency n=300 min^{-1}, a constant friction coefficient μ=0.27 occurred from the 6th minute of testing. At a disk rotation frequency n=1000 min^{-1}, a constant friction coefficient μ=0.2 was observed from 3 minutes of tribocoupling tests. Subsequently, the movement resistance gradually increased, and the rate of increase in the friction coefficient was 0.005 min^{-1}. The addition of DC ensured, starting from the 4th minute of the experiments, a steady process of contact interaction with a friction coefficient of μ=0.2. That is, DC created the conditions for the formation of more reliable lubricating formations capable of withstanding an increase in contact pressure in the friction zone.

According to the indicators of the temperature state given in Table 4, no significant changes were observed, with the exception of an increase in the rate of temperature growth by 1.4 times at the rotation speed of the disk sample n = 300 min^{-1} with the addition of DC. This condition was also observed for Opet Fullgear FRM 75W-80 oil.

Table 4. Temperature indicators when testing Castrol Syntrax Universal 80W-90 oil

Rotation speed n, min^{-1}	without DC			with DC		
	υ_T, ^{0}C хв$^{-1}$	T_{max}, ^{0}C	ΔT, ^{0}C	υ_T, ^{0}C хв$^{-1}$	T_{max}, ^{0}C	ΔT, ^{0}C
300	1,2	52	3	1,7	60	15
1000	5	100	25	5	80	20

According to the wear rate of the ball sample, the value of which is given in Table 5, the addition of DC causes an increase in wear rate by 2.1 times and 3.6 times at the corresponding test frequencies. Since this test time characteristic is integral, greater wear, based on the graphical dependencies (Figure 4b), appeared in the period from the beginning of the experiments to 8 minutes of testing.

Table 5. Wear rate Is of the ball sample, 10^{-10} m

Rotation speed n, min^{-1}	without DC	with DC
300	3,7	7,8
1000	3,0	10,7

2.3 Tribological state of a model tribological coupling, which was tested with synthetic gear oil CastrolATFDexronIIMultiVehicle 75W-80

The patterns of change in the friction coefficient shown in Figure 5 indicate the following.

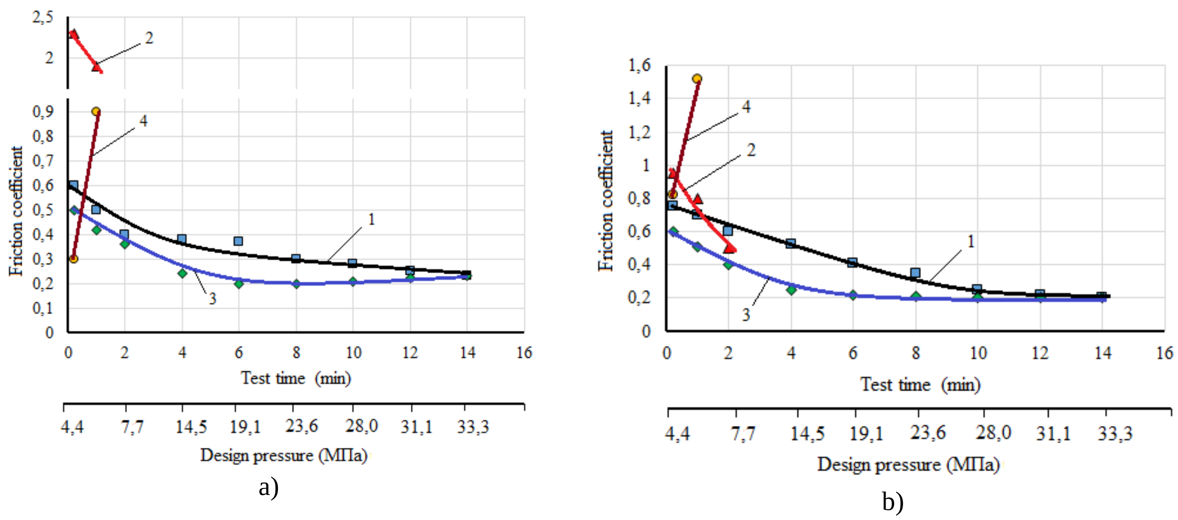

1 – tests with abundant lubrication, n=300 min^{-1}; 2 – tests on formed lubricating formations without additional oil supply, n=300 min^{-1}; 3 - tests with abundant lubrication, n=1000 min^{-1}; 4 - tests on formed lubricating formations without additional oil supply, n=1000 min^{-1}

Fig. 5. - The influence of load and rotation speed on the coefficient of friction of a model tribocoupling when testing Castrol ATF Dexron II Multi Vehicle 75W-80 oil:
a – tribological contact without DC; b - tribological contact with PolytronMTC DC

When tested under conditions of abundant lubrication without the addition of DC, a constant mode of boundary friction was observed briefly for 2 minutes (line 3, Figure 5a) at a rotation speed of n=1000 min^{-1}, the friction coefficient was $\mu \approx 0.2$. At a rotation speed of n=300 min^{-1}, the running-in of the surfaces did not end until the end of the experiments (line 1, Figure 4 a). It is obvious in this case that the speed of contact interaction hindered the speed of reliable structuring of thin lubricant formations. At the same time, the high rate of entry of oil components into the friction zone provided lower values of the friction coefficient, which at a rotation speed of n=1000 min^{-1} was 1.5 times less than at a frequency of n=300 min^{-1}. The addition of a DC with the same features of contact interaction as without a DC led to the achievement of steady-state friction only at the 10th minute of the experiments at a rotation speed of n=300 min^{-1} and at the 6th minute at n=300 min^{-1} (lines 1 and 3 of the figure 5 b). That is, the manifestation of the time factor of the manifestation of the properties and action of the DC to form the corresponding lubricating formations is obvious. But again, it is noted that the steady state of boundary friction occurred with an increase in contact pressure with a friction coefficient of μ = 0.2.

When tested without additional oil supply without adding DC, the formed lubricating formations of the lubricant layers were not able to reduce friction, as evidenced by sharp jumps in the resistance to movement behind the recorder of the friction machine and the experiments stopped. The addition of DC caused a decrease in the initial friction coefficient by 2.5 times at a rotation speed of n=300 min^{-1}, but its large value μ=0.8-1.0 caused significant wear of the ball samples and destruction of the disk surface (Figure 1 d), and the experiments stopped. The created lubricating formations with the addition of DC did not work even at a rotation speed of n=1000 min^{-1}. At the same time, the coefficient of friction at the beginning of the tests was higher for 2.6 cuts compared to layers that were formed without adding DC, and its growth rates were almost the same. According to the temperature indicators given in Table 6, there was an increase in the temperature growth rate by 1.3 times at a disk rotation speed of n=300 min^{-1} with the addition of DC. And at a frequency of n=1000 min^{-1}, on the contrary, there was a decrease in the rate of temperature increase by 1.4 times, which correlated with a decrease in the friction coefficient. High maximum temperatures at a frequency of n=1000 min^{-1} also confirmed the destructive processes of friction surfaces and the inability of the remote control to influence this at high sliding speeds.

Table 6. Temperature indicators when testing Castrol ATF Dexron II Multi Vehicle 75W-80 oil

Rotation speed n, min^{-1}	Without DC			With DC		
	υ_T, ^{0}C.хв$^{-1}$	T_{max}, ^{0}C	ΔT, ^{0}C	υ_T, ^{0}C.хв$^{-1}$	T_{max}, ^{0}C	ΔT, ^{0}C
300	1,3	52	8	1,7	55	16
1000	5,5	120	32	3,8	90	20

According to the wear rate of the ball sample, the value of which is given in Table 7, the addition of DC causes a decrease in the wear rate at rotation speed n=300 min^{-1} by 2.6 times. This is explained by the intensification of the formation of lubricating formations with a shorter time to reach a stable friction mode, and, accordingly, their ability to resist destruction of the metal surfaces of the samples. At a frequency of n = 1000 min^{-1}, there is also a decrease in wear intensity, which is 6.5 times. However, such a decrease does not lead to normal mechanochemical wear, but causes pathological destruction of surfaces, Figure 2 d.

Table 7. Wear rate Is of the ball sample, 10^{-10} m

Rotation speed n, min^{-1}	without DC	with DC
300	4,2	1,61
1000	49,1	7,5

A generalization of the identified trends in the influence of the viscosity class of transmission oil (in accordance with Table 1, kinematic viscosity at 40 0C is taken as an argument), its basis, the addition of DC, the speed mode of contact interaction and lubrication conditions on the wear rate of the ball sample in the form of graphical patterns is shown in Figure 6.

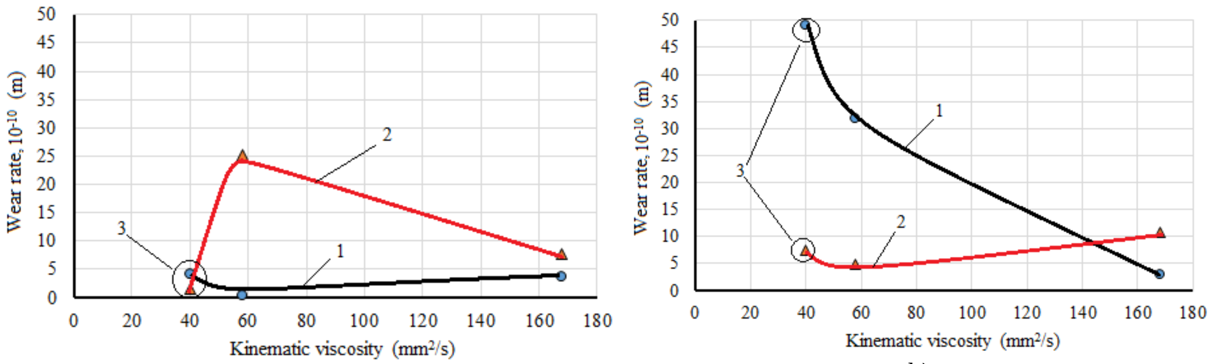

a) b)

1 – without DC; 2 – with DC; 3 – viscosity of mineral-based oil

Fig. 6. - The influence of the kinematic viscosity of the transmission oil on the change in the wear rate of the ball sample according to the test conditions and modes:
(a) – at disk rotation frequency n=300 min^{-1}; (b) - at disk rotation frequency n=1000 min^{-1}

The constructed graphical dependencies indicate the following. There is a fundamental difference in the manifestation of DC when it is added to oils on mineral and synthetic bases. Firstly, for mineral oil, regardless of the sliding speed, the formation of lubricating formations takes place, causing the intended reduction in wear rate at a rotation speed of n = 300 min^{-1} (item 3, Fig. 6a), and its significant reduction at a rotation speed of n = 1000 min^{-1} (item 3, fig. 6b).

Secondly, for synthetic oils at low sliding speeds and a range of kinematic viscosity, for example from 58 mm^2/s to 168 mm^2/s (Table 1), the addition of DC has a negative effect on wear. At the same time, it is possible to achieve equality of wear intensity with a further increase in viscosity, i.e. more than 168 mm^2/s. And since the graphical dependence is tied to a temperature of 40 ^{0}C, it is predicted that the viscosity can be increased by regulating the volumetric temperature of the tribological contact. The opposite picture develops at high sliding speeds. At a rotation speed of $n=1000$ min^{-1} (item 3, Fig. 6b), the addition of DC generally has a positive effect on the formation of wear-resistant lubricating formations from oil components on both mineral and synthetic bases, but in a reduced range of kinematic viscosity, that is from 40 mm^2/s to 58 mm^2/s. Starting from a viscosity of $\nu \approx 58$ mm^2/s, the strength and composition of lubricating formations change, and DC begins to have a weak negative effect on wear when added to synthetic oils. In the range of kinematic viscosity from 140 mm^2/s to 150 mm^2/s, the wear rate of the ball sample is conditionally equal both with and without the addition of DC. Those. wear occurs through the same mechanisms, which are based on the resistance to destruction of cohesive bonds of oil molecules with the active metal centers of the sample materials under the influence of tangential shear deformations. At the same time, a further increase in viscosity of more than 150 mm^2/s causes a change in the strength of the designated adhesive bonds: with DC they decrease due to the energetic imbalance of molecular-mechanical submicrosystems of lubricating formations due to the presence of unrelated hydrocarbons; without DC they increase due to the physical density of the base hydrocarbon compounds.

Conclusions

The results obtained in the work revealed the features of the manifestation of friction and wear of the material system "40X – (transmission olive + POLYTRON^{MTS}) - HCh15" when modeling the destruction of boundary oil formations in the range of contact loads from 4 MPa to 40 MPa at rotation speeds of 300 min-1 and 1000 min-1 1, which reproduces the operating conditions of gears when lubrication conditions are violated.

It has been established that, based on the totality of the obtained tribotechnical characteristics, improvement of the lubrication effect of the considered transmission oils under the influence of POLYTRON^{MTS} is possible under certain restrictions determined by the speed, load conditions and base oil base.

New information about the obtained patterns of changes in the coefficient of friction, wear intensity, and the temperature state of the studied tribological contact expands information about the possible consequences of using POLYTRONMTS. At the same time, it seems possible to compare the results of tribological tests with real load operating conditions of parts, for example gears, and consider questions about the recommended use of POLYTRON^{MTS}.

The authors express their gratitude to the director of Altair-Polys LLC for providing the POLYTRON^{MTC} product for tribological testing.

References

[1] Bukvic M., Gajevic S., Skulić A., Savic S, Ašonja A. Stojanovic B. Tribological Application of Nanocomposite Additives in Industrial Oils // Lubricants, 2024, Vol. 12(1). – P. 3-9.

[2] Wu B., Shi L., Li J., Ding H., Galas R., Omasta M., Guo J. Tribological and rhealogical performance of friction modifiers with different viscosities // Wear, 2024, Vol. 538-539. – P. 15-23.

[3] Dembelova T., Badmaev B., Makarova D., Mashanov A., Mishigdorzhiyn U. Rheological and Tribological Study of Polyethylsiloxane with SiO_2 // Nanoparcles Additive Lubricants, 2023, Vol. 11(1). – P. 9-16.

[4] Guo W., Bai Q., Deng K., Dou Y., Wang T., Wang H. Comparison of ubricationmechanism and friction behavior of graphene on stainless steel substrate at different scales // Appl. Surf. Science, 2023, V. 649. – P. 15-24.

[5] Srinivas V., Rao C.K.R., Abyudaya M., Jyothi E.S. Extreme Pressure Properties of 600 N Base Oil Dispersed With Molybdenum Disulphide // Nano Particles. Univers. 2014, V. 2. – P. 220-225.

[6] Vazirisereshk M.R., Martini A., Strubbe D.A., Baykara M.Z. Solid lubrication with MoS_2 // A. Review. Lubricants, 2019, Vol.7. – P. 57-66.

[7] Polytron Ukraine. Lubricants. https: // latifundist. com/kompanii / 936-politron-ukraina

[8] Today's Most Technologically Advanced Lubricants. http://www.polytron-lubes.com

[9] GOST 9490-75. Liquid and plastic lubricants. Method for determining tribological characteristics on a four-ball machine

[10] Lembyk O. With Polytron, the tractor can work for 40,000 engine hours without overhaul // https://traktorist.ua/articles/854-z-polytron-traktor-moje-pratsyuvati-40-000-motogodin-bez-kapremontu--oleg-lembik

[11] Nehme G., Mourhatch R, Aswath P. Effect of contact load and lubricant volume on the properties of tribofilms formed under boundary lubrication in a fully formulated oil under extreme load conditions // Wear, 2010. Vol. 268(9). – P. 1129-1147.

[12] Kubich V.I., Zadorozhnaya E.A., Cherneta O.G. Forming Laminar Flow of Engine Oil Under Conditions of High-Speed Sliding Friction. Lecture Notes in Mechanical Engineering, // Proceedings of the 5th International Conference on Industrial Engineering (ICIE 2019). - P. 1137-1153.

[13] Kubich V.I., Cherneta O.G., Yurov V.M. Influence of compositions ABRO GT-409 and POLYTRON^{MTC}in transmission oil on tribological contact in material systems CuCrNiZrTi - KCh50, CuCrNiZrTi - 40X // Journal of Physics: Conference Series, 2022, 2182(1), 012077.

Information of the authors

Kubich Vadim Ivanovich, c.t.s., associate professor, National University Zaporozhye Polytechnic
e-mail: schmirung@gmail.com

Cherneta Oleg Georgievich, c.t.s., associate professor, Dnieper State Technical University
e-mail: ocherneta@gmail.com

Yurov Viktor Mikhailovich, c.t.s., associate professor, Karaganda Buketov University e-mail: exciton@list.ru

Portnov Vassiliy Sergeevich, d.t.s, professor, Abylkas Saginov Karaganda Technical University
e-mail: vs_portnov@mail.ru

Amangeldikyzy Altynay, PhD, acting associate professor, Abylkas Saginov Karaganda Technical University
e-mail: amangeldykyzy@inbox.ru

Kopobayeva Aiman Nygmetovna, acting associate professor, Abylkas Saginov Karaganda Technical University
e-mail: kopobayeva@inbox.ru

Madisheva Rima Kopbosynkyzy, acting associate professor, Abylkas Saginov Karaganda Technical University
e-mail: rimma_kz@mail.ru

Askarova Nazym Srajadinkyzy, PhD, lecturer, Abylkas Saginov Karaganda Technical University
e-mail: nazym.askarova@kstu.kz

DOI 10.52209/2706-977X_2024_2_18 **IRSTI 55.20.23** **UDC 62-242**

Method of Cleaning Internal Combustion Engine Radiator Tubes with Ultrasound

Sakhapov R. L.*
Kazan (Volga region) Federal University, Kazan, Russia
*corresponding author

Annotation. The article provides an experimental justification for cleaning radiator tubes. The method consists in the destruction of slag on the inner walls of the radiator tubes due to the cavitation of water under the action of ultrasonic waves. The description of the stand, the experimental technique and its results are given. In particular, the dependences of the slag mass on the time of exposure to ultrasound on the tubes, the temperature of the water and its air saturation are given. The obtained dependencies are reflected in the regression equation. The analysis of the regression equation allowed us to determine the optimal time of exposure to ultrasound. The coefficients of the ratio of the increase in the rate of fluid outflow from the radiator tubes, the mass of the slag and the density of the liquid before and after exposure to ultrasound are proposed. The design and equipment for the radiator cleaning station in the conditions of production and their manufacture at machine-building plants are given.

Keywords: radiator, cavitation, ultrasound, mechanical engineering, dispersion, ultrasonic generator, emitter.

Introduction

Vehicles equipped with an internal combustion engine have, with a few exceptions, a liquid engine cooling system. The heat exchanger in this system is the radiator tubes through which the coolant is pumped [1]. Over time, as the radiator is used, it gets dirty from the outside, and slag settles on the walls in its tubes. All this leads to a decrease in the heat exchange of the radiator with air, overheating of the engine, deterioration of the heating system and incomplete combustion of fuel in the engine [2,3]. This, in turn, worsens the environment and causes various diseases. Increased levels of air pollution caused by emissions from cars and other sources can worsen air quality and weaken human respiratory functions. This can increase the risk of COVID-19 infection and worsen the severity of the disease in those who have already been infected. [4,5,6]. To reduce the impact on the environment and improve public health, various measures can be taken, such as improving the efficiency of vehicles by improving the methods of car maintenance and installing additional exhaust gas purification devices for internal combustion engines [7,8].

Currently, radiator tubes are cleaned mechanically and chemically. The mechanical method is to guide the probe into the radiator tubes. This can damage it due to scratches and chips [9]. The chemical method consists in washing copper radiators with alkali, and aluminum radiators with acid. At the same time, parts made of other materials corrode, streaks and microcracks occur [10].

Modern mechanical engineering produces a number of devices for the diagnosis of diseases, geographical research, purification of gases and liquids and laundry. Ultrasonic and electric pulse methods of exhaust gas purification are developing prospectively. This method involves the use of ultrasonic waves to destroy pollution particles in exhaust gases. Both of these methods are aimed at reducing the level of harmful emissions from automobile exhaust, which contributes to improving air quality and reducing the negative impact on the environment and human health. [11,12].

In connection with the above, we have proposed a method for cleaning the walls of the radiator from scale by ultrasonic action on the water poured into the tubes.

This method has no disadvantages of chemical and mechanical methods and is therefore relevant.

We have proposed a method for cleaning radiators by cavitating water in tubes under the action of ultrasound.

The purpose of the experiment was to confirm the hypothesis of the effectiveness of the proposed method.

The practical usefulness of the proposed method is to simplify the washing procedure and make it safer for the structure.

The scientific novelty is in obtaining dependences of the efficiency of radiator cleaning on the mass of washed scale, pulp density and the rate of liquid outflow from the tubes.

During the experimental study, the following tasks were solved: equipment and measuring equipment were selected, a plan and procedure for conducting the experiment were developed, controlled factors and parameters were determined, quantitative and qualitative indicators determining the process under study were proposed, experimental data were obtained and experimental results were processed.

1. Methods and materials

The process of cleaning radiator tubes is carried out by cavitation of water under the influence of ultrasound.

Cavitation is a process of rapid destruction of air bubbles in a liquid having a strong destructive effect on the contact surface [13].

The authors conducted a preliminary experiment on cleaning the radiator tubes of a car. The experiment showed the effectiveness of the cleaning method [14]. However, due to the small size of the radiator, there was doubt about the effectiveness of the process on large radiators. This doubt was due to the fact that the scale coefficients in this case are not linear and it is impossible to determine a multiple of the size to change the result.

Also, a preliminary experiment, during which two main effects were considered: along and across the radiator tubes, showed that the longitudinal effect has a more effective result in the process of cleaning the radiator with ultrasound. This is due to the fact that with a transverse wave, it is necessary to cross the interface of the media several times, in this case, twice the walls of each tube. This leads to a rapid attenuation of the transverse wave [14 p. B290].

To implement a preliminary experiment on ultrasonic cleaning of the radiator, a liquid with the lowest viscosity was selected, while the liquid was saturated with air. This is justified by theoretical assumptions, according to which the use of a low-viscosity liquid contributes to a more efficient generation of cavitation bubbles under the influence of ultrasonic waves [14 p. B293, 15,16]. Air saturation additionally enhanced the cavitation processes, contributing to a more efficient removal of impurities from the internal cavities of the radiator tubes [17, 18].

An experimental study on cleaning the radiator of the cooling system was carried out on the radiator from the UAZ PATRIOT car using an assembled ultrasonic installation for cleaning car radiators based on preliminary results.

The installation for cleaning radiators by ultrasound consists of the following elements, shown in Figure 1.

Fig.1. – Installation for cleaning radiators with ultrasound

To clean the radiator with an ultrasonic wave, three ultrasonic generators and emitters with a frequency of 40 kilohertz and a power of 120 watts were used.

Longitudinal ultrasonic action was performed on the radiator by three emitters simultaneously shown in Figure 2.

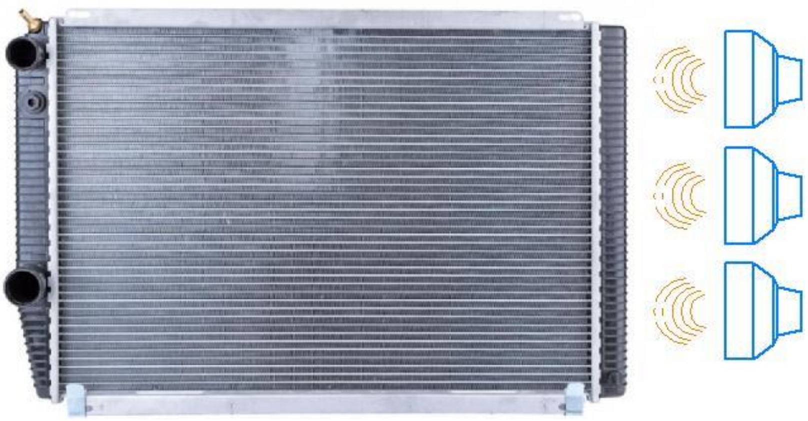

Fig. 2. – The effect of ultrasound on the radiator

During the experiment, liquid parameters such as density, volume and mass were determined. The following equipment was used to determine the parameters: electronic jewelry scales MN-500, measuring cylinder 50ml., measuring jug 1000 ml.

3. Experiment

In the experiment, distilled water with the lowest dynamic viscosity was used as a washing liquid. The water was saturated with air using an air pump and heated to a temperature of 55 degrees Celsius. The selected liquid parameters provide optimal conditions, fast and effective manifestations of cavitation processes and scale dispersion in the radiator [18, 19].

The experimental study was conducted in accordance with the following procedure: pure distilled water was poured into the radiator, the mass, volume, density and rate of water flow through the radiator were determined. Then the water was poured back, the water was saturated with air through the pump, ultrasound was applied for various times and the rate of water flow through the radiator, mass, volume and density were re-determined. The determination of liquid parameters before and after exposure to an ultrasonic wave was carried out by weighing, which made it possible to obtain accurate quantitative data on the mass and density of the liquid. The scale mass was determined by subtracting the mass of pure water from the total mass of the obtained pulp, which allowed to obtain the mass of washed scale. The pulp is a liquid with scale obtained as a result of exposure to ultrasound on the radiator [20]. Scale is solid deposits formed on the surfaces of heat exchange elements, where the liquid is heated or cooled [21]. The efficiency of the purification process was determined by the difference obtained. Figure 3 shows the detached scale from the internal cavities of the radiator.

Fig. 3. – Washed scale after exposure to ultrasound

Scale formation is not only associated with the decomposition of the coolant, but also occurs due to the effects of additional substances such as engine oil, gasoline, solid oil and others [21,22,23]. These components can contribute to the formation of solid deposits and affect the efficiency of heat transfer in the radiator.

3. Results and discussion

The conducted experiment was analyzed, as a result of which patterns were revealed and dependencies between the measured parameters were obtained. Graphs were plotted based on these dependencies, which made it possible to visualize the results and better understand the effect of ultrasonic exposure on the liquid poured into the radiator.

The measured parameters were systematized and presented in table 1, which makes it possible to evaluate changes in various parameters during the exposure to ultrasonic cleaning and to conduct a detailed analysis of the experimental results.

Table 1. Measured parameters when exposed to ultrasound

№	Ultrasound exposure time in seconds	The mass of the liquid in grams	Volume of water in milliliters	The density of the liquid in g/cm^3	Liquid expiration time in seconds	The temperature of the liquid in C^o	Fluid flow rate in ml/s
1	0	49,53	50	0,9906	3,34	55	299,40
2	600	51,39	50	1,0278	3,243	55	308,36
3	1200	53,74	50	1,0748	3,127	55	319,80
4	1800	57,18	50	1,1436	2,98	55	335,57

The analysis of experimental data made it possible to establish a relationship between the density and the rate of fluid flow through the radiator, depending on the time of exposure to ultrasound, which is reflected in Figures 4 and 5. These dependencies allow us to estimate the degree of intensity of cleaning the radiator tubes.

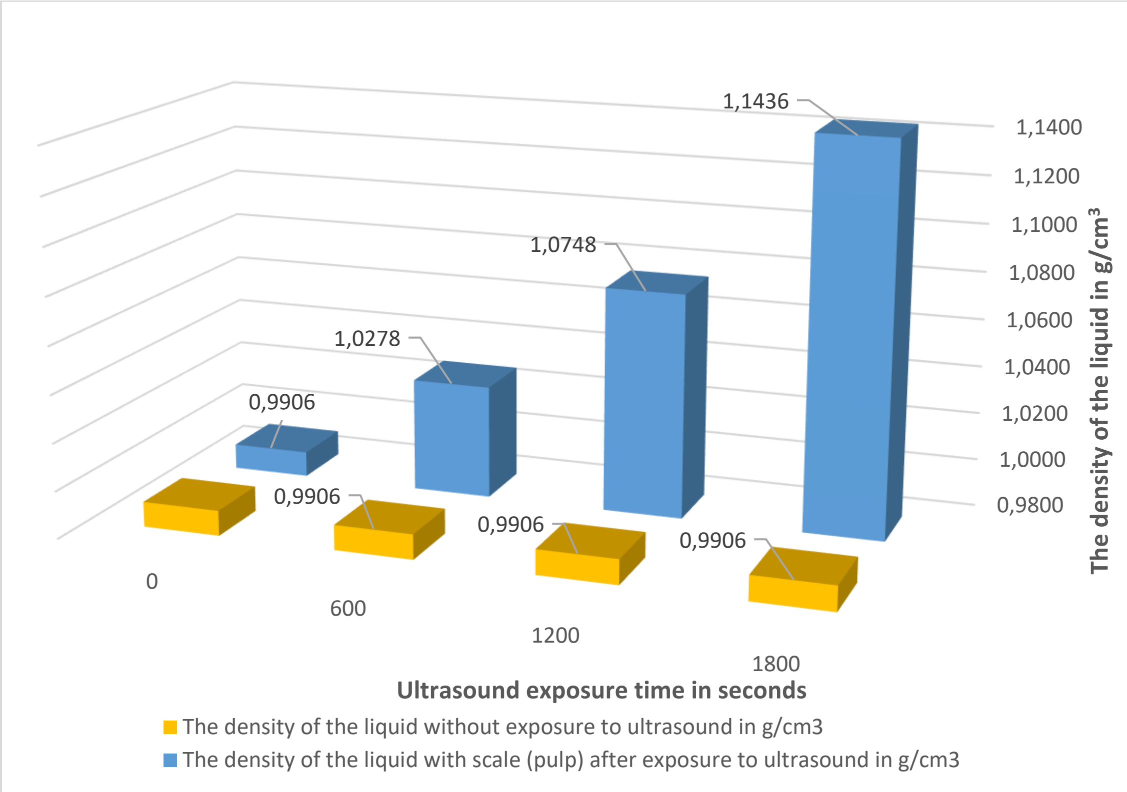

Fig. 4. – Changes in the density of the liquid depending on the time of exposure to ultrasound

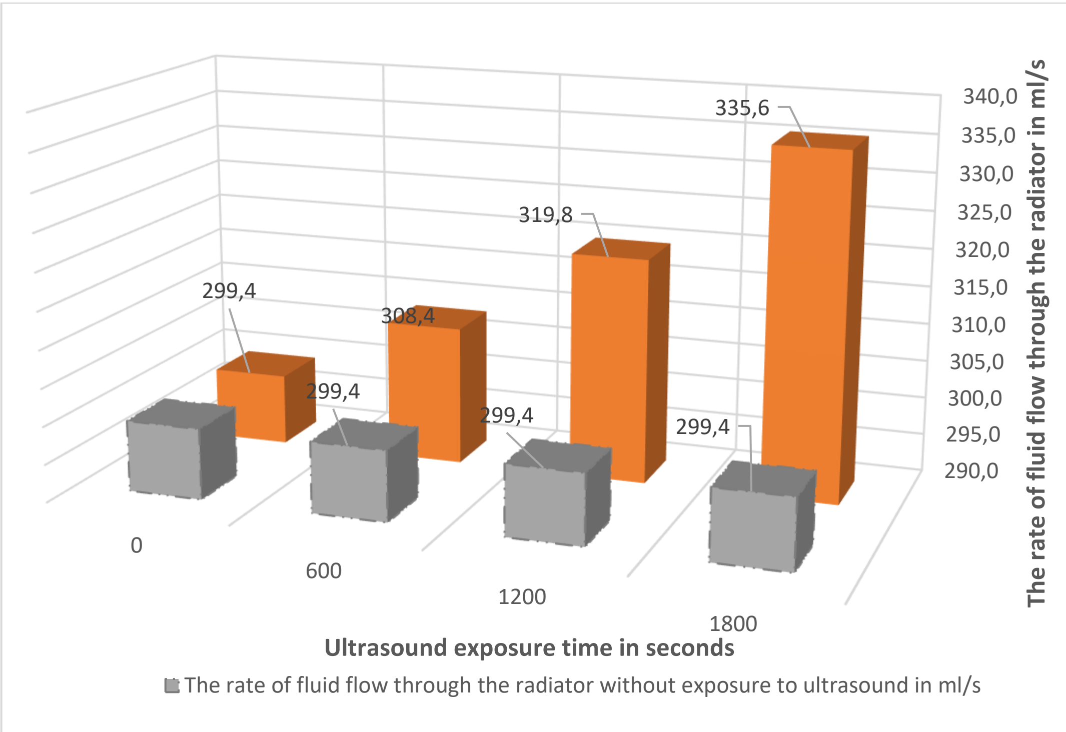

Fig. 5. – Changes in the rate of fluid flow through the radiator of the car depending on the time of exposure to ultrasound

The obtained graphs are a tool for visual examination, deeper data analysis and drawing conclusions about the effectiveness of ultrasonic exposure in the radiator cleaning process. Graph analysis makes it possible to assess the dynamics of the effect of ultrasound on the flow processes and properties of the liquid in the radiator, providing information on the effectiveness of ultrasonic cleaning depending on the exposure time.

With an increase in the time of exposure to ultrasound, an increase in the rate of discharge of liquid with scale is observed. This means that the effect of ultrasound has a more pronounced effect on the expiration of the pulp compared to pure water with an increase in processing time.

Table 2 shows the dynamic changes in pulp mass depending on the time of exposure to ultrasonic treatment and plots shown in Figures 6 and 7. These data reflect the weight of the pulp and the scale content, as the time of exposure to ultrasound. By subtracting the mass of pure water from the total mass of the pulp, the mass of washed scale was obtained. This approach allows us to quantify the effectiveness of the ultrasonic cleaning process and highlight the effect of this effect on descaling from the internal cavities of the radiator.

Table 2. Measured liquid parameters

The time of exposure of the ultrasonic wave to the radiator	seconds	0	600	1200	1800
The mass of the liquid	grams	49,53	51,39	53,74	57,18
Scale mass after exposure to ultrasound	grams	0	1,86	4,21	7,65

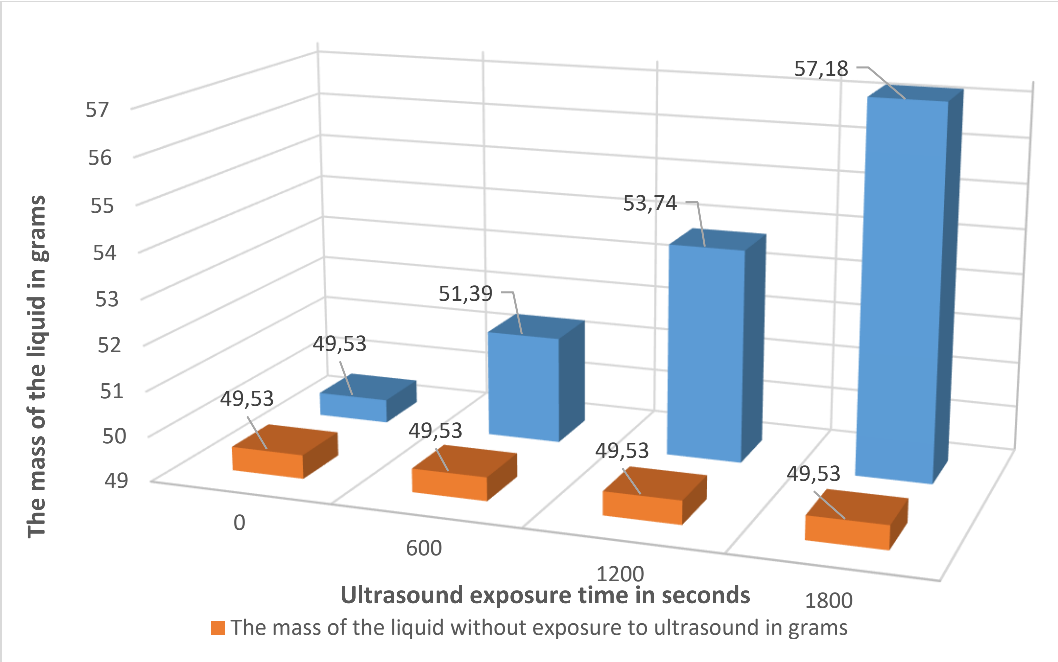

Fig. 6. – The obtained pulp mass depending on the time of exposure to ultrasound

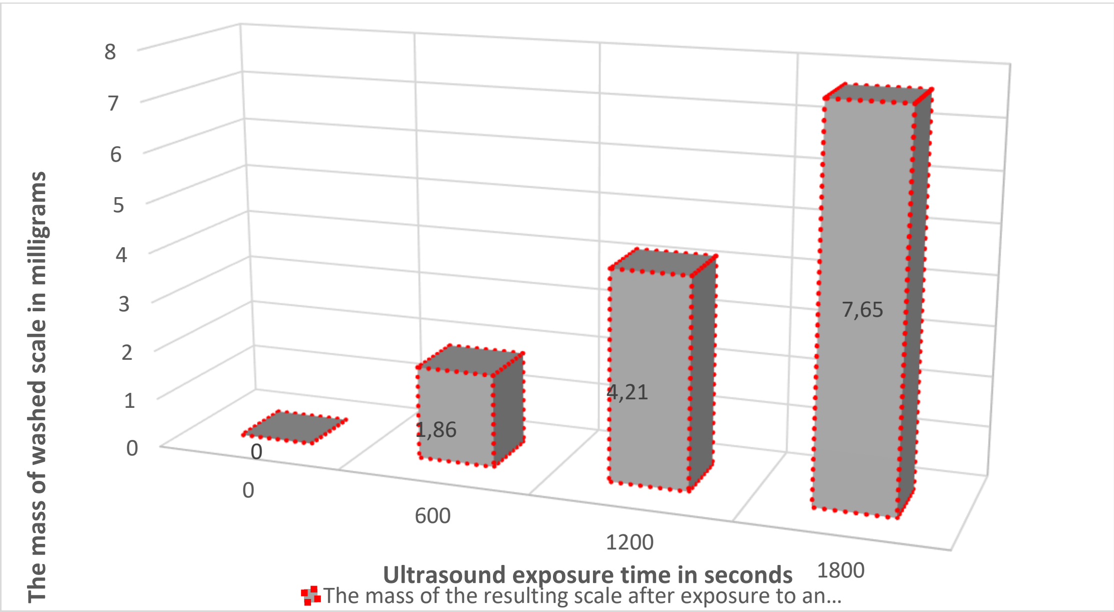

Fig. 7. – The resulting scale mass depending on the time of exposure to ultrasound

The analysis of these changes makes it possible to assess the dynamics of descaling from the radiator. With an increase in the time of exposure to ultrasound on the car radiator, the scale content in the liquid increases. The obtained dependences emphasize the effect of ultrasonic cleaning on the effective removal of scale from the radiator, which supports the initial assumption about the effectiveness of this method in the field of maintenance of the cooling system of transport equipment.

The resulting fluid mass data were interpolated by the Newton polynomial to more accurately determine the regression. From the analysis of the calculations performed for the highest values of the correlation coefficients, determination and the lowest values of the average approximation error, the quadratic regression equation was used for the radiator cleaning process by ultrasound:

$$y=ax^2- bx+c \tag{1}$$

$$y = 0{,}0000010973x^2 - 0{,}0021370795x + 49{,}6540167414$$

Correlation coefficient = 0,9996895857;
Coefficient of determination = 0,9993792678;
Average approximation error = 0,0901504992%.

The purification efficiency coefficients were calculated using the ratios of scale mass, density and fluid flow rate at different exposure times to ultrasound. These coefficients are presented in Table 3 and shown in Figure 8. The obtained coefficient values reflect the degree of effectiveness of ultrasonic cleaning depending on the exposure time, providing a quantitative assessment of the experimental results [14 p. B297].

Table 3. Coefficients justifying the efficiency of radiator cleaning

The effects of the ultrasonic wave on the radiator in seconds	The coefficient of increase in the rate of fluid flow after exposure to ultrasound	The coefficient of increase in the mass of washed scale after exposure to ultrasound	The coefficient of increase in liquid density after exposure to ultrasound
0	1	1	1
600	1,029927	1,037553	1,037553
1200	1,068136	1,084999	1,084999
1800	1,120808	1,154452	1,154452

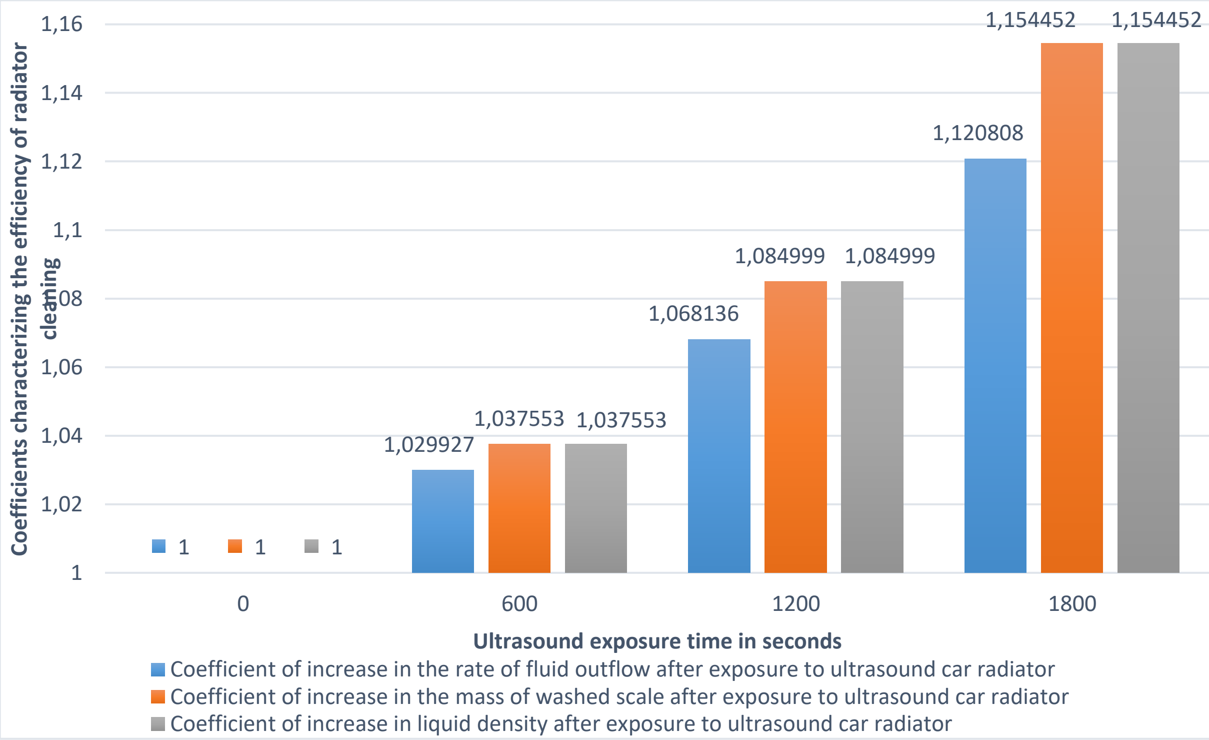

Fig. 8. – Coefficients justifying the efficiency of radiator cleaning

The obtained coefficients shown in Figure 8 reflect the processes that occur during cavitation into a liquid under the influence of ultrasound, and justify the effectiveness of scale destruction in radiator tubes. These coefficients represent a quantitative assessment of the degree of scale destruction and serve as important indicators of the effect of ultrasonic cleaning on the radiator, where higher values indicate a more efficient cleaning process.

Conclusions

The experiment confirms the hypothesis of the effectiveness of the proposed method for cleaning radiators of the cooling system of transport equipment equipped with internal combustion engines.

During the experimental study, the possibility of manufacturing new equipment for safe and innovative descaling of radiators using ultrasonic exposure, during maintenance of the cooling system of transport equipment, was proved.

The results obtained are a key component in understanding the cleaning process and can serve as a basis for further optimization of ultrasonic radiator cleaning conditions.

The results have both scientific and practical significance in the field of developing a methodology for calculating the parameters of the technological process and equipment for radiator maintenance. These findings are important for clarifying and optimizing the maintenance procedures for cooling systems, in particular radiators, which contributes to improving the efficiency and durability of automotive systems.

References

[1] Savich E.L. The device of cars. Engines: educational settlement – Minsk: Higher School, 2019. – 334 p.
[2] Kravchenko V.A., Butkov R.I. Maintenance and repair of motor vehicles. – Zernograd, 2015. – 339 p.
[3] Sherov K.T., Absadykov B.N., Sikhimbayev M.R., Togizbayeva B.B., Esirkepov A. Investigation of the stress-strain state of components of a hydraulic impact device. News of the National Academy of Sciences of the Republic of Kazakhstan. Series of geology and technical sciences, 2023. Volume 1, Number 457. - P.260-269.
[4] Kadyrova I., Kolesnichenko S., Kolesnikova Ye., Korshukov I., Barkhanskaya V., Sultanbekova A., Babenko D. SARS-COV-2 detection in MALDI-TOF mass spectra by machine learning // AIP Conference Proceedings, 2023, Vol. 2872, №1.
[5] Yessenbayeva A., Apsalikov B., Massabayeva M., Kazymov M., Shakhanova A., Mussazhanova Z., Kadyrova I., Aukenov N., Shaimardanov N. Biomarkers of immunothrombosis and polymorphisms of IL2, IL6, and IL10 genes as predictors of the severity of COVID-19 in a Kazakh population // PLoS One., 2023, Vol.18, №6.
[6] Kolesnikova Y., Babenko D., Kadyrova I., Kolesnichenko S., Akhmaltdinova L., Korshukov I., Kabildina N., Sirota V., Zhumaliyeva V., Taizhanova D., Vazenmiller D., Turmukhambetova A. Association of four genetic variants with colorectal cancer in Kazakhstan population // Oncotarget, 2021, Vol.12, №21, P. 2215-2222.
[7] Kadyrov A., Sarsembekov B., Ganyukov A., Suyunbaev S., Sinelnikov K. Ultrasonic Unit for Reducing the Toxicity of Diesel Vehicle Exhaust Gases // Communications - Scientific Letters of the University of Zilina, 2022, Vol. 24, №3. – P. B189-B198.
[8] Kadyrov A., Kryuchkov Y., Sinelnikov K., Ganyukov A., Sakhapov R., Kukesheva A. Studying the Process of the Internal Combustion Engine Exhaust Gas Purification by an Electric Pulse // Communications - Scientific Letters of the University of Zilina. – 2022. – Vol. 24, №4. – P. B275-B287. -https://doi.org/10.26552/com.C.2022.4.B275-B287
[9] TM 10-450 Sheet Metal Work, Body, Fender And Radiator Repairs / War Department. – Washington, 1941. – 119 p.
[10] Ilyin M.S. Bodywork. Straightening, welding, painting, anti–corrosion treatment. - M., 2009. – 480 p.
[11] Kadyrov A., Bembenek M., Sarsembekov B., Kukesheva A., Nurkusheva S. The Influence of the Frequency of Ultrasound on the Exhaust Gas Purification Process in a Diesel Car Muffler // Applied Sciences – 2024. – Vol. 14, №12. – 4, 5027
[12] Kadyrov A., Kryuchkov Y., Kukesheva A., Pak I., Kurmasheva B., Kabikenov S. Development of Calculation Methodology for Optimizing the Operating Mode of an Electric Pulse Unit for Cleaning Exhaust Gases // Communications - Scientific Letters of the University of Zilina. – 2024. – Vol. 26, №1. – P. B41-B53.
[13] Kardashev G.A. Physical methods of intensification of chemical technology processes. – M.: Chemistry, 1990. – 205 p.
[14] Kadyrov A., Sinelnikov K., Sakhapov R., Ganyukov A., Kurmasheva B., Suyunbaev S. Studying the Process of Transport Equipment Cooling System Ultrasonic Cleaning // Communications - Scientific Letters of the University of Zilina. – 2022. – Vol. 24, №4. – P. B288-B300.
[15] Magomedov U.B., Magomedov M.M.-Sh., Alkhasov A.B. Handbook of thermal conductivity and dynamic viscosity of water and aqueous solutions of salts. – M.: Fizmatlit, 2013. – 219 p.
[16] Kyzylbaeva E., Kukesheva A., Kunaev V. Mathematical model of plate movement in thixotropic mud // Material and Mechanical Engineering Technology 2020. – Vol. 2, №2. – P. 26-30.
[17] Kozyrev S.P. Hydroabrasive wear of metals during cavitation. – M.: Mashinostroenie, 1971. – 240 p.
[18] Sinelnikov K.A. Development and research of methods of maintenance and operation of a car using ultrasound: dis. ...doc. PhD: 8D071. – Karaganda, 2023. – 142 p.
[19] Golyamina I. P. Ultrasound: a small Encyclop. Moscow: Sovetskaya encyclopedia publ., 1979, 400 p.
[20] Larichkin V.V., Gusev K.P. Industrial ecology. Laboratory practice. - Novosibirsk: NSTU Publishing House, 2011. - 56 p.
[21] Tokarev, A. O., Mironenko I. G. Failures of machine parts. Analysis of causes, technical diagnostics and prevention. -Moscow; Vologda: Infra-Engineering, 2020. - 220 p.
[22] Kadyrov A., Sarsembekov B., Ganyukov A., Zhunusbekova Z., Alikarimov K. Experimental research of the coagulation process of exhaust gases under the influence of ultrasound. // Communications - Scientific Letters of the University of Zilina, Vol. 23, Issue 4, 2021. – P. 288-298
[23] Rutenburg G.B. Operation and repair of automobile radiators. – M., 1955. – 81 p.

Information of the authors

Sakhapov Rustem Lukmanovich, d.t.s., professor, Kazan (Volga region) Federal University
e-mail: coolzero7777@gmail.com

DOI 10.52209/2706-977X_2024_2_25 IRSTI 55.03.14 UDC 621.91

Improvement of Base Sets for Complex Configuration Parts when Assessing their Manufacturability within Industry 4.0

Berg A.S.[1], Nurzhanova O.A.[1*], Vytautas T. [2], Berg A.A.[1], Vitushenko D.V.[1]
[1]Abylkas Saginov Karaganda Technical University, Karaganda, Kazakhstan
[2]Vilnius Gediminas Technical University, Lithuania, Vilnius
*corresponding author

Annotation. Assessment of the manufacturability of products is carried out at the early stages of production preparation. The quality of this assessment significantly affects the efficiency of subsequent actions, including the development of technological processes and equipment operation. Currently, there is no accurate and complete description of the assessment methodology, which makes it dependent on the subjective experience of the technologist and prevents the creation of a formalized model. The purpose of this paper is to improve the quality of machining of complex configuration parts and the efficiency of manufacturing systems by developing new quantitative indicators of manufacturability. The paper presents a sequence of steps to create and calculate these indicators using the example of the part “Cover 2522-4202051”. This process includes the formation of graphs of interrelationships between the surfaces of the part, taking into account the design bases and requirements to their geometric characteristics. The obtained information is transformed and formalized in the form of a database, which serves as a basis for defining new quantitative indicators of manufacturability. The result is a set of new indicators that allow to evaluate the conformity of the part design to the possibilities of using a single base when designing its manufacturing process. The proposed indicators provide analysis of the use of rational technological bases in the manufacturing process of parts and complement the existing indicators, providing more complete information on the compliance of the part design with technological processing methods and the efficiency of manufacturing systems.

Key words: production automation, basing, basis set, graph, dimensional analysis, Industry 4.0

Introduction

In recent decades, the advent of Industry 4.0 has ushered in a new era in the industrial landscape, marked by a profound focus on novel technologies and automation, instigating significant global transformations. Industry 4.0 embodies the integration of cutting-edge technologies such as the Internet, artificial intelligence, automation, and cloud computing into industrial and economic operations. Given its aspirations for modernization, the Republic of Kazakhstan stands among the nations diligently embracing the principles of Industry 4.0 across various sectors of its economy [1].

The manufacturing industry stands out as a pivotal domain where Kazakhstan endeavors to implement the tenets of Industry 4.0. Advanced automation and robotics technologies hold the promise of substantially enhancing production efficiency, curbing labor expenses, and elevating product quality. Notably, in sectors like automotive manufacturing, automated assembly lines and robotic systems accelerate production timelines while concurrently minimizing the occurrence of errors.

At its core, Industry 4.0 represents a paradigm shift in industrial and economic progress, underscored by the integration of cutting-edge technologies into manufacturing processes. Central to this transformative journey are Computer Numerical Control (CNC) machines. These sophisticated devices, facilitating automation and adaptability in production, play a pivotal role in realizing the vision of Industry 4.0 [2].

The complex of issues related to the assessment of production manufacturability of manufactured parts is at the forefront of the development of machining production machine-building systems. At present, the evaluation of manufacturability of manufactured parts directly depends on the technologist's (designer's) experience and subjective knowledge, which does not guarantee correct decision-making based on the knowledge of data on actively developing capabilities and on the real state of production. The assessment of manufacturability is used to display the relationship between the costs at the time of manufacturing a part and its design features, it has a contradictory nature, and also does not have an accurate and complete description of the procedure of carrying out [3-6, 11].

The main approaches to resolving the currently existing problems are:

- finding the weight values of individual manufacturability indicators depending on the characteristics of real production and the nomenclature of manufactured parts;
- expansion of the nomenclature of quantitative indicators of production manufacturability assessment, which are aimed at taking into account the used approaches to production preparation and the peculiarities of certain production complexes [7-9, 11].

The main purpose of the study is to improve the methodology for assessing production manufacturability on the basis of the formation of additional indicators, which, in turn, are interrelated with the constantly updated requirements for improving product quality, the production process itself, as well as the rational use of available equipment. The works [10 - 11] reflect the indicators that provide an opportunity to orient the evaluation of manufacturability on the design features of multi-nomenclature complexes of mechanical processing and that take into account the requirements of a particular production system, the conditions of formation of links between production manufacturability and its impact on the technological aspects of processing. The composition of additional indicators for assessing manufacturability for their application in the planning system of multinomial technological processes is presented [11].

1. Methodology

In mechanical engineering technology as a science, one of the fundamental rules, which is applied when assigning technological bases for the creation of technological processes, is the principle of unity and constancy of bases. Known indicators of manufacturability assessment do not provide an open and complete possibility for predicting the conformity of the manufactured part design to the potential possibilities of compliance with these principles when designing technological processes of their manufacturing. In order to solve this problem, it is necessary to create absolutely new indicators of quantitative assessment of manufacturing manufacturability, which should allow to form a conclusion about the reality of compliance with the principle of unity and constancy of bases in the process of technological process design and to estimate the value of this compliance [11].

Let us consider the proposed sequence of determination of the developed new indicators of quantitative assessment of production manufacturability on the example of the part "Cover 2522-4202051". The part "Cover 2522-420202051" (Figure 1) is a part of the rear PTO shaft of MTZ - 2522 tractors, belongs to the parts of the type of bodies of rotation and includes external and internal cylindrical surfaces, ends, chamfers, holes, internal grooves.

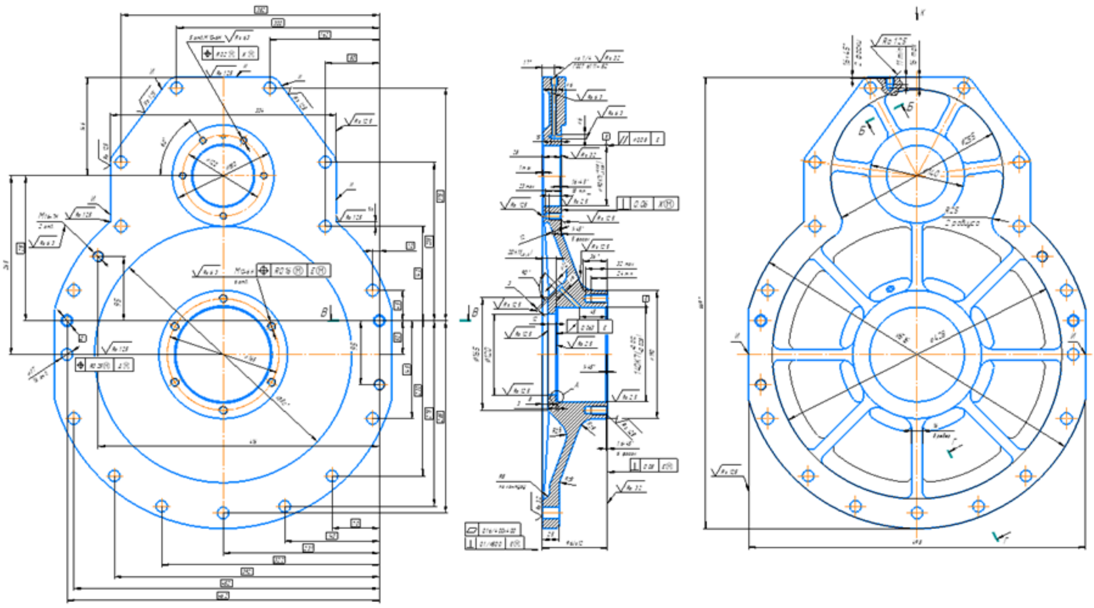

Fig. 1. - Drawing of the part "Cover 2522-4202051"

In order to fully analyze the structural properties of a manufactured part, first of all, it is necessary to determine the number of cross-sections in which dimensional relationships are formed, which open the possibility to reveal comprehensive data on the spatial and dimensional characteristics of various constituent elements of the manufactured part [11].

Modern manufacturing tends to apply advanced digital and intelligent technologies, including robotic systems. An important development trend in this area is the use of network-centric manufacturing networks. These networks allow efficient planning and execution of parallel manufacturing processes. Examples of such modern manufacturing sites include complexes of multifunctional CNC machines, 3D printers, and robots integrated into a network for optimal task execution [12, 13, 14-19].

Manufacturing process preparation (TPP) plays a key role in the part production process. It includes the solution of tasks to ensure manufacturability of the product design, design of technological processes, manufacturing of technological tooling and management of the production preparation process. In single and small batch production, standard automation methods such as element and process typing may be ineffective due to the high costs of preparatory work.

The construction of a simulation model of production processes and multi-criteria analysis on its basis are effective methods of selecting the optimal variant of technological process. The authors will use this model when evaluating the technological preparation of production.

Automation of production processes, including technological preparation, selection of sets of bases increases the efficiency of the enterprise and its competitiveness [12, 20]. Digitalization of processes reduces the time of production preparation and optimizes the total cost of manufacturing products. In addition, such automation allows adapting technological processes to changing conditions and promptly responding to them [12, 21].

When designing technological processes for manufacturing machine parts, dimensional calculations of the main output parameters of the technological process, as well as assessment of the accuracy of the technological process as a whole occupy a significant place in the whole set of works.

The dimensional analysis of technological processes is understood as a set of works on construction of special dimensional schemes, calculations of operational dimensional chains, determination of tolerances and allowances at operations, determination of blank sizes, evaluation of different variants of technological processes, etc.

Dimensional analysis is used for newly designed or existing technological process. In this case, the following tasks are solved:

a) to establish scientifically justified operational dimensions at all operations of the technological process;

b) to establish scientifically justified optimal dimensions of workpieces;

c) to ensure the design of technological processes with a minimum number of operations.

These tasks are solved with the help of dimensional chains. Dimensional chains, the links of which are operational dimensions and allowances, as well as the drawing dimensions of the processed part, are called technological [22].

Dimensional analysis of technological processes of part “Cover 2522-4202051” is presented in Figure 2.

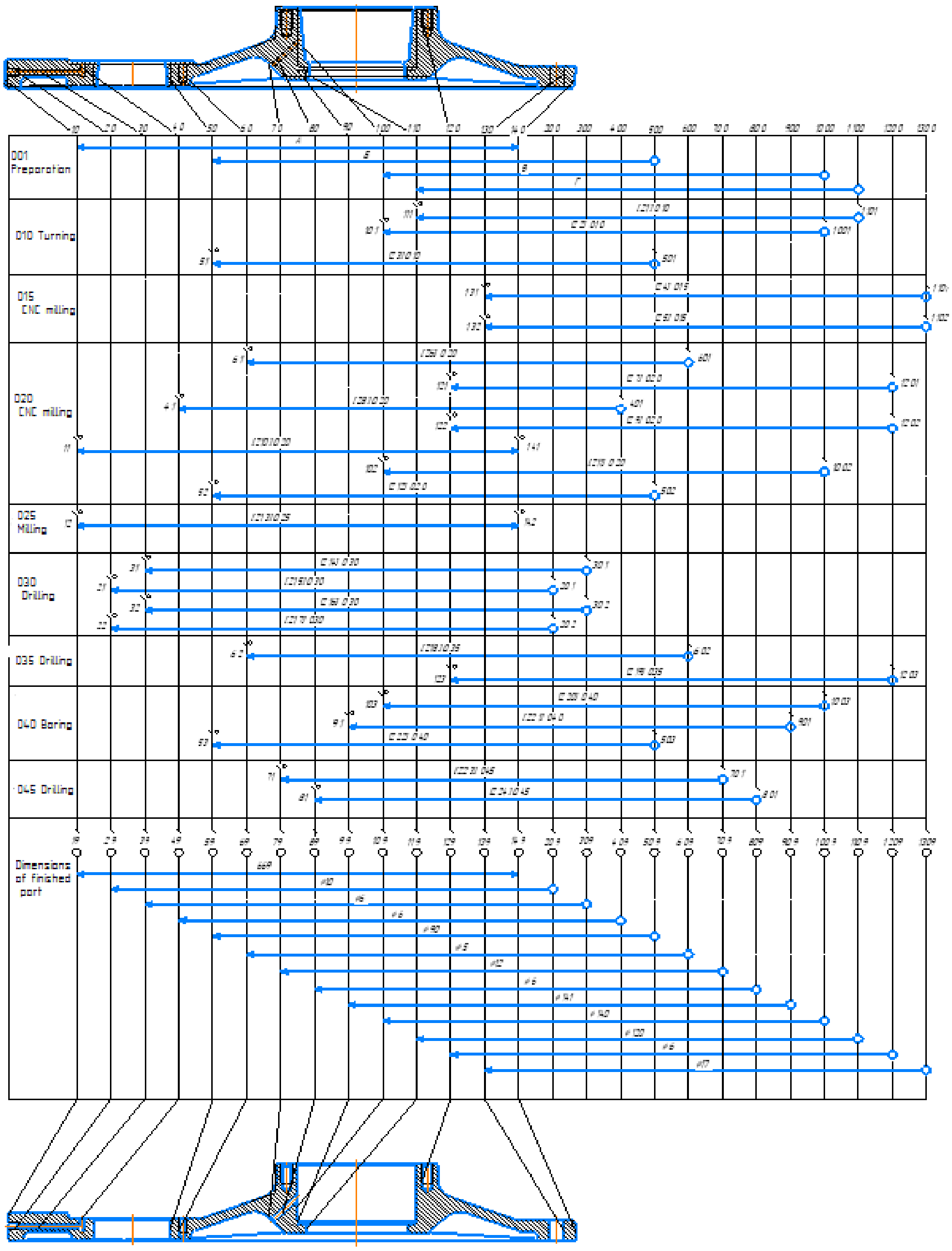

Fig. 2. Dimensional analysis of the technological process

The methodology for analyzing the similarity of design solutions within the framework of technological preparation of production relies on the formalization and comparison of design and technological solutions [12, 23-25]. The main concept in this methodology is a technological complex (hereinafter referred to as T-complex), which is a set of different typical surfaces. For these surfaces there is a common machining trajectory that allows them to be machined together. To each T-complex there correspond certain technological methods, which can be applied individually or in combination, depending on the production conditions and the required manufacturing quality.

T-complexes are characterized by the following features: types of incoming surfaces, production and operational quality indicators, as well as external attributes that determine the relationship of this complex with the others. These relations can be represented in the form of a graph model, where nodes are identifiers of selected T-complexes, and edges are corresponding links between them. The graph of links allows to estimate the constructive similarity in two ways: on the basis of the composition of T-complex models and on the basis of the structure of links between them [12, 26, 27].

From these positions, the part "Cover 2522-4202051" can be investigated using two views, respectively, one dimensional scheme, which is presented in the graph format in Figure 3 [22].

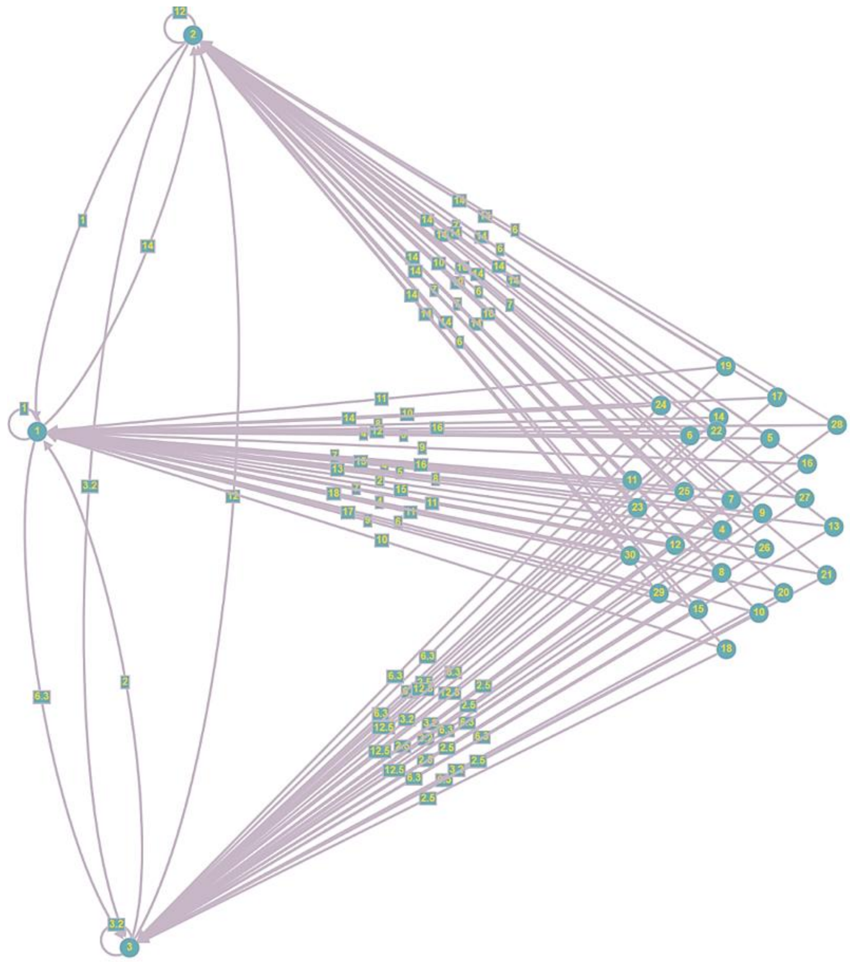

– symbolic designation on the graph, including: surface number on the design drawing, coding of elementary surface, regulated in the planning system of multi-nomenclature technological processes;

– accuracy characteristics of part surfaces

Fig. 3. Design graph for part "Cover 2522-4202051"

In order to assess the manufacturability of the manufactured part from the point of view of building predictive data on the level of meeting the requirement of unity of bases in the process of designing the manufacturing process, a necessary and obligatory condition is the study of information formed as a result of analyzing the operational design bases of parts during its operation directly in the assembly itself.

The part "Cover 2522-4202051" is a part of the rear power take-off shaft of MTZ-2522 tractors. These tractors are designed to perform a full range of agricultural work with mounted, semi-mounted, trailed machines and implements, loading and unloading equipment, with harvesting complexes, to drive various kinds of stationary special machines, as well as for transportation work in different climatic zones. The part is designed for connection with the body on one side and with the spacer on the other side. For the considered part the design bases are: surfaces 5 and 9 (Figure 4). To fix these data, additional designations for the surfaces of the part, which are the design bases and finding of the minimum spanning tree [11], are introduced into the constructed graphs.

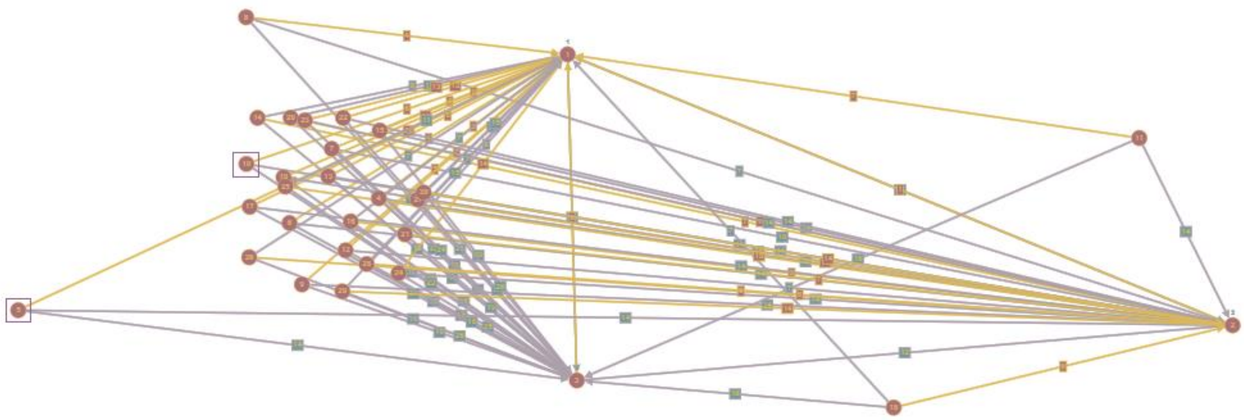

— basic design bases of the part "Cover 2522-4202051"

Fig. 4. A graph augmented with information about design bases and search for a minimal island tree

When selecting technological bases during the creation of technological processes, it is especially important to pay attention not only to dimensional characteristics, but also to the specified parameters that determine the requirements for the geometric shape of surfaces, for this purpose, the graph is saturated with this information. obtained from the design drawing of the part (Figure 5).

It is necessary to emphasize the requirement of the principle of unity and constancy of bases in the process of technological process development. For example, in addition to geometric and dimensional characteristics, it is necessary to take into account the constraints that are noted in the design documentation and set the limits of the mutual location of surfaces relative to each other. It is also important to consider the positional tolerance, which includes the mutual arrangement of the surfaces and the permissible deviation from the geometric shape. Based on the analysis of this information, the graph can be supplemented with the necessary data (Figure 5) [11].

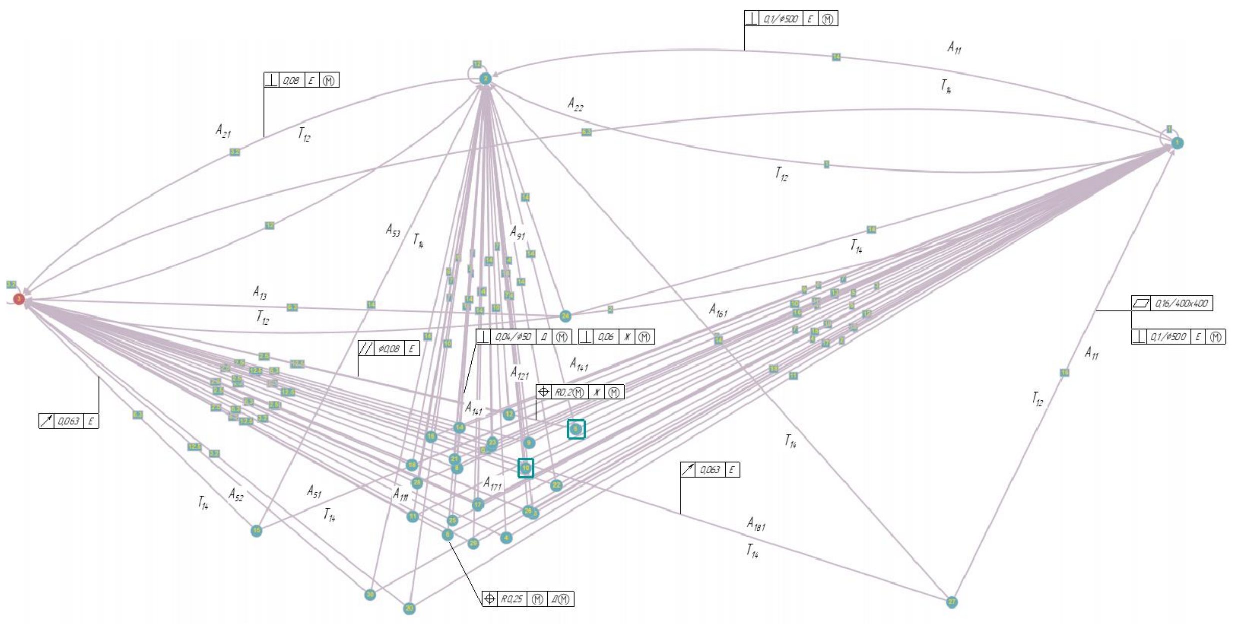

Fig. 5. Graph supplemented with information about the mutual arrangement of surfaces and positional tolerances of the part "Cover 2522-4202051"

The designed graph provides an opportunity for subsequent formalized processing of the generated information about the design characteristics of the manufactured part, without which it is impossible to perform the analysis of requirements satisfaction by the fact of assigning technological rational bases in the future development of the manufacturing process of the part. The obtained data are presented in the format of a relational database, which includes information about the relationships between all the elements of the manufactured part for each size and other norms presented in the design drawing [11].

The presented model of the sequence of data formation serves as a basis for the development of new quantitative indicators of production manufacturability, allowing to establish a relationship between the possibility of creating technological processes that meet the principle of unity and consistency of bases and design features of parts. It is used to propose an index of manufacturing manufacturability of a part, which reflects the possibility of compliance with the principle of unity of bases in the development of technological process in terms of evaluating the relationships between the surfaces of the part and the surface, which is the main design base:

$$K_{EO} = \frac{1}{M}\sum_{i=1}^{M} NO_i, \tag{1}$$

where M - total number of dimensions and requirements in the design drawing that define the relationship between the surfaces;

$NO_i \in \{0,1\}$ - presence or absence of relationship of each surface of the part with the main design basis established by the i-th dimension or requirement [11].

The index of manufacturing manufacturability of a part is proposed, which reflects the possibility of observing the principle of unity of bases in the development of technological process in terms of evaluating the relationships between the surfaces of the part and surfaces that are auxiliary design bases:

$$K_{EOB} = \frac{1}{M}\sum_{i=1}^{M} NOB_i, \tag{2}$$

where $NOB_i \in \{0,1\}$ indicates the presence or absence of interrelation of each surface of the part with auxiliary design bases established by i - size or requirement.

The calculation of the developed indicators of production manufacturability for the part "Cover 2522-4202051" has been performed: $K_{EO} = 0{,}95$, $K_{EOB} = 0{,}92$ [11].

2. Results and Discussions

The development of the technology for selecting a set of bases and basing technology is a solution to a complex complex problem. It is required to find the optimal variant of transition from semi-finished product to finished part that meets all the requirements of its service purpose [29].

Structural accuracy is justified by the conditions of workpiece operation in the assembly, machining capabilities and conditions for obtaining the initial workpiece. When machining on machine tools, the workpieces must be correctly oriented relative to the mechanisms and units of the machine, which determine the trajectories of movement of cutting tools. These include: guides; slides; milling and tool heads; copying devices and others. The tasks of mutual orientation of parts and assemblies in machines during their assembly and blanks on machines during the manufacture of parts are solved by basing. Basis is the provision of the required position of the product relative to the selected coordinate system. When applied to design or assembly, basing means giving the part or assembly unit the required position relative to other parts of the product. When machining workpieces on machine tools, basing is considered to be giving the workpiece the required position relative to the machine elements that determine the trajectories of the machining tool feed. Terms and definitions of the basic concepts of basing and bases are defined by the standard "Basing and bases in mechanical engineering".

The basis of the theory of basing is the concept of a non-free system studied in theoretical mechanics. According to these concepts, the required position or motion of a solid body relative to a selected coordinate system is achieved by imposing geometric or kinematic relationships. A free solid body has six degrees of freedom: displacements along the axes OX, OY, OZ and three rotations around the same axes. When geometric bonds are imposed, the body is deprived of a certain number of degrees of freedom and, if it is deprived of all six degrees of freedom, the body becomes stationary in the OXYZ system. Six connections, depriving the body of motion in six directions, are created by contact of connected bodies at six points. It is considered that the realization of necessary connections is achieved by contact of bodies on surfaces, and the existence of real connections is symbolized by reference points having theoretical character. To give a position to a body (using its planes of symmetry or axes of surfaces), the connections must be imposed directly on the planes of symmetry, axes, lines or points of their intersection. Reference point - a point symbolizing one of the workpiece or product relationships with the selected coordinate system.

To ensure the immobility of the workpiece or product in the chosen coordinate system, six bilateral geometric relationships must be imposed on them, which require a set of bases.

If the workpiece is to have a certain number of degrees of freedom, the corresponding number of degrees is removed. The theory of basing is general and applies to all bodies that can be regarded as solid, including mechanical engineering products in assembly and at all stages of the production process (machining, transportation, inspection, assembly, etc.) [28].

In order to solve the set tasks it is necessary to have the following initial data and materials:

1) assembly and working drawings of the product and the part;

2) specifications, accuracy standards and other data characterizing the service purpose of the part in the working machine, the requirements for the part, identified in the development of the technological process of assembly;

3) the number of parts to be manufactured per unit of time on the unchanged drawing;

4) the conditions in which the technological process should be carried out, the newly designed or operating plant, the composition of the equipment, the equipment of the plant, the equipment of the new plant, the equipment of the new plant. Information of this kind is very extensive and capacious, changing in time in a very short time.

To do this, the technologist needs large amounts of predictive information information information, and various data monitoring systems to be able to update them promptly [29].

Having established the refinements that must be provided between the surfaces of the part as a result of their processing, i.e. knowing the task, it is possible to proceed to the establishment of the sequence of processing of individual surfaces of the part, to the selection of technological bases in accordance with this and to identify the possibility of combining the processing transitions of different surfaces in time.

The most important reason for the lack of workable formal methods of assigning the schemes of basing, installation schemes and processing route of the workpiece, is the imperfection of the provisions of GOST21495-77; until now in the CIS countries there are still complaints about this GOST and disputes, but in numerous works devoted to the theory of basing do not describe the problems that are solved in basing, there is no clear distinction between the concepts of design and real basing, the theoretical scheme of basing and installation in the design, machining, assembly and co-processing.

One of the difficulties in the development of technological processes is the need to take into account the errors [30, 31] that affect the accuracy of technological processes. In this case, the errors arise, first, from the side of the process of development of the technology itself, and second, from the side of the production process [32].

The main causes of static adjustment error of dimensional and kinematic circuits of the technological system are:

1) incorrect choice of technological bases of the object being processed;

2) wrong choice of measuring bases and measuring method;

3) incorrect choice of method and means of static adjustment of dimensional and kinematic chains;

4) incorrect installation of cutting edges of the tool relative to the executive surfaces of the machine that determine its position;

5) incorrect installation and fixing of fixtures used to determine the position of the processed object and the cutting tool;

6) insufficient static (geometric) accuracy of the equipment, fixtures and cutting tools (manufacturing errors, condition, etc.);

7) insufficient qualification and errors of the equipment, fixtures and cutting tools.

The main reasons generating the error of dynamic adjustment of dimensional and kinematic chains of the technological system are:

1) heterogeneity of the material of machined objects;

2) fluctuations of machining allowances;

3) insufficient and variable rigidity of the technological system on the coordinate of relative movement of the cutting tool and the object being machined;

4) changes in the direction and magnitude of forces acting in the machining process;

5) quality and condition of the cutting tool;

6) condition of the equipment and fixtures;

7) temperature of the machined object, equipment, fixtures, cutting and measuring tools and medium, and especially its fluctuations;

8) properties, method of application and amount of lubricating and cooling fluid;

9) incorrect choice of methods and means for measuring the error of dynamic adjustment;

10) vibrations of the technological system;

11) insufficient qualification and errors of the worker or adjuster and a number of other reasons.

Let's consider the influence of installation error on the course of process design. In most cases, the causes of installation error of a machined object are: 1) incorrect selection of technological bases; 2) errors of technological bases (distances, dimensions, relative turns of geometric shape and roughness); 3) errors of the executive surfaces of the machine, fixture or workplace used to determine the position of the machined object; 4) incorrect use of the six-point rule in determining the position of the machined object; 5) incorrect force closure (creating insufficient magnitude, points and sequence of application); 6) incorrect choice of measuring bases, method and means of measurement; 7) unorganized change of bases in the process of fixing the machined object; 8) insufficient qualification of the worker and some others

One of the main reasons generating errors of installation, is the wrong choice of technological and measuring bases, especially at the first operation. Therefore, the role and importance of the first operation is considered first.

In the first operation of manufacturing a part from a workpiece, two main tasks are accomplished:

1) relationships are established that determine the distances and rotations of the surfaces that result from machining relative to the surfaces that remain unmachined;

2) the distribution of the actual machining allowances between the surfaces to be machined.

The correct solution of both problems has a decisive influence on the number of transitions and operations of the technological process, its labor intensity, cycle and cost of processing.

When solving the first problem, we are usually guided by the need to ensure that the part fulfills its service purpose when working in the machine. For some parts, their executive surfaces are left without machining due to the complexity of their shape, while the surfaces of the main and auxiliary bases are machined. If these parts are not machined to the required accuracy, the distances and relative rotations of the actuating surfaces with respect to the surfaces of the main bases, the parts will not fulfill their service purpose correctly.

Some parts have requirements that require these relationships to be established:

1) obtaining uniformity in the wall thickness of a part in order to provide sufficient strength or dynamic balance to the part.

2) Providing the necessary clearance between the free and other surfaces of two parts located or traveling a short distance one from the other when operating in a machine.

In solving the second problem, the first operation is guided by three basic considerations: 1) the need to maintain a dense homogeneous layer of material on the surfaces of the part subjected to the most intensive wear during its operation in the machine, in order to increase their wear resistance; 2) the need for uniform distribution of the machining allowance on each individual surface and primarily on the encompassing and internal surfaces (grooves, cast holes, etc.);

3) the need to increase the productivity of machining by reducing the amount of material to be removed in the process of machining.

The necessity of uniform distribution of machining allowance on each of the surfaces, especially on covering and internal surfaces, is explained by the fact that non-uniform allowance always generates fluctuations of cutting force, causing vibrations and elastic movements in the technological system, generating an increase in the error of dynamic adjustment of dimensional and kinematic chains.

The result is an increase in random machining errors, obtaining incorrect geometric shape of machined surfaces, increase in the size dispersion field, increase in surface roughness, etc.

The need to reduce these errors forces to carry out machining at reduced modes or to introduce additional passes or even whole transitions and operations into the technological process, which is associated with loss of productivity and additional costs.

The need to ensure uniform allowance on internal surfaces (surfaces of grooves, holes, etc.) is primarily due to the fact that the dimensions of holes and grooves limit the geometric dimensions of cutting and auxiliary tools, in particular, mandrels, boring bars etc.

The resulting insufficient rigidity of the tool forces machining at reduced modes or with a large number of passes or transitions, often associated with the change of cutting tools, which causes an increase in labour intensity of machining.

Uniformity of the allowance on the surfaces of parts allows: 1) improve machining accuracy at the first operations and thus reduce the number of passes and transitions; 2) reduce energy costs and equipment amortisation, as machines with lower motor power can be used; 3) increase machining productivity at subsequent operations.

When distributing the machining allowance between several surfaces, especially parallel ones, the largest part of it should be removed from less critical surfaces with smaller overall dimensions, if possible.

All the above tasks are solved at the first operation by correct selection of technological bases.

In order to economically produce good parts, it is necessary to study the influence of all the above factors on machining accuracy in order to be able to manage them to achieve the task by increasing the refinement given by the technological system. Information about these errors is individual - it is specific to a particular plant, process and process system, and is also time variable. To obtain this information requires its collection on the basis of the past and current state of the plant, its analysis and systematisation. At the same time, some of the information changes instantly and cannot be systematised or depends on third-party producers [29].

Installation error is the deviation of the actual position of the workpiece or product achieved during installation from the required position. Basis error is the deviation of the actually achieved position of the workpiece or product during basing from the required position. The required position of the workpiece (product) is understood as such a position of the setting elements that the coordinate system of the workpiece coincides with the coordinate system of the machine or fixture. When machining a batch of workpieces on a tuned machine tool, it is not the actual basing error of each workpiece that is considered, but the basing error - the size dispersion field of all workpieces, which has the smallest and largest limit values. The maximum possible datum errors can be determined for each datuming scheme by calculation [28].

The datum error δb (Figure 6) is characterised by the limit positions of the workpiece bore axis Z_1 relative to the fixture pin axis Z:

$$\delta_{b\ max} = 0 \pm (D_{\ max} - d_{\ min})\ /2 \tag{3}$$

The scheme of cylindrical workpiece installation in the prism for bald milling is shown in Figure 7.

The two circles show the smallest and largest diameter of the workpiece in the batch with axes C‘ and C’‘, When making a dimension, the basing error is determined by the difference in the limiting dimensions from the measuring base (formers A’ and A‘’) to the tool set to the dimension (point A‘’) [28]:

$$\delta b\ h_1 = OA' - OA'' = TD\ /2\ (1/\sin\alpha/2 + 1),$$

By analogy for dimensions h_2 and h_3:

$\delta b\ h_2 = TD\ /2 \cdot (1/\sin\alpha/2 - 1)$; $\delta b\ h_3 = TD\ /2 \cdot 1/\sin\alpha/2$

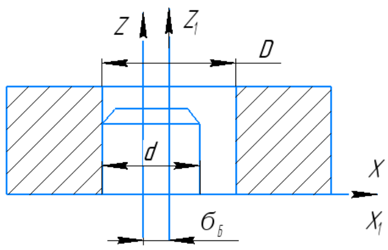

Fig. 6. – Occurrence of a datum error:
Z - fixture coordinate system; Z_1 - workpiece coordinate system

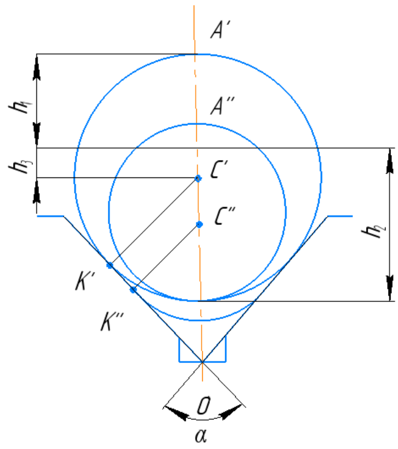

Fig. 7. – Occurrence of basing errors

The basing error can be reduced and even eliminated either by selecting a more correct basing scheme or automating the process, or by making the base elements of the fixture more accurate to the workpiece itself (base hole diameter). For example, mandrels with a taper of 1.5° ... 5.0° are used in order to eliminate the gap in the joint, for example, unclamping mandrels of collet and cam type or hydroplastic mandrels.

The clamping error is caused by the displacement of the workpiece or its elastic deformations under the action of clamping forces. Due to fluctuations in compressed air pressure in the network, oil pressure in hydraulic systems, fluctuations in magnetic, electromagnetic or manual clamping forces, clamping forces are not constant. Elastic forces are also variable due to variations in physical and mechanical properties and dimensions in workpiece cross-sections. In the practice of predicting the clamping error, the data of average error scatter fields for typical fixtures are given. This error, like the basing error, is only part of the total fixture error. The scattering field of installation error is equal to the sum of scattering fields of all errors: basing, clamping and fixture [28, 33, 34].

A great contribution to the development of the school of computer-aided design was made by scientists Shvoev V.F., who was directly engaged in the development of methodology of systems of computer-aided design of technological processes of mechanical processing, Zhetesova G.S. - development of mathematical models and software for design and technological support for the production of mining equipment, Nikonova T.Yu. [35] - development of mathematical models and software for processing by methods of plastic deformation, Yurchenko V.V. [29]- was engaged in the development of systems of computer-aided design of technological processes of mechanical processing of parts of mining machines. However, so far, as the analysis of existing CAD systems has shown, the possibility of objective decision making has not been solved.

Thus, based on the analysis of the theoretical foundations of technology design and computer-aided design systems, the following conclusions can be drawn:

- the solution of the majority of automated technological design tasks is based on the use of professional knowledge and experience of the designer, i.e. trained and constantly improved specialised human intelligence;
- the formulation of the overwhelming number of design tasks is difficult or non-formalisable;
- decision-making is based on the use of TTP, GTP and CTP;
- the existing theoretical and methodological bases of design do not allow to develop CAD TA that meet the requirements of modern production [29].

Conclusions

The developed quantitative indicators for the assessment of manufacturing manufacturability significantly deepen and expand our knowledge gained in the process of working with manufactured parts. They help to take into account the peculiarities of technological preparation, especially in the conditions of production of diverse products, which makes them indispensable in modern industry.

The obtained results and created forma lised methods of using new quantitative indicators allow making forecasts at early stages of formation of technological processes of parts manufacturing regarding the probability of using optimal technological bases. Together with the already existing indicators they provide a more detailed view of the compliance of the design of manufactured parts with the requirements and processing methods, which allows making more accurate and well-founded predictions about the performance of production systems in the manufacture of specific parts.

References

[1] Azretbergenova G., Nakipbekova S., Turysbekova G. Direction of development of Kazakhstan in accordance with the fourth industrial revolution // Economic series of the bulletin of Gumilyov ENU, volume 141, № 4, 2022.
[2] Savelyeva N., Nikonova T., Zhetessova G., Khrustaleva I., Yurchenko V, Cˇernašejus O., Zharkevich O., Dandybaev E., Berg A., Vassenkin S., Baimuldin M. Implementation of Simulation Modeling of Single and High-Volume Machine-Building Productions // Designs, 2024, 8(2), 24
[3] Vasiliev A. S., Dalsky A. M., Zolotarevskii Y. M.. Kondakov A. I. Directed formation of properties of mechanical engineering products - M.: Mashinostroenie, 2005. - 352 p.
[4] Suslov A. G. Technology of mechanical engineering: textbook. - M. Knorus, 2013. – 336 p.
[5] Bagrov B. Ensuring manufacturability of the product design //Science-intensive technologies in mechanical engineering, № 8 (110), 2020. - P. 18-22.
[6] Bezjazychny V. F. Fundamentals of engineering technology: a textbook for universities. 3rd hyd. - M.: Innovatsionnoe mashinostroenie, 2020. – 568 p.
[7] Mitin S.G., Bochkarev G.K., Bokova L.G. Automatisation of an estimation of production manufacturability of a product in conditions of multinomain production systems. Science-intensive technologies in mechanical engineering, 2014, № 9 (39). – P. 44-48.
[8] Bokova L. G., Bochkarev P. Yu. Development of indicators to assess the production manufacturability of parts in the system of planning technological processes of machining // Vector of Science of Togliatti State University. 2015, № 3-1 (33-1). - P. 29-35.
[9] Bokova L. G., Bochkarev P. IO., Korolev R. D. Estimation of production manufacturability of parts in the planning system of multinomain technological processes: textbook - Saratov: Izd-vo Saratov State Technical University, 2018. – P. 12 - 17
[10] Bochkarev P. Ю., Bokova L. G. Estimation of production manufacturability of parts under conditions of multitoned machining systems //Bulletin of Rybinsk State Aviation Technological Academy named after P. A. Solovyov, 2017, № 1 (40). - P. 250-254.
[11] Bochkarev K., Korolev R.D., Bokova L.G. Provision of principles of basing of machined parts at estimation of production manufacturability //Izvestiya vysshee obrazovaniya vysshee obrazovaniya. Povolzhsky region. Technical Sciences, 2, 2022, P. 82 - 91.
[12] Nikonova T.Yu., Kabidenov D.K., Abdugalieva G.B., Berg A.S., Imasheva K.I. Processing of a Part Such //Material and Mechanical Engineering Technology, 1, 2024. - P. 21 - 29.
[13] Chernorutsky I., Kotlyarov V., Shyamasundar R., Tolstoles A., Voinov N. Implementation of reliable net-centric management of IoT industrial workshop for small-scale production //IOP Conf. Ser. Mater. Sci. Eng., 2018, 497, 012040.
[14] Manzei, C., Schleupner, L., Heinze, R. Industrie 4.0 im Internationalen Kontext: Kernkonzepte, Ergebnisse, Trends; VDE VERLAG GmbH: Berlin, Germany, 2016. - 261 p.
[15] Marcos, M.P.; Pitarch, J.L.; de Prada, C. Integrated Process Re-Design with Operation in the Digital Era: Illustration through an Industrial Case Study //Processes, 2021, 9, 1203.
[16] Bako, B.; Božek, P. Trends in simulation and planning of manufacturing companies //Procedia Eng. 2016, 149, P. 571-575.
[17] Chlebus E, Krot K. CAD 3D models decomposition in manufacturing processes //Arch. Civ. Mech. Eng., 2016, 16, P. 20-29.
[18] Adam R., Kotze P., Merwe A. Acceptance of enterprise resource planning systems by small manufacturing Enterprises // Proceedings of the 13th International Conference on Enterprise Information Systems, Beijing, China, 8–11 June 2011, Volume 1, P.238 - 240
[19] Browne J., O'Kelly M.E.J., Davies B.J. Scheduling in a batch or job shop production environment //Eng. Manag. Int, 1982, 1, P. 173–184.
[20] Rosova A., Behun M., Khouri S., Cehlar M., Ferencz V., Sofranko M. Case study: The simulation modeling to improve the efficiency and performance of production process // Wirel. Netw, 28, 2022, P. 863–872.

[21] Pompeev K.P., Timofeeva O.S., Yablochnikov E.I., Volosatova E.E. Methods of Parts Digital Models Design for Problems Resolving in Technological Preparation of Production. In Advances in Mechanical Engineering; Lecture Notes in Mechanical Engineering; Evgrafov, A.N., Ed.; Springer: Berlin/Heidelberg, Germany, 2022, P. 129–139.
[22] Burkatovskaya Y.B. Graph theory. Part 1: textbook. - Tomsk: Izd-vo Tomsk Polytechnic University, 2014. - 200 p.
[23] Chen Z., Bao J., Zheng X.; Liu T. Assembly information model based on knowledge graph // J. Shanghai Jiaotong Univ, 2020, 25, 578–588.
[24] Li X., Zhang S., Huang R., Huang B., Xu C., Kuang B. Structured modeling of heterogeneous CAM model based on process knowledge graph //Int. J. Adv. Manuf. Technol. 2018, 96, 4173–4193.
[25] Xu Z., Liu H., Li, J.; Zhang, Q.; Tang, Y. CKGAT: Collaborative Knowledge-Aware Graph Attention Network for Top-N Recommendation //Appl. Sci. 2022, 12, 1669.
[26] Han, Z., Mo, R., Hao L. Clustering and retrieval of mechanical CAD assembly models based on multi-source attributes information //Robot. Comput. Integr. Manuf. 2019, 58, 220–229.
[27] Stavropoulos P., Papacharalampopoulos, A., Sabatakakis K. Data Attributes in Quality Monitoring of Manufacturing Processes: The Welding Case //Appl. Sci. 2023, 13, 10580.
[28] Guzeyev V.I. Theoretical bases of parts basing and calculation of dimensional chains in machining. Tutorial. - Chelyabinsk: Publishing Centre of SUSU, 2013. - 178 p.
[29] Nikonova T., Zharkevich O., Dandybaev E., Baimuldin M., Daich L., Sichkarenko A., Kotov E. Developing a measuring system for monitoring the thickness of the 6 m wide hdpe/ldpe polymer geomembrane with its continuous flow using automation equipment //Applied Sciences (Switzerland), 2021, 11(21), 10045
[30] Belyakov N. V. Formalisation of design of technological processes of mechanical processing of case details of machines // UE ‘VGTU’. - Vitebsk, 2006. – 147 p.
[31] Yashcheritzyn P. I., Ryzhov E. V., Averchenko V. I. Technological heredity in mechanical engineering. - Minsk: Nauka i tekhnika, 1987. - 256 p.
[32] Vasiliev A.S., Dalsky A.M., Zolotarevsky Y.M. Directed formation of properties of machine-building products. – M.: Mashinostroenie, 2005. - 562 p.
[33] Scherbakov N.P. Automation of technological design: Manual. - Barnaul: Izd-vo AltGTU, 2002. – 434 p.
[34] Kapustin N.M., Kuznetsov P.M., Skhirtladze A.G. et al. Automation of production processes in mechanical engineering: Training, for universities. – M.: Vysh, shk., 2004. - 415 p.
[35] Yurchenko V.V., Shvoev V.F., Nikonova T.Y. Main directions of CALS-technologies development in the Republic of Kazakhstan //Collection of abstracts of reports. III All-Russian interuniversity scientific conference ‘Science and education in the development of industrial, social and economic spheres of Russian regions’: III All-Russian scientific Zvorykin readings. - Murom: Izd.-polygraphic centre of MI VlSU, 2011. - P. 313-315.

Information of the authors

Berg Alexandra Sergeevna, PhD, assistant, Abylkas Saginov Karaganda Technical University
e-mail: kibeko_1995@mail.ru

Nurzhanova Oxana Amangeldyevna, PhD, senior lecturer, Abylkas Saginov Karaganda Technical University
e-mail: nurzhanova_o@mail.ru

Turla Vytautas, d.t.s., professor, Vilnius Gediminas Technical University
e-mail: vytautas.turla@vilniustech.lt

Berg Andrey Alexeyevich, doctoral student, Abylkas Saginov Karaganda Technical University
e-mail: 22526633@mail.ru

Vitushenko Denis Valeryevich, student, Abylkas Saginov Karaganda Technical University
e-mail: kibeko_1995@mail.ru

DOI 10.52209/2706-977X_2024_2_36 IRSTI 55.13.99 UDC 621.923

The Mechanism of Orientation of Ferro-abrasive Grains in the Working Gap During Magnetic Abrasive Treatment

Akulovich L. M.[1], Sergeev L. E. [1], MendalievaS. I. [2], Sherov K. T. [2*], Mazdubai A.V.[3] Tussupova S.O.[3], AinabekovaS.S.[4]
[1]Belarusian Agrotechnical University, Minsk, Republic of Belarus
[2]S.Seifullin Kazakh Agro-Technical Research University, Astana, Republic of Kazakhstan
[3]Toraighyrov University, Pavlodar, Republic of Kazakhstan
[4]Karaganda industrial university, Temirtau, Republic of Kazakhstan
*corresponding author

Abstract: The purpose of the article is to study the orientation of ferro-abrasive grains in the working space at MAT to determine the possibility of controlling this process.The article examines the behavior of ferro-abrasive grains in the working space during magnetic abrasive processing. Theoretical studies have been carried out to identify the parameters that affect the effectiveness of surface treatment of the part. The modeling of the cutting process by ferro-abrasive grain of the treated surface is based on the shape of a triaxial ellipsoid. The cutting scheme and the acting forces in the working space of the MAT are given. The expediency of oriented cutting and control of the angle of inclination of ferro-abrasive grains to intensify the cutting of the allowance for MAT is substantiated. The influence of the angle of inclination of ferro-abrasive grains on the cutting process is considered from the standpoint of the basic provisions of the cutting theory.

Keywords: magnetic abrasive treatment, ferro abrasive grain, ferro-abrasive powder, triaxial ellipsoid, microhardness, friction force, coefficient of friction, angle of inclination, cutting force.

Introduction

The cutting process under MAT is influenced by the shape of the ferro-abrasive grains FAG [1]. The geometric parameters of ferro-abrasive grains determine its cutting ability, which depends on the number of cutting edges, on the corners at the vertices and the radii of rounding of the vertices.

The shape of ferro-abrasive grains depends on the powder manufacturing technology, materials of magnetic and abrasive components and has, as a rule, an irregular geometric shape. Depending on the method of manufacturing powders, two typical forms of phases can be distinguished:

– fragmentation (Fig.1), obtained after grinding granular materials based on amorphous iron (powders of the POLYMER-T type) [1];

– rounded (Fig. 2), obtained from a melt without subsequent grinding (powders of type P6M5, POLYMER-M) [1].

a)

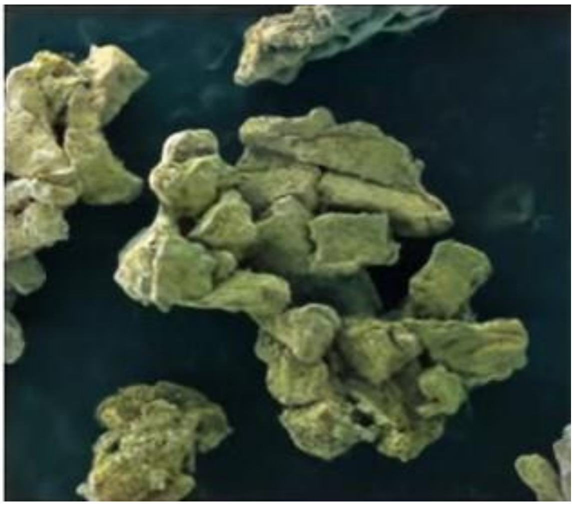

b)

Fig. 1. - Photos of splinter-shaped FAP (×500): a) FeTiC; b) diamond-based powder

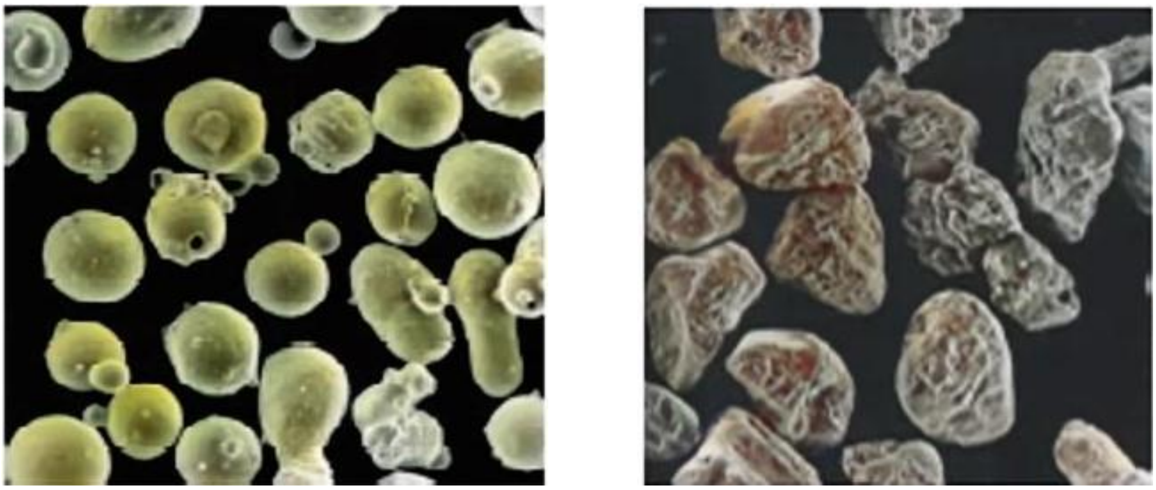

a) b)

Fig. 2. - Photographs of rounded FAP (×400) a – powder R6M5; b – powder TSARAMAM

FAP of the same composition can have different geometric shapes, which is due to the method of their manufacture, the type of additional processing, the size of the fraction and other factors [1].

The ability of the FAP to seal in the working gap at MAT depends on the shape of the ferro-abrasive grains. The shape of ferro-abrasive grains also affects their ability to rotate relative to the treated surface under the influence of a magnetic field during the MAT process.

According to [2], it is preferable that the shape of ferro-abrasive grains approach the shape of regular geometric shapes. This is due to the fact that rounded particles provide increased polishing ability due to the care of the treated surface of the parts, unlike the shapes of fragmented grains and conglomerate grains.

Each ferro-abrasive grain has, as a rule, several vertices formed by faces (chips) with certain radii of their rounding. The number of vertices in the abrasive grain, the angles at the vertices and the radii of rounding depend on the grade of the FAP, its grain size and the manufacturing method. According to [3], the magnitude of the angles at the vertices is in the range from 30° to 130°.

1. Methodology

The efficiency of MAT depends on the shape and size of the ferro-abrasive grains, their granulometric composition, the chemical activity of the processed material, and the microhardness of the abrasive component. Since when a grain enters a magnetic field, its largest axis is oriented in the direction of the field lines, it is preferable to use a stretched or fragmented grain shape, which facilitates the process of their reorientation during processing.

From the analysis of the geometry of the ferro-abrasive grains, it follows that they are granules of irregular angular shape with many protrusions and depressions. The morphology of the ferro-abrasive grains determines the options of their ordered packing, aggregation in the colony when forming an abrasive brush.

When modeling the contour of a cutting tool with different profile surfaces, it is convenient to represent the shape of the phase in the form of a regular geometric shape approximating oval, elliptical, spindle-shaped, lamellar.

Therefore, as a generalized model of the FAG of these shapes, it is advisable to take the form of a triaxial ellipsoid, the surface of which contains microparticles of an abrasive component. The shape of such a model is similar to a geoid, the surface of which contains abrasive particles (Fig. 3) [4].

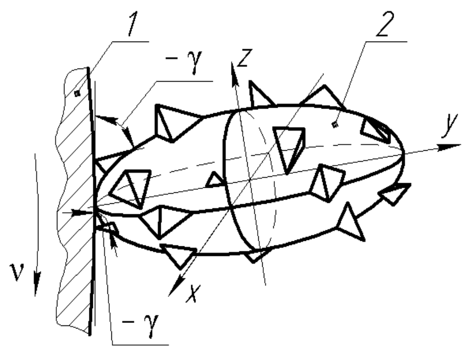

1 – the surface to be processed; 2 – ferro-abrasivegrain;v – the speed of the main movement; γ – the front angle

Fig. 3. - A model of the shape of a ferro-abrasive grain of its location in the MAT process

In the classical MAO scheme, the front angle γ of the cutting elements of the ferro-abrasive grain has negative values.When choosing a generalized model of the ferro-abrasive grain shape, the following assumptions were introduced:

1) ferro-abrasive grain is a triaxial ellipsoid, the equation of which has the form:

$$\frac{x^2}{a^2}+\frac{y^2}{b^2}+\frac{z^2}{c^2}=1 \tag{1}$$

where a is the small semi-axis of the ellipsoid, mm;
b is the large semi-axis of the ellipsoid, mm;
c is the middle half-axis of the ellipsoid, mm.

2) the dependence of the magnitude of the semi-axes of a triaxial ellipsoid on the grain size of the FAP is described by the expression

$$c=(a+b)/\,2 \tag{2}$$

2. Results and Discussions

Let's consider the general scheme of cutting with a single ferro-abrasive grain, the location of which relative to the treated surface is shown in Fig. 4 [4].

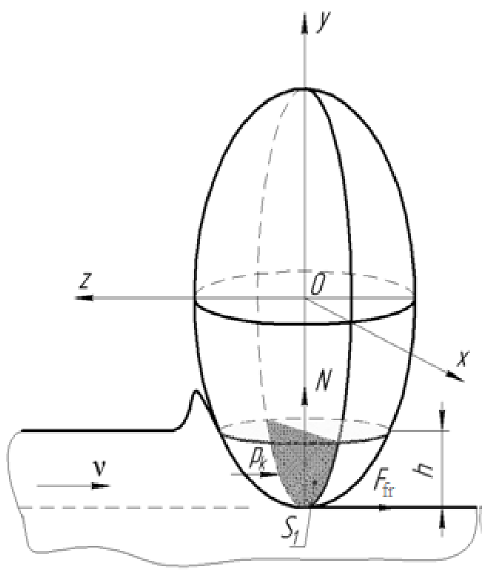

Fig. 4. - Cutting scheme with a single ferro-abrasive grain at MAT

The following forces act on the FAG:
--the reaction force of the treated surface N, equal to the value of the normal component of the magnetic field strength F_m (ΔB_1);
-the friction force F_{fr} between the FAG and the treated surface, which is set by the ratio:

$$F_{fr}=\mu N=\mu F_m(\Delta B_1), \tag{3}$$

where μ - coefficient of friction on the contact surface;

N - total normal pressure p_k, along the contact surface acting on the area located in the normal phase section and enclosed between the contact spot of the ferro-abrasive grain with the treated surface and the plane determining the value of the layer to be removed h by a single grain of FAP at a given time.

With respect to the parameters acting on a single FAG, the following assumptions are made:

1) The stress distribution over the surface of the FAG in the cutting area is uniform;

2) The stress on the surface of the cutting zone is proportional to the hardness of the material being processed.

3. The coefficient of friction μ does not change over the entire surface of the contact between the phases and the workpiece.

Thus, the projection components of the cutting force acting on the FAG at MAT in the direction of the *z* and *y* axes can be expressed by dependencies [4]:

$$\mathrm{P_z = p_k S_1 + F_{fr}}, \tag{4}$$

where S_1 - value of the cross-sectional area, which is affected by the total voltage across the contact surface, mcm^2.

$$P_y = N, \tag{5}$$

The size of the cross-sectional area can be calculated using the formula [4]

$$S_1 = \int_{-b}^{-b+h} dy \int_{-a\sqrt{1-\frac{y^2}{b^2}}}^{a\sqrt{1-\frac{y^2}{b^2}}} dx \tag{6}$$

where *b* and *a* are the major and minor semi-axes of a triaxial ellipsoid, microns.

Given the symmetry of the ellipse with respect to both axes, we can write:

$$S_1 = \int_{-b}^{-b+h} dy \int_{-a\sqrt{1-\frac{y^2}{b^2}}}^{a\sqrt{1-\frac{y^2}{b^2}}} dx = 2\int_{b-h}^{b} dy \int_{0}^{a\sqrt{1-\frac{y^2}{b^2}}} dx = 2\int_{b-h}^{b} dy\,(x)\Big|_0^{a\sqrt{1-\frac{y^2}{b^2}}} =$$

$$= 2\int_{b-h}^{b} a\sqrt{1-\frac{y^2}{b^2}}dy = 2\int_{b-h}^{b} \frac{a}{b}\sqrt{b^2-y^2}dy =$$

$$= \left| \begin{matrix} y = b\sin t \\ dy = b\cos t dt \\ y = b \Rightarrow t = \frac{\pi}{2} \\ y = b-h \Rightarrow t = \arcsin\frac{b-h}{b} \end{matrix} \right| =$$

$$= 2\int_{\arcsin\frac{b-h}{b}}^{\frac{\pi}{2}} \frac{a}{b}\sqrt{b^2-b^2\sin^2 t}\; b\cos t\, dt =$$

$$= 2\int_{\arcsin\frac{b-h}{b}}^{\frac{\pi}{2}} \frac{a}{b} b^2\cos^2 t\, dt = 2ab\int_{\arcsin\frac{b-h}{b}}^{\frac{\pi}{2}} \cos^2 t\, dt =$$

$$= 2ab \int_{\arcsin\frac{b-h}{b}}^{\frac{\pi}{2}} \frac{1+\cos 2t}{2} dt = ab\left(t + \frac{1}{2}\sin 2t\right)\Big|_{\arcsin\frac{b-h}{b}}^{\frac{\pi}{2}} =$$

$$= ab\left(\frac{\pi}{2} - \arcsin\frac{b-h}{b} - \frac{1}{2}\sin\left(2\arcsin\frac{b-h}{b}\right)\right) =$$

$$= ab\left(\frac{\pi}{2} - \arcsin\frac{b-h}{b} - \frac{b-h}{b}\sqrt{1-\left(\frac{b-h}{b}\right)^2}\right) =$$

$$= ab\left(\arccos\frac{b-h}{b} - \frac{b-h}{b}\sqrt{1-\left(\frac{b-h}{b}\right)^2}\right) \quad (7)$$

In formula (7), the thickness of the cut layer *h* can be determined from Kick's law [5] if the ferro-abrasive grain is likened to an indenter:

$$\mathrm{h} = \sqrt{\frac{\mathrm{P_g}}{\mathrm{c_g}}} \quad (8)$$

where P_g - insertion force, it will be equal to the magnetic field strength F_m, N;

c_g - coefficient depending on the angle of FAG insertion and the elastic–plastic properties of the material into which it is pressed.

The angle of ferro-abrasive grain insertion also depends on the angle of inclination of the axis of the ferro-abrasive grain relative to the treated surface. It follows from formula (8) that the thickness of the cut layer is influenced by the angle of inclination of the axis of the ferro-abrasive grain. Consider this influence.

In the middle part of the working gap, the magnetic lines of force are directed perpendicular to the surface to be processed (Fig. 4). Accordingly, the largest axis of the ferro-abrasive grain is directed. When changing the direction of the magnetic force lines by an angle of *ω*, the abrasive grains also rotate their largest axis by the same angle (Fig. 5).

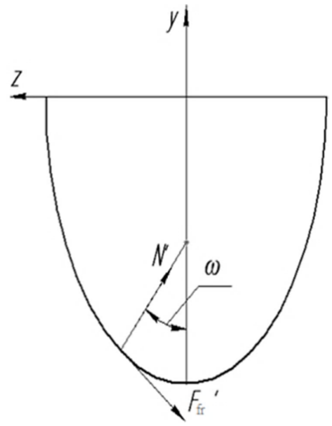

Fig. 5. - Diagram of forces acting on the lateral surface of the FAG N' is the normal reaction force acting on the ferro-abrasive grain from the side of the processed material; F_{fr}' is the friction force

Consider the effect of cutting forces on a ferroabrasive grain when its angle of inclination*ω* changes. Force projections on the Z axis:

$$\mathrm{N}_z^{'} = \mathrm{N}^{'}\sin\omega, \quad (9)$$

$$\mathrm{F}_{\mathrm{fr}\,z}^{'} = \mathrm{F}_{\mathrm{fr}}^{'}\cos\omega \quad (10)$$

Summing the vectors *N'* and F_{fr}' on the half-meter, taking into account the change in the angle *ω*, we obtain the sum of their integral absolute values [6]:

$$\left|\int_{90^\circ}^{0^\circ} N^{'} \sin\omega d\omega\right| + \left|\int_{90^\circ}^{0^\circ} F_{fr}^{'} \cos\omega d\omega\right| = N^{'} + F_{fr}^{'}. \quad (11)$$

Normal forces can be determined through the normal pressure $p_{N'z}$, and the friction force can be determined through the tangential stress $p_{F'fr}$. In turn, the normal pressure is proportional to the hardness of the processed material, as shown in the expression [6]:

$$p_{N_z^{'}} \approx \beta \cdot H_V \quad (12)$$

where H_V - hardness of the treated surface on the Vickers scale, MPa;

β - constant expressing the ratio of the values $p_{N'z}$, and H_V.

For example, according to the literary source [7], the value β = 1÷ 1.23.We take a lower limit value, then β = 1, i.e. the normal pressure on the grain surface is equal to the hardness of the material being processed.

The tangential stress is expressed in terms of the normal stress and the coefficient of friction according to the formula

$$p_{F_{fr}^{'}} = \mu p_{N_z^{'}} \quad (13)$$

Taking into account the expressions (4), (5), (11), (12) the component of the cutting force P_z acting on a single grain can be described by the dependence:

$$P_z = H_V \cdot (1 + \mu) S_1 + \mu F_m(\Delta B_1), \quad (14)$$

$$P_y = F_m(\Delta B_1) \quad (15)$$

On the other hand, summing up the projections of the forces N' and F_{fr}' on the z axis and taking into account (3), we obtain the cutting force:

$$P_z^{'} = N_z^{'} + F_{fr}^{'} = N^{'}(\sin\omega + \mu\cos\omega) \quad (16)$$

The value of P_y'at MAT is always equal to the magnitude of the magnetic field strength. With the constant strength of the magnetic field, according to formula (12), the ferro-abrasive grain will be embedded in the treated surface to a depth determined by the elastic-plastic properties of the treated material. [8,9,10]

Thus, the expediency of oriented cutting and control of the angle of inclination of ferro-abrasive grains to intensify the cutting of the allowance at MAT is theoretically justified. Let's consider the influence of the angle of inclination of ferro-abrasive grains on thecutting process from the standpoint of the basic provisions of the cutting theory. An increase in the angle of inclination of the grains ω leads to an increase in the shear angle β_1 and a decrease in the cutting angle (Fig. 6).

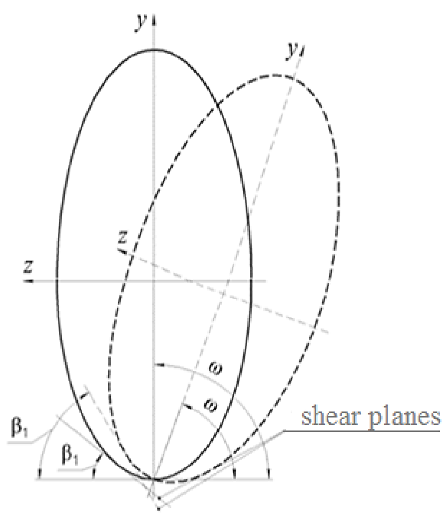

Fig. 6. - Directions of the chip shear plane when the angle of inclination of the ferro-abrasive grain changes

Reducing the cutting angle facilitates the chip removal process and reduces the cutting force P_z. However, the radius of rounding of the cutting edge must be taken into account.

The shape of the ferro-abrasive grain in the form of a triaxial ellipsoid has a different curvature along the contour. The radius of rounding has the smallest value at the intersection point of the ellipse with the largest half-axis b. The possible contact zones of the FAP grain with the treated surface are within half of the perimeter of the contact zone, which corresponds to a change in the boundary values of the angle ω from90^o to 0^o. The refore, it is necessary to introduce a technical restriction on the angle of inclination of the grain ω. The problem can be solved theoretically or graphically using the ellipse construction method.

In the first case, it is necessary to determine the coordinates (y_0 z_0) of the intersection point M_0 of the large and small circles approximating the ellipse curve by solving a system of equations:

$$\begin{cases}(z+z_1)^2+y^2=R_1^2\\ z^2+(y-y_2)^2=R_2^2\end{cases} \tag{17}$$

where $R_1$and R_2 - radii of the large and small circles, microns.

Then determine the equation of the tangent to the small circle at the point M_0(18) and its angle of inclination to the axis oy:

$$\begin{aligned}yy_0+zz_0=R_1\\ yy_0+zz_0=R_1\end{aligned} \tag{18}$$

The analysis of the above dependencies (17 and 18) shows that the boundary value of the rotation angle depends on the ratio of the semi-axes of the ellipsoid a, b and c. The accepted shape of the triaxial ellipsoid is generalized. If the half axes are equal, the ferro-abrasive grain will have a spherical shape, and if the 2 axes are equal, the ellipsoid of rotation.

Therefore, it is advisable to take the average shape of a ferro-abrasive grain in the form of a triaxial ellipsoid with a half-axis ratio b = 1 : c = (b+a)/2 : a = 0,25. With this assumption, the boundary value of the angle of inclination of the ferro-abrasive grain, equal to 58°, was determined using the graphical method.

Thus, the components of the force depend on the tilt of the axis of the ferro-abrasive grain relative to the treated surface, as well as on the coefficient of friction in contact with the treated surface, on the hardness of the processed material and the size of the layer to be removed by a single grain.

Conclusions

Based on the dependencies obtained, the following conclusions can be drawn:

– it is technologically difficult or impossible to control the amount of cutting forces by changing the coefficient of friction in contact of the ferro-abrasive grain with the surface to be processed;

– the hardness of the processed material is a constant value (specified in the design documentation);

– the value of the allowance to be removed is determined by the component of the cutting force P_y, depending on the magnitude of the magnetic induction;

– changing the cutting forces is accessible and technologically easy to implement by controlling the magnitude of magnetic induction and the angle of orientation of the ferro-abrasive grain relative to the surface to be processed, which affects the value of the leading angle of the cutting edge.

Referance

[1] Akulovich L.M. Ferroabrasive powders for magnetic abrasive treatment of metal surfaces. Minsk: BSATU, 2015. - 284 p.
[2] Radomyslsky I.D., Tuchinsky L.N. Powdered magnetic materials. - Kiev: Naukova dumka. 1984. - 142 p.
[3] Chernyavsky P.A. New in magnetic methods of investigation of metallized catalysts //Russian Chemical Journal, vol. 17, no. 6, 2002, P.19-30
[4] Voroshukho O.N. Technology of magnetic abrasive treatment of external cylindrical surfaces with controlled orientation of ferroabrasive grains and regeneration of an abrasive brush by a pulsed magnetic field: abstract of the dissertation of the candidate of technical sciences. - Minsk: BNTU, 2019, 27 p.
[5] Fedosov S.A. Determination of mechanical properties of materials by microindentation: Modern foreign methods. - M.: Faculty of Physics of Moscow State University, 2004. - 100 p.
[6] Shavva M.A. Analysis of the relationship between wear of the circle and cutting forces during diamond grinding // Science and education of Bauman Moscow State Technical University, 11, 2014, P. 137-156
[7] Akulovich L.M., Sergeev L.E. Fundamentals of profiling of cutting tools in magnetic abrasive processing. Minsk: BSATU, 2014. - 280 p.

[8] Akulovich L.M., Sergeev L.E., Mendaliyeva S.I., Sherov K.T., Features of Magnetic Field Modeling for Magnetic-Abrasive Treatment of Complex-Profile Surfaces //Material and Mechanical Engineering Technology, vol. 40, 2022, P. 37–42
[9] Arystanov Z., Togizbayeva B., Karazhanov A., Alipbayev Z., Burkanova K. Investigation of the impact of operating conditions on the service life of locomotive wheelset tyres //Journal of the Balkan Tribological Association, 2022, 28(6), P. 882–896.
[10] Sherov K.T., Mussayev M.M., Zharkevich O.M. Features of chip formation during thermal friction milling //Material and Mechanical Engineering Technology, №3, 2021, P. 17-21

Information of the authors

Akulovich Leonid Michailovich, d.t.s., professor, Belarusian Agrotechnical University
e-mail: leo-akulovich.tm@bsatu.by

Sergeev Leonid Efimovich, c.t.s., associate professor, Belarusian Agrotechnical University
e-mail: sergeev.tm@bsatu.by

Mendalieva Saule Ilyinichna, c.t.s., senior lecturer, Seifullin Kazakh Agro-Technical Research University
e-mail: s.mendalieva@kazatu.edu.kz

Sherov Karibek Tagaevich, d.t.s., professor, Seifullin Kazakh Agro-Technical Research University
e-mail:shkt1965@mail.ru

Mazdubai Asylhan Vladimirovich, PhD, Ass. Professor, Toraighyrov University
e-mail: asylkhan_m@mail.ru

Tussupova Sayagul Oralovna, PhD, senior lecturer, Toraighyrov University
e-mail: suleeva.s@inbox.ru

Ainabekova Saule Serikbaevna, PhD, senior lecturer, Karaganda Industrial University
e-mail: asaules@mail.ru

DOI 10.52209/2706-977X_2024_2_44 IRSTI 55.03.14 UDC 621.01

Strength analysis by the Finite Element Method (FEM) of a modular line

Marcinkiewicz J. *, Spadło M., Staszak Ż.
Poznan University of Technology, Poznan, Poland
*corresponding author

Annotation. The aim of the work is the strength analysis of structural elements of a modular line. Within the subject, an assessment of the structural strength state was made using the finite element method. For the purpose of the work, the following computational models were developed: the load-bearing frame of a charging hopper, the load-bearing frame of a screen as well as the load-bearing structure of wheels. The problem of load transfer between components occurring in mutual contact was discussed. Multi-variant strength calculations were performed later and stress patterns were determined for all the most important operating cases. The final stage of the work was the verification of the adopted design assumptions in terms of stress with the results obtained during the tests.

Key words: finite element method, FEM, strength analyse

Introduction

The first information on application of finite elements was available in the mid-60s in 20th c. At the beginning they were used in mechanics and the machine and construction facilities' design process. However, the complicated boundary conditions made formulating issues concerning a mathematical analysis impossible. Mathematics development allowed of changing the problem description from the analytical to algebraic form and of applying this solution to issues related to mechanics [1].

The Finite Element Method (FEM) allows of physical calculations based on the discretisation of an area with a finite number of elements averaging the body physical state. The finite element is understood as the sub-area of the discretised continuum. Its dimension is finite and its shape is simpler than the geometric shape of the examined object [2, 7]. The particular elements should be small in size so that the base functions approximated in them could be approximated by means of polynomials, but they must differ from zero, whereas the base elements should be simple solids while discretising space or simple figures while discretising surfaces [1-3, 33, 35-37].

The selection of points for analysis, called nodes, aims at determining the input function conditions of compatibility and equilibrium, whereas each of the nodes is characterised by an appropriate number of degrees of freedom. There are six degrees of freedom for solid elements, hence a three-dimensional model, while for flat elements the number of degrees of freedom is three and a two-dimensional model is created. The accuracy of the solution depends on the shape function, i.e. the accuracy of the approximation of physical quantities inside the element [2-4, 32, 38-40].

The shape functions should meet the following assumptions: there is no need for continuity of derivatives between the elements, the matrix of the whole system is created on the basis of the matrix of elements. This allows the basic system of equations to be solved and on the basis of determined nodal parameters derivative functions are calculated [1, 5].

Computer programmes making FEM calculations consist in preparing the calculation process, building and solving an appropriate system of equations which can be presented in the form of print-outs or graphs [3-4].

The finite element method is used by Hou et al. [14] to analyse the helical gear mesh stiffness. Tan, et al. [15], uses the FEM to locate mechanical damage, whereas Hakula and Lakksonen [16] to analyse perforated material damage. The finite element method is also applied in the shipbuilding industry, e.g. when evaluating the thermal properties of fire doors on a ship [17]. The described method does not only concern steel materials, but can also be used for the analysis of building materials in order to assess their strength [18] and for the analysis of reinforced concrete elements [19-20] used during the construction of large buildings.

The finite element method is used much more often while designing machines and equipment. Azarinfar and Aghaebrahimi [21] applied it to calculate the disk rotor using permanent magnets with cross-flow. Ścieszka and Żołnierz [22] used the finite element method to calculate the effect of the hoisting machine disk brake design on its thermal-elastic instability. This method is also used during the cracking analysis of machine elements [23,25,34,41] and issues related to the contact of machine elements [24,31,35,42].

The finite element method used for the stress analysis requires a lot of work on model preparation and synthesis of results [43]. It is now an integral part of the design process [44]. It is applied in the stress analysis in complex mechanical systems [45-46]. Due to the FEM, it is possible to examine the strength of the structure, its dynamics, stresses, displacements, kinematics and statics, simulate deflections and check the flow of liquids and heat [47]. Apart from its application in many fields of technology, it is also used in bioengineering and medicine [6-8].

1. Purpose and Scope of work

The investigated constructions were designed as space frame systems which are the basic load-bearing system for the charging hopper (Fig. 1) and the vibrating screen (Fig. 2). Due to the nature of input functions, the adopted construction solutions were selected in order to ensure full structure stability even in unstable foundation conditions on demanding ground therefore most of the structural joints are designed as welded joints. In the structure of both frame structures, as the basic construction elements there were used I-section stringers connected with crossbars and reinforced columns, which were reinforced with braces at critical points. For strength reasons, the number of bolted joints is limited to the minimum to maintain the proper functionality of the designed structures [9-10].

Strength considerations also regarded a driving unit, additional equipment of the discussed frame systems (Fig. 3) which is an innovative solution on the market and can also be used as a bogie for transporting heavy and bulky materials. The construction supported by eight wheels in twin subsystems was designed to guarantee the mobility of the newly designed technological line. In the construction structure, a load-bearing element in the form of a lateral axis and articulated bogies mounted at its ends can be distinguished.

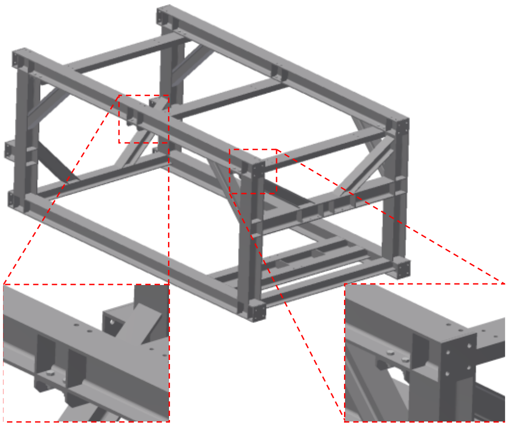

Fig. 1. - Charging hopper frame

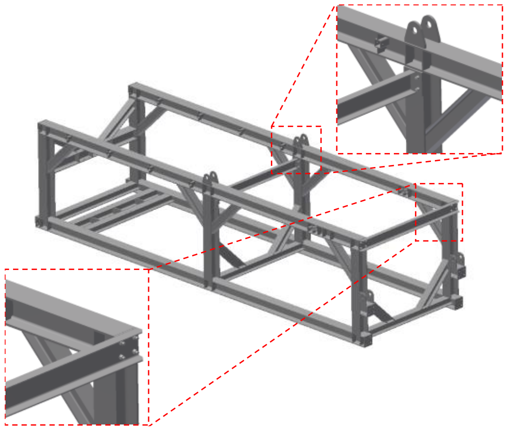

Fig. 2. - Vibrating screen frame

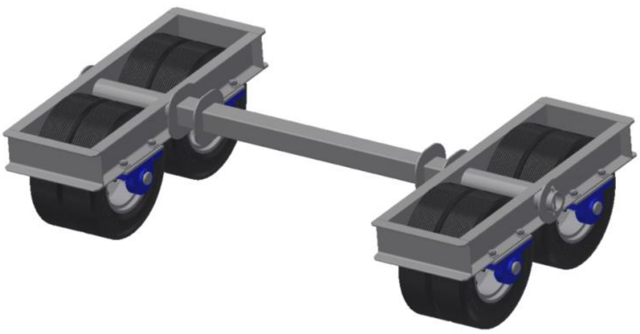

Fig. 3. - Driving unit model – top view

Only selected system components were analysed in the work. Commercial components and those which are not affected by high amplitude loads, i.e. crucial from the strength point of view, were omitted in the analysis.

For the main structural elements in the design, unalloyed structural steel, hot-rolled S355 J0, for which the yield stress is 355 MPa, was selected. It is killed steel of a ferritic-perlite structure in delivery condition, usually used in the construction of sensitive machine and equipment elements [11].

2. Strength analyses using the fem and the computational model construction

For the load-bearing frame, intermediate frames and all other non-integral elements, the standard rules for the conclusion of the material stress were applied, based on the hypothesis of the highest energy of effort state (Huber-Misses Hencky hypothesis) [13]. The following assumption was made (1):

$$\boldsymbol{k_{dop}} \leq \frac{Re}{x}, \tag{1}$$

where:
Re - material yield stress (355 MPa),
x - safety factor adopted arbitrarily.

On the basis of the experiments of the research team performing the calculations, the following safety factor values were adopted:
x_{native} = 1.2 - for a native material,
x_{joints} = 1.6 – for joints.
Hence:
$k_{dop\ native}$ = 295 MPa,
$k_{dop\ joints}$ = 221 MPa.

In order to construct the computational model, there were used techniques facilitating the imposition of the finite element mesh, while maintaining a high reflection of the geometric form of the analysed structure. The first step in the process was to simplify the virtual model.

In the context of load-bearing frames, the simplification consisted in replacing the volumetric model with the surface one, and as it was decided to use two-dimensional meshes, inclinations and slight rounding radii were removed. These elements in the virtual space have a certain height and width, while the thickness is stored in the computer memory as a single scalar size. Such an approach is appropriate for modelling fragments of slender, long, extensive structures whose thickness does not exceed 10% of their length or width [12]. Usually these are sheet metal elements as well as sections with open and closed cross-sections.

This process was carried out by the use of a function which automatically searches the central surface. This results in deactivating the view of elements containing finite volume and displaying only generated surfaces.

For the model prepared in this way it is possible to superimpose two-dimensional meshes which will help to perform calculations (Fig. 4 and 5). Additionally, it is possible to change quickly the thickness of T-profiles, structural channels, angles and sheet metal by changing one parameter, without the necessity to update the finite element meshes, which also increases the efficiency of the considerations.

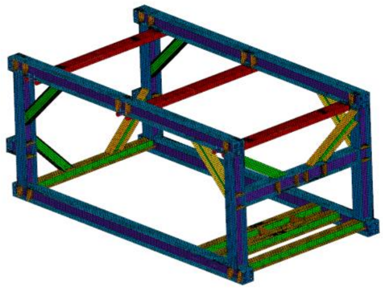

Fig. 4. - Mesh of two-dimensional elements of the charging hopper frame

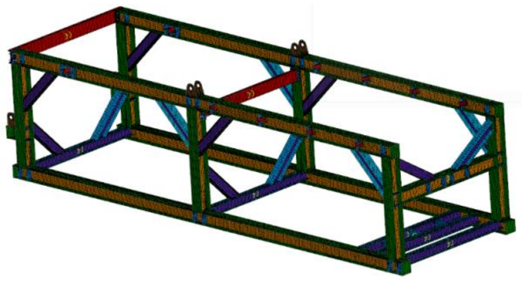

Fig. 5. - Mesh of two-dimensional elements of vibrating screen load-bearing frame

In the both analysed cases (Fig. 4 and 5), the second order (parabolic) mesh was used - it consists in the superimposition of additional calculation nodes between nodes located in the vertices of geometric figures, which increases the accuracy of calculations. The triangular mesh was used in places where the degree of geometric complexity of a structural element was large and the superimposition of the square mesh was impossible or significantly impeded by the impossibility of superimposing the square element without the introduction of the so-called "deformations", which consisted in the appearance of open angles between the sides of the quadrilateral with a value equal or exceeding 180 degrees. Then it is impossible to properly determine the stiffness matrix of the element.

During the development of the computational model, the geometry was simplified by removing minor rounding, undercutting and chamfering. However, holes were left which will then be used to model the bolted joints.

Superimposing three-dimensional meshes was performed using tools for automatic filling of selected volumes with finite elements. For the purpose of the discretisation, three-dimensional second-order pyramidal elements with additional nodes between the vertices and medium-density meshes were applied, whereas for the bearing frame a low-density mesh was used (Fig. 6).

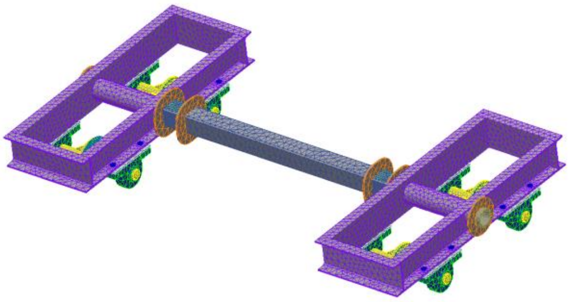

Fig. 6. - Mesh of two-dimensional elements of vibrating screen load-bearing frame

The analyses took into account the presence of bolts and their interactions with structural elements of the system. In case of the bolt-nut combination, the bolt head and nut were modelled using one-dimensional elements of RBE2 type. These elements are characterised by infinite stiffness, i.e. not susceptible to deformation. These elements were distributed using the so-called "spider" technique, i.e. a node, called the central node, was placed in the axis of the bolt, with which all nodes lying on the circles of holes through which the bolts are installed were connected via RBE2.

The core of the bolt itself was modelled from CBAR type elements, i.e. beam elements transferring tensile forces and bending moments. These elements were placed between the central nodes. This way of implementing bolted joints allows of reading the forces' values occurring in the joints during operation without going into details of stress patterns, displacements or deflections. At the same time, bolt stiffness (by using CBAR) is reflected in the correct way; hence the whole structure will be reliable.

The so-called "preload", i.e. the initial tension resulting from tightening the bolts to a given torque, is introduced in all bolt joints. The value of the preload was determined depending on the bolt size and strength class.

All significant force interactions, i.e. gravity and external input functions were taken into account to develop boundary conditions of the analyses (loads and supports).

For load-bearing frames, loads were applied over the entire length of the main beams. The load value is 100 kN, which corresponds to an application of 10 tons of mass. The degrees of freedom were reduced so that the possibility of longitudinal movement with all the nodes belonging to the lower beams was restrained, as shown in Figure 7.

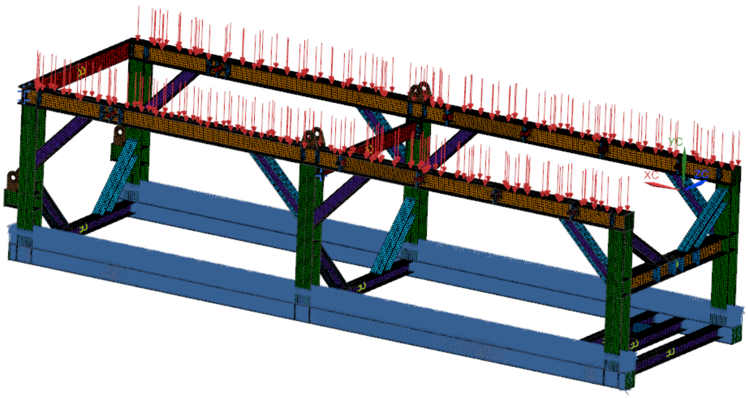

Fig. 7. - The method of modelling the boundary conditions of the analysis on the example of a vibrating screen frame. The red arrows illustrate the forces, whereas the blue arrows illustrate the reduced degrees of freedom

Figures 7 and 8 show the layout of boundary conditions for the analysed load cases. In such a state it was assumed that the main load of the tested structures is a vertical force Fy (10 t) generated by the mass of installed devices and gravitational acceleration g. The distribution of forces affecting the structural elements was carried out in accordance with the distribution resulting from the construction of the installed devices.

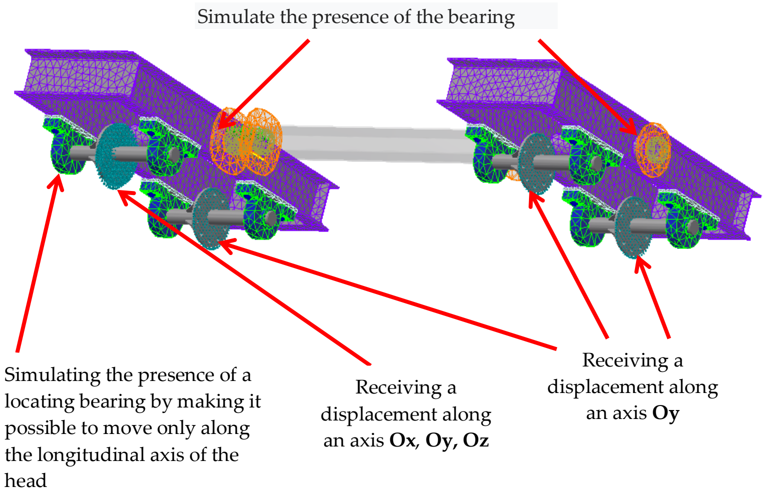

Fig. 8. - The reduced degrees of freedom for the computational model of a driving unit

Then, strength analyses were carried out for: the charging hopper frame, the vibrating screen frame and the driving unit.

For the frame of the charging hopper, the stress map H-M-H is shown in Fig. 9 because only these stresses are relevant for the accepted criteria, whereas Fig. 10 shows its displacements.

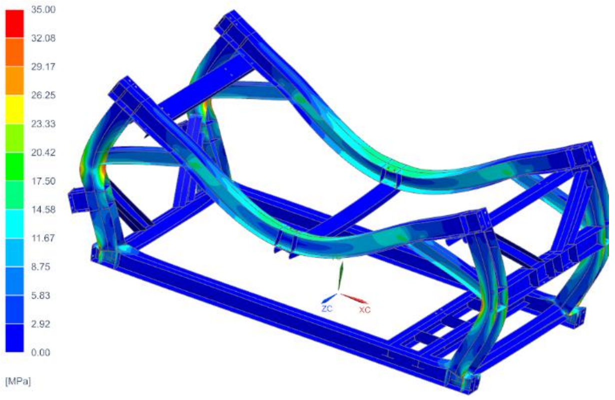

Fig. 9. - The stress map H-M-H, for the charging hopper frame (load 10t) – displacements in scale 200:1 – general view unit

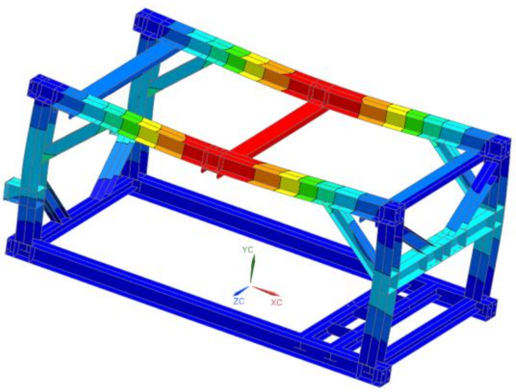

Fig. 10. - Displacement map, for the charging hopper frame (load 10t) – displacements in scale 100:1 – general view

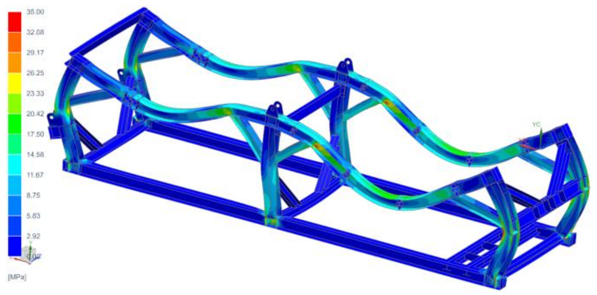

Fig. 11. - The stress map H-M-H, for the frame of the vibrating screen (load 10t) – displacements in scale 1000:1 – general view

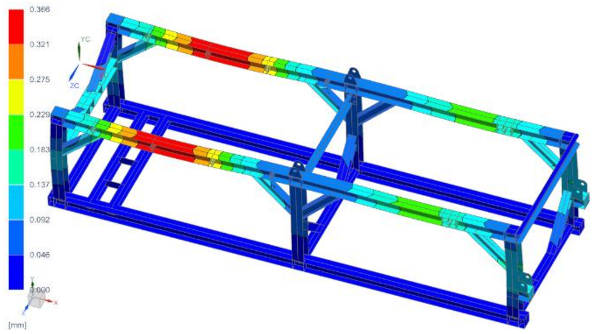

Fig. 12. - The displacement map for the Frome of the vibrating screen (load10t) – displacements in scale 100:1 – general view

The last stage was to present the stress map H-M-H for the frame of the driving unit (Fig. 13) and the map of its displacements (Fig. 14).

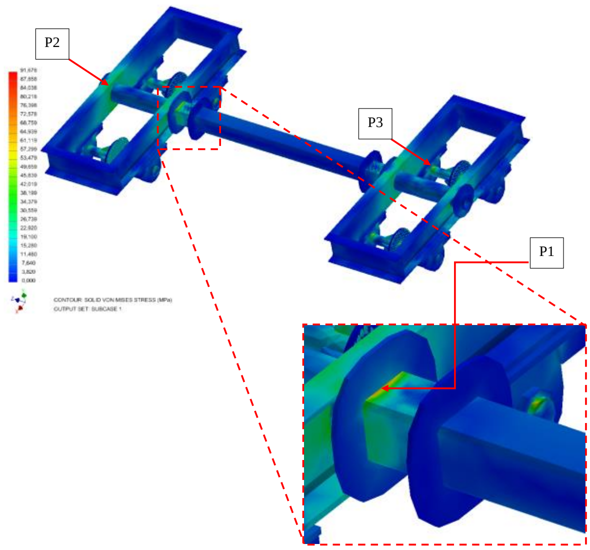

Fig. 13. - The stress map H-M-H, for the frame of the driving unit (load 10t) – top view

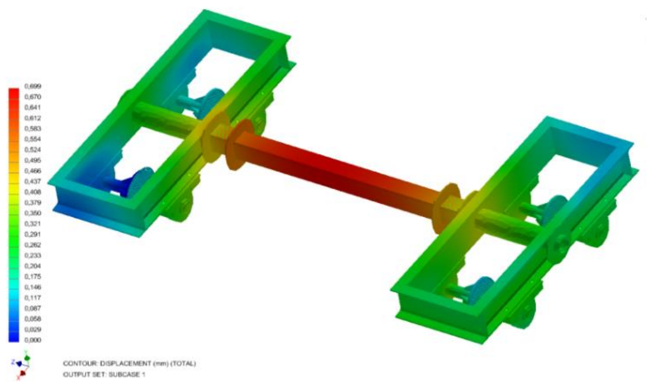

Fig. 14. - Displacements of mesh nods for the frame of the driving unit

3. Fatigue analysis

For the purpose of estimating the fatigue durability of the S355 steel structure, the Goodman-Smith diagram was utilized. Among the considered cases, the driving unit frame was taken into consideration. For the analyzed scenario, the stress amplitude was determined from the difference between the stress values obtained for the static loading case and the maximum operational loading case. For the construction of the computational model in the analyzed scenario, asymmetric loads were assumed in the form of unloading on one side. In this particular case, one side of the frame is completely unloaded (reaction forces equal zero), and the other side is maximally loaded.

Based on the analysis results for the examined points, average stress values were determined. In Fig. 13, the locations where maximum stress values were read for the mentioned two load cases are shown. The determined stress amplitudes and averages are plotted on the Goodman-Smith diagram for S355JO steel (Fig. 15).

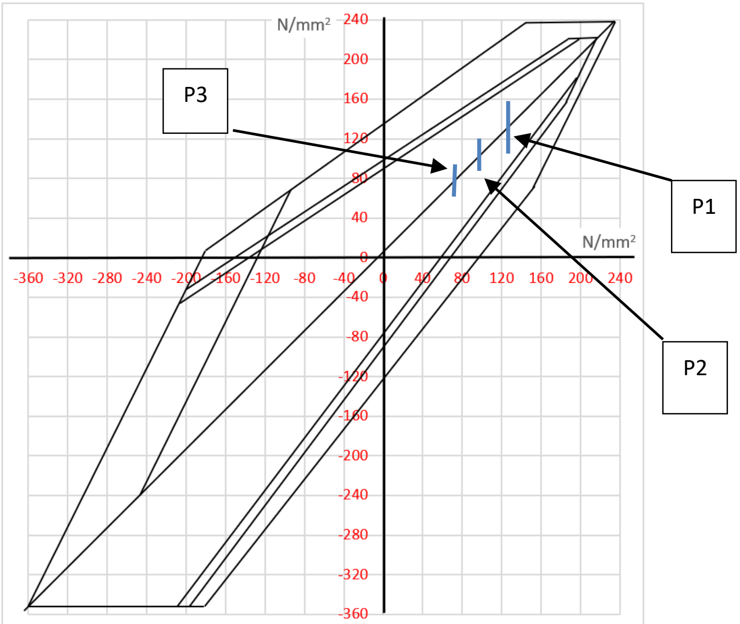

Fig. 15. - The Smith chart for S355JO steel, with selected mean and amplitude stresses plotted at measurement points for the frame of the driving unit

Conclusions

According to the above results, it is concluded that the device load-bearing structure meets the strength criteria [28]:

$k_{dop\ native}$ = 295 MPa,

$k_{dop\ joints}$ = 221 MPa .

The applied method is consistent with the method adopted by Truty et al. [26] in their work on the strength of the press adaptation table, Selech et al. [27] and Marcinkiewicz et al. [29, 30] in their work presenting a machine for laying drainage hoses.

In the analysed model, no points were observed where the stresses would exceed a value greater than 20% of the joint's permissible stresses. The analyzed structure is characterised by high stiffness and is not susceptible to deflections, which makes it possible to reduce its weight by implementing beams, sheet metal and profiles with smaller cross-sections and strength indicators. The material used is appropriate, and the von Misses stress values obtained during simulation tests are lower than the Re value. The risk of plasticization is very low. There is no possibility of replacing the material with another one with a lower yield strength. In order to verify the above calculations, it is necessary to make a prototype and perform tests with the use of strain gauges to validate computer calculations of the structure.

The forces in the bolts connecting the individual sections are low and reach a value of at most several percent of their load capacity. It has been observed that some of the bolts transmit compressive forces, which should be interpreted as the fact that they take over the compressive loads between the structural elements being in contact with each other.

The designed model is characterised by high load capacity, if the prototype and later serial production are made according to the above recommendations; the risk of malfunctioning due to improper stress is minimal.

In the context of fatigue analysis, it was not observed that in the three analyzed points (P1, P2 and P3), the lines representing the stress range went beyond the area of the permanent fatigue limit for the Goodman-Smith chart. This means that there is a possibility of long-term cyclic loading of the tested object without the risk of fatigue cracks.

In the context of fatigue analysis, it was not observed that in the three analyzed points (P1, P2 and P3) the lines representing the stress range went beyond the area of the permanent fatigue limit for the Goodman-Smith chart. This means that it is possible to load the tested object for a long time, cyclically, without the risk of fatigue cracks.

References

[1] Łodygowski T., Kąkol W.: Metoda elementów skończonych w wybranych zagadnieniach mechaniki konstrukcji inżynierskich. Wyd. PP, Poznań, 1994, 1-2.
[2] Zienkiewicz O. C.: Metoda elementów skończonych. Arkady, Warszawa, 1972, 63-84.
[3] Balonek K., Gozdur S.: Wprowadzenie do Metody Elementu Skończonego. Wydział Fizyki i Informatyki Stosowanej, AGH, Kraków, Poland [dostęp: 10 stycznia 2020]. Dostępny w internecie: http://fatcat.ftj.agh.edu.pl/~ i6balone/MES.Pdf.
[4] Fortuna Z., Macukow B., Wąsowski J.: Metody numeryczne. Wyd. Naukowo-Techniczne, Warszawa, 1993.
[5] Lohrengel A., Kramarczyk W., Kruk R., Twardoch K., Wieczorek A.: Modelowanie zjawisk dynamicznych w przekładniach zębatych, z wykorzystaniem metody elementów sztywnych. Górnictwo i geologia, 2011, 6(3), 115-126.
[6] Kruszewski J., Sawiak S., Wittbridt E.: Metoda sztywnych elementów skończonych w dynamice konstrukcji. Wyd. Naukowo-Techniczne, Warszawa, 1999.
[7] Gilewski W.: Some considerations on the finite element method. Sci. Rev. Eng. Eb=nv. Sci. 62, 2013, 502-510.
[8] Dobosz A, Panek H., Dobosz K.: Implementation of Finite Elements Method in Evaluatiom of Stresses in Dental Hard Tissues. Dent. Med. Probl., 2005, 42, 4, 651-655.
[9] Moss R., Basic M. : Pressure Vessel Design Manual. 4th Edition. Butterworth-Heinemann, 2012.
[10] Niemi E., Marquis G.: Introduction to the Structrual Stress Approach to Fatigue Analysis of Plate Structures, Lappeenranta University of Technology.
[11] Polska norma PN-EN 1561:2012 „Żeliwo szare".
[12] Tabor A., Zarębski K., Putyra P.: Wpływ temperatury na właściwości mechaniczne sferoidalnego żeliwa austenitycznego o zawartości niklu 20%. Archiwum Odlewnictwa, 2006, Rocznik 6, Nr 21(1/2).
[13] Niezgodziński M.E., Niezgodziński T.: Wzory wykresy i tablice wytrzymałościowe. WNT, Warszawa, 2004.
[14] Hou, S., Wei, J., Zhang, A., Zhang, C., Yan, J., Wang, C.: A Novel Comprehensive Method for Modeling and Analysis of Mesh Stiffness of Helical Gear. Applied Sciences, 2020, 10(19), 6695.
[15] Tan, X., Chen, W., Wang, L., Yang, J.: Analysis of Local Damages Effect on Mechanical Responses of Underwater Shield Tunnel via Field Testing and Numerical Simulation. Applied Sciences, 2020, 10(18), 6575.
[16] Hakula, H., Laaksonen, M. Frequency response analysis of perforated shells with uncertain materials and damage. Applied Sciences, 2019, 9(24), 5299.
[17] D'Amore, G. K. O., Mauro, F., Marinò, A., Caniato, M., Kašpar, J.: Towards the use of novel materials in shipbuilding: assessing thermal performances of fire-doors by self-consistent numerical modelling. Applied Sciences, 2020, 10(17), 5736.
[18] Invernizzi, S., Lacidogna, G., Carpinteri, A.: Numerical models for the assessment of historical masonry structures and materials, monitored by acoustic emission. Applied Sciences, 2016, 6(4), 102.
[19] Szcześniak, A., Stolarski, A.: Dynamic Relaxation Method for Load Capacity Analysis of Reinforced Concrete Elements. Applied Sciences, 2018, 8(3), 396.
[20] Li, J. B., Gao, X., Fu, X. A., Wu, C., Lin, G.: A nonlinear crack model for concrete structure based on an extended scaled boundary finite element method. Applied Sciences, 2018, 8(7), 1067.
[21] Azarinfar, H., Aghaebrahimi, M. R. Design, Analysis and Fabrication of a Novel Transverse Flux Permanent Magnet Machine with Disk Rotor. Applied Sciences, 2017, 7(8), 860.
[22] Ścieszka, S., Żołnierz, M.: Wpływ cech konstrukcyjnych hamulca tarczowego maszyny wyciągowej na jego niestabilność termosprężystą. Część I. Budowa modelu MES i jego weryfikacja. Zagadnienia Eksploatacji Maszyn, 2007, 42.3: 111-124.
[23] Różyło, P., Gajewski, J., Nowakowski, P., Machrowska, A.: Zastosowanie sieci RBF w analizie pękania elementów maszyn. Logistyka, 2015, (3), 4172-4186.
[24] Jachimowicz, J., Wawrzyniak, A.: Zastosowanie MES w zagadnieniach kontaktu elementów maszyn. Prace Instytutu Podstaw Budowy Maszyn/Politechnika Warszawska, 1999, 69-108.
[25] Chichociński, A., Ładecki, B.: Analiza przyczyn powstawania pęknięć zmęczeniowych w konstrukcji bębna pędnego maszyny wyciągowej. Mechanics/AGH University of Science and Technology, 2005, 24: 166-172.
[26] Truty, G., Nycz, D., Ślązkiewicz, M.: Numeryczne obliczenia wytrzymałościowe stołu adaptacyjnego do prasy. Modelowanie Inżynierskie, 2017, 33.
[27] Selech, J., Romek, D., Ulbrich, D., Włodarczyk, K., Staszak, Ż., Marcinkiewicz, J., Zbonik, M.: Projekt maszyny do bezwykopowego układania węży drenarskich. W: XXII Międzynarodowa Szkoła komputerowego wspomagania projektowania, wytwarzania i eksploatacji, Wyd. WAT, 2018, 334-340.
[28] Lachowicz, M. B., Lachowicz, M. M. Właściwości użytkowe, projektowe i technologiczne stali konstrukcyjnych klasyfikowanych według obowiązujących norm i stosowanych w budowie maszyn //Górnictwo Odkrywkowe, 2013, 54.

[29] Marcinkiewicz J., Bieńczak A., Dembicki D., Dudziński P., Mac J., Szczepaniak J. Strength analysis of insulated body with the use of FEM // Journal of Research and Applications in Agricultural Engineering, 60(1). 2015
[30] Marcinkiewicz J., Selech J., Staszak Ż., Gierz Ł., Ulbrich D., Romek D. DEM simulation research of selected sowing unit elements used in a mechanical seeding drill // MATEC Web of Conferences, Vol. 254, 2019, p. 02021
[31] Niesłony P., Grzesik W. Modelowanie procesu i operacji skrawania metodą elementów skończonych (MES) Cz. I. Podstawy i programy symulacyjne //Mechanik, 86(10), 2013, 825-826.
[32] Selech J., Ulbrich D., Włodarczyk K., Kowalczyk J., Adamkiewicz J. The prototype of stream amplifier used in transport of polydisperse medium //Procedia engineering, 2017, 192, P. 777–781.
[33] Kilikevičius, A., Bačinskas D., Selech J., Matijošius, J., Kilikevičien K., Vainorius D., Ulbrich D., Romek D. The influence of different loads on the footbridge dynamic parameters //Symmetry, 12 (4), 2020, 657.
[34] Pieniak D, Walczak A, Oszus M, Przystupa K, KamockaBronisz R, Piec R. Influence of thermal shocks on residual static strength, impact strength and elasticity of polymercomposite materials used in firefighting helmets //Materials, 2022,15(1), 57.
[35] Selech J., Ulbrich D., Kęska W., Staszak Ż., Marcinkiewicz J., Romek D., Rogoziński P., Design of a cultivator mounted on a tractor with a power of up to 20 kW //MATEC Web Conferences 254, 1-7, (2019).
[36] Durczak K., Selech J., Ekielski A., Żelaziński T., Waleński M., Witaszek K., Using the Kaplan–Meier Estimator to Assess the Reliability of Agricultural Machinery //Agronomy *12*, 2022, 1364.
[37] Domagała I., Gil L., Firlej M., Pieniak D., Selech J., Romek D., Biedziak B., Statistical Comparison of the Hardness and Scratch-Resistance of the PMMA Polymers Used in Orthodontic Appliances //Adv. Sci. Technol. Eng. Syst. J, 2020, 14, 250–261.
[38] Przystupa K., Chornodolskyy Y.M., Selech J., Karnaushenko V.O., Demkiv T.M., Kochan O., Syrotyuk S.V., Voloshinovskii A.S., The Influence of Halide Ion Substitution on Energy Structure and Luminescence Efficiency in CeBr2I and CeBrI2 Crystals //Materials, 2023, 16, 5085.
[39] Przystupa K., Beshley M., Hordiichuk-Bublivska O., Kyryk M., Beshley H., Pyrih J., Selech J., Distributed Singular Value Decomposition Method for Fast Data Processing in Recommendation Systems // Energies, 2021, 14, 2284.
[40] Kilikevičius A., Bačinskas D., Selech J., Matijošius J., Kilikevičienė K., Vainorius D., Ulbrich D., Romek D., The Influence of Different Loads on the Footbridge Dynamic Parameters // Symmetry, 2020, 12, 657.
[41] Paczkowska M., Selech J., Microstructure and Soil Wear Resistance of a Grey Cast Iron Alloy Reinforced with Ni and Cr Laser Coatings //Materials 2022, 15, 3153.
[42] Durczak K., Selech J., The Quantification of Operational Reliability of Agricultural Tractors with the Competing Risks Method, Tehnički vjesnik, vol. 29, no. 2, 2022, P. 628-633.
[43] Warguła Ł., Wojtkowiak D., Kukla M., & Talaśka, K. Symmetric nature of stress distribution in the elastic-plastic range of Pinus L. pine wood samples determined experimentally and using the finite element method (FEM). Symmetry 2020, 13(1), 39.
[44] Warguła Ł., Wojtkowiak, D., Kukla M., Talaśka K.. Modelling the process of splitting wood and chipless cutting Pinus sylvestris L. wood in terms of designing the geometry of the tools and the driving force of the machine // European Journal of Wood and Wood Products 2023, 81(1), 223-237
[45] Warguła Ł., Lijewski P., Kukla M. Effects of Changing Drive Control Method of Idling Wood Size Reduction Machines on Fuel Consumption and Exhaust Emissions // Croatian Journal of Forest Engineering: Journal for Theory and Application of Forestry Engineering 2023, 44(1), P. 137-151.
[46] Warguła Ł., Wilczyński D., Wieczorek B., Palander T., Gierz L., Nati C., Sydor M. Characterizing Sawdust Fractional Composition from Oak Parquet Woodworking for Briquette and Pellet Production. Advances in Science and Technology //Research Journal, 2023, 17(5).
[47] Kaczmarzyk, P., Małozięć, D., Burdzy, T., Ziegler, B., Krawiec, P., Dziechciarz, A., & Warguła, Ł. Analysis of the air stream flow parameters generated by the positive pressure ventilator - full scale experiment and CFD simulation //Scientific Reports 2024, 14(1), 6852.

Information of the authors

Marcinkiewicz Jacek, msc. eng., assistant, Poznan University of Technology
e-mail: jacek.marcinkiewicz@put.poznan.pl

Spadło Mikołaj, PhD Eng., assistant professor, Poznan University of Technology
e-mail: mikolaj.sspadlo@put.poznan.pl

Staszak Żaneta, PhD Eng., assistant professor, Poznan University of Technology
e-mail: staszak.zaneta@put.poznan.pl

DOI 10.52209/2706-977X_2024_2_53 IRSTI 55.20.23 UDC 621.431.73

Experimental study of the ultrasonic muffler efficiency for improving the exhaust gas cleaning system of internal combustion engines of automobiles

Pak I*.
Abylkas Saginov Karaganda Technical University, Karaganda, Kazakhstan
*corresponding author

Abstract. In this paper, an extensive study has been carried out on the use of ultrasound for the purpose of cleaning automotive exhaust gases. The main focus is on the use of ultrasonic emitter in automotive muffler design. The paper presents a detailed analysis of the theories associated with the ultrasonic coagulation process and an in-depth description of the physical aspects of the ultrasonic muffler. Methods for evaluating gas cleaning efficiency are also discussed and the importance of using energy consumption as a criterion for evaluating the efficiency of an ultrasonic silencer is emphasised. The paper presents a computational methodology for evaluating the efficiency of a new muffler design based on consideration of the power consumed by the engine to pass gases through the muffler. For experimental verification of the ultrasonic silencer efficiency, a special bench was created to measure the smokiness of gases at changing engine speeds. Experimental results confirmed the effectiveness of the ultrasonic silencer, showing a reduction in the smokiness of gases at a certain combination of speed and frequency of ultrasonic waves, which led to the best cleaning of exhaust gases.

Keywords: ultrasonic gas cleaning, car muffler design, muffler operation mode, exhaust gas cleaning system, internal combustion engine.

1. Introduction

In modern times, in an era of onrush of vehicle technologies, the problem of exhaust gas purification is making it as one of the most critical and important objectives facing mankind. Exhaust gas emissions containing harmful chemical compounds, hydrocarbons and heavy metals have increased with expansion of global traffic far more [1]. This problem has serious impacts on the environment, human health and climate change [2]. Studies show that these contaminants in the air are linked to a number of diseases and conditions, including respiratory diseases, allergies, lung cancer, cardiovascular disease and even neurological disorders. [3,4]

There are several methods of treating vehicle exhaust gases to reduce harmful emissions into the environment. These include catalytic converters (catalysts), exhaust gas recirculation (EGR) systems, diesel particulate filters (DPF), selective catalytic reduction (SCR), and particulate matter (PM) cleaning systems [5,6]. There are also industrial purification systems (absorption, sorption, oxidation, etc.), electric chambers and electric filters [7,8]. However, these cleaning methods have a shared disadvantage: they increase the energy and fuel costs of the engine, increase their operating costs and have a negative impact on the overall effectiveness of vehicles, causing reduced gas purification performance.

Moreover, not all the methods shown are capable to neutralize gases from their harmful fine particles. For example, catalysts, EGR and SCR are mainly focused on reducing nitrogen oxide (NOx) emissions [9,10]. As to gas purification systems each method specializes in cleaning a specific type of gas particles. For example, sorption is effective in capturing only aerosols and volatile organic compounds, oxidation methods - gaseous pollutants (hydrogen sulfide or nitrogen oxides), absorption - gases and their particles in liquids, and electrolysis is not used at all to capture fine particles in gases [11,12]. Therefore, the methods placed are potentially limited in the capture of all types of pollutants, including fine gas particles, requiring the search for new alternative purification methods.

This led to the idea of ultrasonic blast cleaning of vehicle exhaust. The advantage of ultrasound in exhaust gas purification is the ability to remove fine particles of gas, including soot, which contributes to an increased cleaning rate of up to 95%. Besides, the ultrasonic method does not require to use chemical reagents, thus avoiding to add second substances in the cleaning process [13,14]. Also unlike some traditional cleaning methods, this one does not require high energy costs. Design solutions are available for the installation of ultrasonic cameras between the engine collector and the muffler [15,16]. However, this approach can significantly complicate vehicle design and limit the possibilities of its modernization in the future.

So, we offer a more practical solution: installing an ultrasonic pulse in the body of the vehicle muffler. A muffler fitted with ultrasonic equipment (ultrasonic muffler) can reduce the toxicity of gas emissions without providing a significant pressure on the engine itself. This solution has a number of advantages, as the ultrasonic muffler does not take up a lot of power in the process, and its development and installation do not require significant financial costs. This approach combines efficiency with convenience and economy, making it a profitable option to increase the environmental compatibility of vehicles.

The hypothesis of the study was to confirm the potential ability to clean ultrasonic car exhaust emissions through the use of ultrasonic equipment in a muffler. The main objective of the study was to develop a methodology describing the efficiency of the ultrasonic muffler. This objective was achieved by solving several key problems: analysing existing theories related to acoustic coagulation; developing a research methodology that evaluates the efficiency of an ultrasonic silencer by measuring the engine power consumption of gas particles; developing a full-size ultrasonic muffler test rig to conduct the relevant experimental studies; conducting experiments to confirm the initial hypothesis and obtaining specific numerical values that confirm the products of the ultrasonic muffler.

The study acquires practical significance due to the possibility of applying the obtained functional relations and dependencies to the design and calculation of ultrasonic mufflers. This, in turn, can contribute to improving the efficiency of the process of purification of car exhaust gases.

2. Methods and Experiments

The ultrasound study showed its ability to intensify the process of “coagulation”, leading to the sticking or joining of gas particles during collisions with each other. Therefore, ultrasound can effectively increase the size and mass of the finest particles in the gaseous environment, making them more suitable for capture and disposal.

The fundamental approach to get the formation of coarse particles from fine ones is given by Smoluhovsky’s Theory. The basic principles of Smoluhovsky’s Theory of coagulation include the following:

1) Diffusion process: Smoluhovsky suggested that coagulation is a result of random collisions of particles. These impacts may result in larger aggregates if the collision energy exceeds the separation barrier energy;

2) Diffusion barrier: Particles can move as a result of thermal motion. However, for them to coagulate, it is necessary to overcome the diffusion barrier requiring auxiliary energy. This barrier becomes higher as the particle size decreases and the charge increases;

3) Electrostatic interactions: An important aspect of Smoluhovsky’s Theory is the cost of electrostatic interactions between particles. Particle charges can cause repulsion or attraction between them, which affects the probability and nature of coagulation;

4) Coagulation kinetics: Smoluhovsky’s Theory describes coagulation kinetics using an equation known as the Smoluhovsky equation:

$$-\frac{dn}{d\tau} = Kn^2, \tag{1}$$

where K – thermal coagulation constant, m/s. It characterizes the probability of particle convergence.

This equation entertains the possibility of molecular collision and the dependence of coagulation rate on particle concentration and temperature. A more complete picture of coagulation kinetics is provided by Smoluhovsky’s equation including the Einstein’s diffusion equation. Einstein’s equation describes the diffusion of particles in gas and can be integrated into Smolukhovsky’s equation to account for diffusion contributions to the coagulation process. So, Smoluhovsky’s modified equation with Einstein’s equation for diffusion will be as follows [17, 18]:

$$\frac{dn}{dt} = 2\pi DSn^2 \tag{2}$$

$$D = \frac{RT}{6\pi\eta rN} \tag{3}$$

$$\frac{dn}{dt} = \frac{1}{3}\frac{RTSn^2}{\eta rN} \tag{4}$$

However, insight of ultrasonic coagulation in the muffler is difficult and requires additional cost factors that are not included in the classical Smoluhovsky Theory. For example, hydrodynamic movement also arises in the muffler, apart from the Brownian particle movement, which can lead to turbulence in the gas flow. Moreover, the particle may fluctuate under radiation pressure under a calm environment [19,20].

However, there is a gas movement at a certain speed within the muffler changing the nature of these particle oscillations. Hence, to get such a complex process requires more in-depth research and even the development of individual models and experiments to further assess the gas purification and ultrasonic muffler effectiveness.

The evaluation of gas purification degree and the effectiveness of the vehicle ultrasonic muffler can be done using various methods and parameters. There are the following main ways to evaluate gas purification:

- Measurement of the content of gas emissions. The most direct way is to measure the concentration of the exhaust gas before and after exposure to ultrasound. This method involves the measurement of carbon dioxide (CO_2), oxygen (O_2) hydrocarbon (HC), carbon oxides (CO), fine particles and other pollutants. By comparing these values, it is possible to assess how effectively the ultrasonic muffler reduces emissions.

- Use of standards and regulations. Comparison of measurement results with environmental standards and regulations set by regulators to determine the conformity of exhaust gases with established norms. According to GOST *“P 51250-99. Internal combustion engines piston-type. Smoke of exhaust gases. Standards and test methods”* [20] where D gas opacity is the normative parameter for determining gas toxicity. This indicator not only evaluates the fume cleaning performance, but also fully reflects the performance of the muffler and the exhaust system. Providing the assessment of ultrasonic muffler operation and cleaning degree, it is necessary to take the ratio of gas smoke after and before the exposure to ultrasound D_2/D_1.

- Testing unit: Laboratory tests and tests on specially designed testing units can be performed to better evaluate gas purification. Under these conditions, you can control the parameters and repeat the experiments.

- Fuel consumption monitoring: Changes in fuel consumption may indicate the efficiency of the cleaning system. If the system does not operate optimally, it may affect fuel consumption.

- Exhaust temperature measurement: Increased exhaust temperature may indicate cleaning problems as some systems may require certain temperatures for efficient operation.

However, the methods placed are not able to fully assess the performance of the ultrasonic muffler, as they do not include the efficiency of energy consumption, as in do not describe how much energy the muffler consumes to operate in optimal modes and to ensure the necessary level of reduction of harmful particles in the environment. Thus, the efficiency of the ultrasonic muffler is offered to be evaluated by the gas tolerance. Gas flow estimation in the exhaust system of vehicle based on the gas capacity is an important aspect of engineering calculations and optimization. Key aspects to estimate the effectiveness of the ultrasonic muffler of gas power costs are as follows:

- system efficiency. Estimation of the gas power consumption allows to determine the efficiency of the exhaust system. The lower the power required to move gases through the system, the more efficient the system is;

- resistance minimization: The power cost estimate allows to identify possible resistance to gas movement in the exhaust system. Minimizing this resistance can reduce engine load and improve operation efficiency;

- reducing toxic emissions: Reducing the gas capacity can also help reduce emissions to the atmosphere. Less efficient systems can cause increased pollutant emissions, which negatively affects the environment;

- design and upgrade: The estimation of gas capacity is important when designing new exhaust systems or upgrading existing ones. This helps engineers to choose optimal components and configurations for maximum efficiency;

- economic efficiency: Gas capacity cost analysis also has an economic aspect. Lower costs can reduce operating costs and improve the competitiveness of vehicles or production processes.

In general, the estimation of gas flow based on power input plays an important role in engineering calculations and optimization of exhaust systems. This helps not only to reduce the negative impact on the environment, but also to improve the optimum and efficient operation of vehicles.

In order to estimate the power input for the movement of gas particles inside the muffler, the following calculation method was developed, which considers the equation of gas energy change in the purification system. Gas energy change equation ΔE is shown as a change in the kinetic energy of the gas on exit from the engine collector and at the input to the muffler (without the influence of ultrasound), as well as the operation performed by external forces (under the condition of ultrasonic action) from the ultrasonic emitter:

Without ultrasound:

$$\Delta E = E_{\text{exit}}^{\text{collector}} - E_{\text{input}}^{\text{muffler}}, \tag{5}$$

With exposure to ultrasound:

$$\Delta E = E_{\text{exit}}^{\text{collector}} - E_{\text{input}}^{\text{ultrasonic muffler}} + A_{\text{ultrasound}}. \tag{6}$$

where $E_{\text{exit}}^{\text{collector}}$ – exhaust gas energy from engine collector, J;

$E_{\text{input}}^{\text{muffler}}$ – input gas energy in engine muffler, J;

$E_{\text{input}}^{\text{ultrasound muffler}}$– input gas energy in ultrasonic engine muffler, J;

$A_{\text{ultrasound}}$ – operation performed by ultrasonic gas, J.

Then equation (5) was converted as follows:

Without ultrasound:

$$\Delta E = \frac{m\vartheta_{\text{exit}}^2}{2} - \frac{m\vartheta_{\text{input}}^2}{2}, \tag{7}$$

With exposure to ultrasound:

$$\Delta E = \frac{m\vartheta_{\text{exit}}^2}{2} - \frac{m\vartheta_{\text{ultrasound input}}^2}{2} + \mathrm{A}_{\text{ultrasound}}, \tag{8}$$

where m – gas mass, kg;

ϑ_{exit} – engine collector exhaust gas speed, m/s;

ϑ_{input} – speed of input gas to engine muffler, m/s;

$\vartheta_{\text{ultrasound input}}$ – speed of input gas to engine ultrasonic muffler, m/s.

The operation performed by the ultrasonic action on gas in turn has been converted as kinetic energy of the gas particles oscillating from the ultrasound side:

$$A_{\text{ultrasound}} = \frac{mU_{\text{ultrasound}}^2}{2}, \tag{9}$$

where $U_{\text{ultrasound}}$ – ultrasonic oscillation speed of gas particles.

Hence the following equation for changing the energy of gas ΔE was obtained under the condition of ultrasound:

$$\Delta E = \frac{m\vartheta_{\text{exit}}^2}{2} - \frac{m\vartheta_{\text{input}}^2}{2} + \frac{mU_{\text{ultrasound}}^2}{2} \tag{10}$$

By dividing equation (4) for the operation time t, the equation for the change of power consumption for the movement of gas particles ΔN was obtained:

Without ultrasound:

$$\frac{\Delta E}{t} = \frac{m\vartheta_{\text{exit}}^2}{2t} - \frac{m\vartheta_{\text{input}}^2}{2t}, \tag{11}$$

$$\Delta N = N_{\text{collector}} - N_{\text{muffler}}. \tag{12}$$

With exposure to ultrasound:

$$\frac{\Delta E}{t} = \frac{m\vartheta_{\text{exit}}^2}{2t} - \frac{m\vartheta_{\text{input}}^2}{2t} + \frac{mU_{\text{ultrasound}}^2}{2t}. \tag{13}$$

$$\Delta N = N_{\text{collector}} - N_{\text{muffler}} + N_{\text{ultrasound}}. \tag{14}$$

The resulting equation (12) was then converted as follows:

$$N_{\text{collector}} = P_{\text{collector}} S_{\text{collector}} \vartheta_{\text{exit}} \tag{15}$$

$$N_{\text{muffler}} = P_{\text{muffler}} S_{\text{muffler}} \vartheta_{\text{input}} \tag{16}$$

$$N_{\text{ultrasonic muffler}} = P_{\text{ultrasonic muffler}} S_{\text{ultrasonic muffler}} \vartheta_{\text{ultrasonic input}} \tag{17}$$

Without ultrasound:

$$\Delta N = P_{\text{collector}} S_{\text{collector}} \vartheta_{\text{exit}} - P_{\text{muffler}} S_{\text{muffler}} \vartheta_{\text{ input}} \tag{18}$$

With exposure to ultrasound:

$$\Delta N = P_{\text{collector}} S_{\text{collector}} \vartheta_{\text{exit}} - P_{\text{ultrasound muffler}} S_{\text{ultrasonic muffler}} \vartheta_{\text{ultrasonic input}} + N_{\text{ultrasound}}. \tag{19}$$

where $P_{\text{collector}}$ – Engine exhaust collector pressure, Pa;

P_{muffler}– Engine pressure in muffler, Pa;

$P_{\text{ultrasound muffler}}$– Pressure in ultrasonic engine muffler, Pa.

Exhaust gas losses at collector exit (ϑ_{exit}) and at muffler input (ϑ_{input}) were calculated using the mass retention equation for gas flow and the Bernoulli equation.

Mass conservation equation for gas flow:

For the collector:

$$S_{\text{exit}} \rho_{\text{exit}} \vartheta_{\text{exit}} = S_{\text{collector}} \rho_{\text{collector}} \vartheta_{\text{collector}}, \tag{20}$$

where S_{exit} – gas flow exit area from the collector, m^2;

ρ_{exit} – reservoir exit gas density, kg/m^3;

$S_{\text{collector}}$ – collector flow area, m^2;

$\rho_{\text{collector}}$ – gas density in collector, kg/m^3;

$\vartheta_{\text{collector}}$ – gas velocity in collector, m/s.

For no impact and ultrasonic muffler:

$$S_{\text{input}}\rho_{\text{input}}\vartheta_{\text{input}} = S_{\text{muffler}}\rho_{\text{muffler}}\vartheta_{\text{muffler}}, \tag{21}$$

$$S_{\text{input}}\rho_{\text{input}}\vartheta_{\text{input}} = S_{\text{ultrasonic muffler}}\rho_{\text{ultrasonic muffler}}\vartheta_{\text{ultrasonic muffler}}. \tag{22}$$

where S_{input} – gas input flow area in the muffler, m^2;
ρ_{input} – input gas density to the muffler, kg/m^3;
S_{muffler} – muffler flow area, m^2;
ρ_{muffler} – gas density in muffler, kg/m^3;
$\vartheta_{\text{muffler}}$ – gas velocity in muffler, m/s.

Bernoulli equation (with minor changes in height and possible pressure):

For the collector:

$$\frac{1}{2}\rho_{\text{exit}}\vartheta^2_{\text{exit}} = \frac{1}{2}\rho_{\text{collector}}\vartheta^2_{\text{collector}}, \tag{23}$$

For no impact and ultrasonic muffler:

$$\frac{1}{2}\rho_{\text{input}}\vartheta^2_{\text{input}} = \frac{1}{2}\rho_{\text{muffler}}\vartheta^2_{\text{muffler}}, \tag{24}$$

$$\frac{1}{2}\rho_{\text{input}}\vartheta^2_{\text{input}} = \frac{1}{2}\rho_{\text{ultrasonic muffler}}\vartheta^2_{\text{ultrasonic muffler}}. \tag{25}$$

Given the collector/muffler areas and their sections $S = const$ and that the gas is not compressed or expanded substantially $\rho = const$ remain, so the equation of mass conservation for the gas flow and the Bernoulli equation follows:

For the collector:

$$\vartheta_{\text{exit}} = \vartheta_{\text{collector}}, \tag{26}$$

For no impact and ultrasonic muffler:

$$\vartheta_{\text{input}} = \vartheta_{\text{muffler}}, \tag{27}$$

$$\vartheta_{\text{input}} = \vartheta_{\text{ultrasonic muffler}}. \tag{28}$$

This means that the exhaust gas velocity at the collector exit is equal to the gas velocity in the collector and the exhaust gas velocity at the exhaust input to the muffler is equal to the gas velocity in the muffler. Therefore, equation (7) has been converted as follows:

Without ultrasound:

$$\Delta N = P_{\text{collector}}S_{\text{collector}}\vartheta_{\text{collector}} - P_{\text{muffler}}S_{\text{muffler}}\vartheta_{\text{ muffler}} \tag{29}$$

With exposure to ultrasound:

$$\begin{gathered}\Delta N = P_{\text{collector}}S_{\text{collector}}\vartheta_{\text{collector}} \\ -P_{\text{ultrasonic muffler}}S_{\text{ultrasonic muffler}}\vartheta_{\text{ultrasonic muffler}} + N_{\text{ultrasound}}.\end{gathered} \tag{30}$$

Collector and muffler pressure is defined as follows:

$$P_{\text{collector}} = P_{atmosphere} + \frac{1}{2}\rho\vartheta^2_{\text{collector}}, \tag{31}$$

Without ultrasound:

$$P_{\text{muffler}} = P_{\text{collector}} + \frac{1}{2}\rho\vartheta^2_{\text{collector}} - \frac{1}{2}\rho\vartheta^2_{\text{muffler}} \tag{32}$$

With exposure to ultrasound:

$$P_{\text{ultrasonic muffler}} = P_{\text{collector}} + \frac{1}{2}\rho\vartheta^2_{\text{collector}} - \frac{1}{2}\rho\vartheta^2_{\text{ultrasonic muffler}}, \tag{33}$$

The gas velocity in collector, in muffler and in the ultrasonic muffler is determined as follows:

$$v_{\text{collector}} = \frac{Q\omega}{\pi r^2_{\text{collector}}}, \tag{34}$$

$$v_{\text{muffler}} = \frac{Q\omega}{\pi r^2_{\text{muffler}}} \tag{35}$$

$$v_{\text{ultrasonic muffler}} = \frac{Q\omega}{\pi r^2_{\text{ultrasonic muffler}}{}^2} \tag{36}$$

where Q – engine volume, m^3;

ω – engine rotational speed, rad/s;

r – radius of exhaust collector and mufflers.

Then experimental studies should be carried out to assess the degree of gas purification and the efficiency of the ultrasonic vehicle muffler. An experimental Ultrasonic Muffler Stand developed in the scientific laboratory of the Transport Engineering and Logistic Systems Department was used for experimental studies (Figure 1).

Fig. 1. – A full-sized Ultrasonic Vehicle Muffler Stand

A full-sized Ultrasonic Vehicle Muffler Stand (Figure 2) includes a 110 mm metal pipe and ultrasonic equipment. The experimental Ultrasonic Muffler Stand consists of the following structural components: 1 – Input pipe; 2 – Ultrasonic muffler body; 3 – ultrasonic emitter which propagates the ultrasonic wave through the inner casing of the muffler; 5 – Exit pipe.

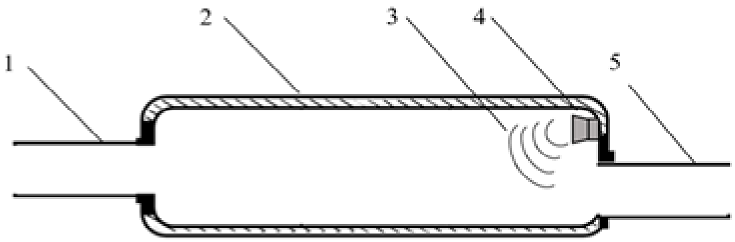

Fig. 2. – Schematic diagram of a full-sized Ultrasonic Vehicle Muffler Stand

Ultrasonic equipment consists of an ultrasonic generator and ultrasonic emitter (Figure 3). The power of ultrasonic equipment is 100 W.

Fig. 3. – Ultrasonic generator with ultrasonic wave emitters

To analyze the qualitative and quantitative composition of emissions from the exhaust system, the vehicle-type 4-component gas analyzer "Infracar M-1.01" was used.

The pilot studies were conducted in two phases. The first phase was to determine gas composition and the second one was to measure the opacity of the gases, including the effects and without ultrasound.

The pilot studies were as follows. The experimental tests were carried out in two modes: with and without ultrasonic equipment, where the ultrasonic exposure time was one minute, and the frequency of ultrasound exposure was 40 kHz.

These studies were performed on the laboratory diesel engine "D245" with a volume of 4750 cm^3 and a capacity of 245 horsepower. Engine ran at different crankshaft speeds: 1000, 1200 and 1400 rpm.

The exhaust gas from the vehicle was fed into the full-sized Ultrasonic Muffler Stand via an input pipe. Inside the stand, ultrasonic waves in the longitudinal direction were applied at 40 kHz ultrasonic frequency. The effects of ultrasound on gas flow have improved coagulation and cleaning by increasing particle size and soot deposition. The cleaned exhaust gas is then discharged through the exit pipe of the full-sized Ultrasonic Muffler Stand.

3. Results and discussion

The results of the pilot studies are shown in Table 1.

Table 1. Results of the pilot studies

Engine crankshaft speed (rev/min)	1000 rev/min		1200 rev/min		1400 rev/min	
	Without ultrasound	Ultrasonically *f*= 40 kHz	Without ultrasound	Ultrasonically *f*= 40 kHz	Without ultrasound	Ultrasonically *f*= 40 kHz
CH, ppm	0,00	0,00	0,00	0,00	0,02	0,02
CO, %	0,02	0,01	0,02	0,02	0,01	0,01
CO_2, %	1,38	1,36	1,39	1,36	1,40	1,39
O_2, %	18,66	18,7	18,97	18,98	18,56	18,56

Based on the results of the experiments, including the analysis of the emission composition, diagrams have been constructed (Figures 4 and 5) illustrating how oxygen (O_2) and carbon dioxide (CO_2) are changing depending on engine crankshaft speed, with or without the use of ultrasound with a constant impact frequency of 40 kHz.

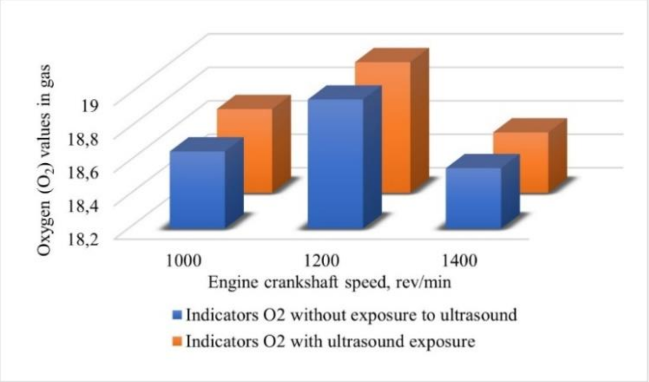

Fig. 4. – Changes in oxygen values (O_2) without exposure and with ultrasound

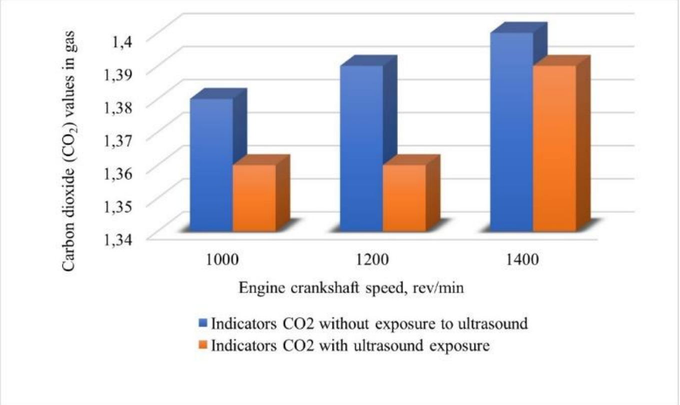

Fig.5. – Carbon dioxide CO_2 change without exposure and with ultrasound

The diagrams in Figures 4 and 5 confirm that ultrasound is indeed effective in influencing the composition and purification of emissions. Based on results obtained, it was found that when the engine crankshaft speed increases and under ultrasound, the percentage oxygen content increases and the carbon dioxide concentration in the exhaust gas decreases.

Then a diagram (Figure 6) was constructed based on results of the fumes experiments, showing how the smoke levels of the gases change depending on the presence or absence of ultrasound at a constant exposure frequency of 40 kHz.

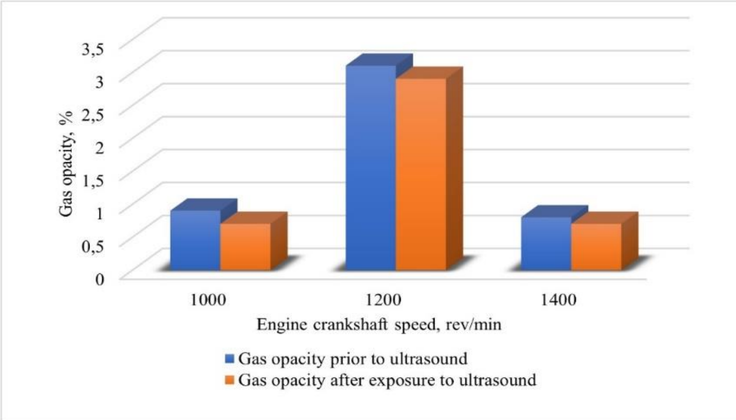

Fig.6. – Changes in gas opacity without exposure and with ultrasound

Studies have shown that the use of ultrasound has a positive effect on reducing smoke levels. This is confirmed by the fact that the numerical opacity of the gases after the application of ultrasound was lower than that of the non-ultrasonic gases. The use of ultrasound resulted in a reduction in smoke levels from 6 to 22 per cent.

It was also noted from the pilot studies that ultrasonic exposure does not cause significant changes in temperature and fuel consumption. This indicates that the ultrasonic equipment does not adversely affect the efficiency of the cleaning system and does not cause any deviation.

Using data on the smoke level of the gases, the ratio between the opacity of the ultrasonic gas exposed to ultrasound and not exposed to such exposure was calculated. This ratio is an important indicator of the ultrasonic muffler effectiveness, reflecting the degree of gas purification depending on the engine crankshaft rotation speed. The results of the D_2/D_1 calculations are shown in Table 2.

Table 2. D_2/D_1 ratio calculation results

Engine crankshaft speed (rev/min)	Engine crankshaft angular speed (rad/s)	Gas smoke ratio (D_2/D_1)
1000	104,7	0,77
1200	125,6	0,93
1400	146,6	0,875

Based on the calculations obtained, a diagram has been drawn up showing the relationship between the gas smoke ratio (D_2/D_1) and the engine crankshaft rotation rate (Figure 7).

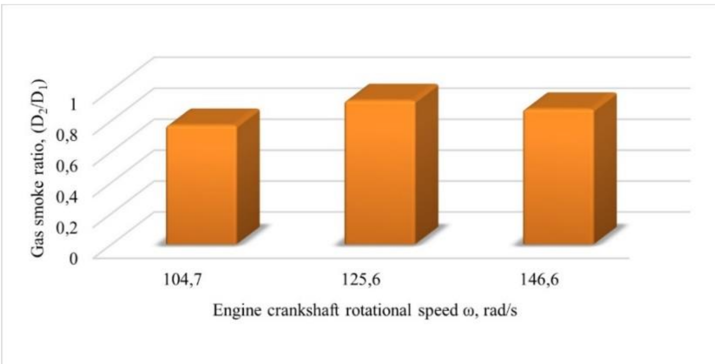

Fig.7. – Change in the ratio of gas smoke to engine crankshaft angular speed

The diagram in Figure 7 shows that when the engine crankshaft speed is increased, the gas smoke ratio is increased, for example at the angular speed of 125.6 rad/s the ratio (D_2/D_1) has reached the maximum (0.93). This is because the increased angular velocity increases the velocity of the gas flow entering the inside of the muffler and, the coagulation process does not be in seconds at a faster gas flow. It takes time for the finest particles to come together and start settling. During this period, particles of different sizes should come into contact with each other and create major agglomerates. Therefore, it is possible to increase the gas opacity ratio with a sharp increase in angular velocity values, as the intensity of the coagulation process has not reached the required level. However, there is a decrease in the opacity (0.875) with a further increase in the angular velocity (146 rad/s), which indicates that the coagulation process has entered an intensive phase and the gas particles have gradually started to coagulate and settle, thereby increasing the transparency of the gas and reducing its smoke level. Thus, the coagulation process intensifies the gas purification efficiency and reduces the number of partially burned particles when exposed to the gas by ultrasound.

The efficiency of the ultrasonic muffler was then estimated by the power input per gas movement through the exhaust system. Typically, the exhaust system, as in, to conduct the exhaust gas through the system and to remove it to the atmophere is spent in the order of 1-5% of the power of the entire engine of the vehicle. It is supposed that the power consumption for gas movement will decrease using the ultrasonic muffler. This is because, compared to the current mufflers, the ultrasonic muffler has a simple design that does not allow for the free passage of gases and provides no resistance, thus keeping the engine power input. Moreover, ultrasonic equipment does not consume much power and does not impose other load on the engine. So, to confirm these assumptions, a calculation of the gas flow capacity cost was made through the muffler, including the impact and without the impact of ultrasound, according to the earlier calculation method provided.

Calculation of the capacity cost for gas movement in a muffler with and without the exposure to ultrasound:

Without ultrasound:

Collector gas velocity:

$$v_{\text{collector}} = \frac{0{,}00475 \cdot 104{,}7}{0{,}0052} = 95{,}63$$

Collector pressure:

The average atmospheric pressure is about $P_{atmosphere}$ = 101.3 kPa

The average exhaust gas density is ρ=0,8-1,4 kg/m³ for more accurate calculations is assumed ρ=1,225 kg/m³.

$$\mathrm{P}_{\text{collector}} = 101{,}3 \cdot 10^3 + 5601{,}37 = 106901{,}37$$

Gas velocity in muffler:

$$v_{\text{muffler}} = \frac{0{,}00475 \cdot 104{,}7}{0{,}002826} = 175{,}98$$

Muffler pressure:

$$\mathrm{P}_{\text{muffler}} = 106901{,}37 + 5601{,}37 - 18968{,}48 = 93534{,}26$$

Gas flow capacity costs:

$$\Delta N = 53159{,}48 - 46516{,}40 = 6643{,}085$$

With exposure to ultrasound:

Ultrasonic muffler area S_{muffler}:

$$S_{\text{ultrasonic muffler}} = 3{,}14 \cdot 0{,}055 = 0{,}0094985$$

Gas velocity in ultrasonic muffler:

$$v_{\text{ultrasonic muffler}} = \frac{0{,}00475 \cdot 104{,}7}{0{,}0094985} = 52{,}35$$

Pressure in ultrasonic muffler:

$$P_{\text{ultrasonic muffler}} = 106901{,}37 + 5601{,}37 - 1678{,}57 = 110824{,}17$$

Gas flow capacity costs:

$$\Delta N = 53159{,}48 - 50490{,}07 + 50 = 2719{,}4$$

Total engine power:

$\mathrm{N_d} = 180197$ W

Percentage of muffler power consumption of total engine power:

Without ultrasound:

$$180197 - 100\%$$
$$6643{,}085 - x$$

$$x = \frac{6643{,}085 \cdot 100\%}{180197} = 3{,}68\%$$

Ultrasonically:

$$180197 - 100\%$$
$$2719{,}4 - x$$

$$x = \frac{2719{,}4 \cdot 100\%}{180197} = 1{,}5\%$$

Reduction of the power cost for gas movement if using the ultrasonic muffler:

$$3{,}68\% - 1{,}5 = 2{,}18\%$$

As it was noted earlier, engine power costs per exhaust system are about 1-5%. Therefore, if an ultrasonic muffler is used, the power consumption of the exhaust system will be reduced by 2.18%.

In this way, it is possible to achieve positive changes in gas composition, to get reduced gas opacity and to reduce power costs using an ultrasonic muffler that may be important for compliance with environmental standards, increase efficiency and reduce harmful gas emissions in the vehicle exhaust system.

Conclusion

The study described in the article represents a new method of exhaust gas purification of internal combustion engines from harmful particles by using ultrasonic emitters in vehicle mufflers. The authors emphasize that the use of ultrasound for exhaust gas purification is proved by its low energy consumption and rather low development and installation costs. This approach combines efficiency, accessibility and economic viability, making it the palatable option for improving the environmental sustainability of vehicles.

The article describes various ways to assess muffler effectiveness equipped with an ultrasonic emitter, including analysis of the emission composition, measurement of gas opacity, conducting testing units and monitoring the parameters of the temperature and fuel consumption. Also to assess the economic feasibility to use such a muffler, it is offered to assess using indicators of power costs for the gas flow through the exhaust system.

The article also describes a full-sized Ultrasonic Muffler Stand where pilot studies were conducted to determine the gas composition, gas opacity and temperature and fuel consumption fixation, including the effects and non-effects of ultrasound on gas.

The results of the experiments on the full-sized stand showed that the introduction of ultrasonic emitters reduces gas opacity, increases the oxygen content and reduces the level of carbon dioxide in emissions, and the change in temperature and fuel consumption were almost negligible, confirming the optimum operation of the ultrasonic muffler. Overall cleaning efficiency reached 6 to 22 per cent depending on the experimental conditions, as in, engine speed change.

Also, there is a change in the ratio of gas opacity when increasing the engine crankshaft angular speed. For example, a decrease in the gas opacity ratio was achieved and the overall cleaning rate was rather 12-23% at the maximum engine crankshaft angular velocity values selected in the pilot studies. As to the developed methodology for calculating the gas power consumption, it was determined that if we use an ultrasonic muffler, the engine power input for the exhaust system will be reduced by 2.8%. The obtained results prove that ultrasound has the potential as an effective method of exhaust gas purification and underlines the importance of realising further study in this area.

Studies obtained in the article makes an important contribution to the development of innovative methods of exhaust gas purification contributing to more efficient and eco-friendly vehicle operation.

References

[1] Sagna K, Amou1 K.A., Boroze T.E., Kassegne D., Almeida A., Napo. K. Environmental Pollution due to the Operation of Gasoline Engines: Exhaust Gas Law // International Journal of Oil, Gas and Coal Engineering, Vol. 5, Issue 4, 2017. – p. 39-43.

[2] Mussazhanova Zh., Kadyrova I, Yessenbayeva A., Apsalikov B., Massabayeva M., Kazymov M., Shakhanova A., Aukenov N., Shaimardanov N. Biomarkers of immunothrombosis and polymorphisms of IL2, IL6, and IL10 genes as predictors of the severity of COVID-19 in a Kazakh population. // PLoS ONE, Vol. 18, Issue 6, 2023. – p. 61-67.

[3] Kolesnichenko S., Kolesnikova Ye., Kadyrova I., Korshukov I., Barkhanskaya V., Sultanbekova A., Babenko D. SARS-COV-2 detection in MALDI-TOF mass spectra by machine learning // AIP Conf. Proc., Vol. 2872, Issue 1, 2023. – p. 1-13.

[4] Akhmaltdinova L., Korshukov I., Kolesnikova Ye., Kolesnichenko S., Babenko D., Kadyrova I., Kabildina N., Sirota V., Zhumaliyeva V., Taizhanova D., Vazenmiller D., Turmukhambetova A. Association of four genetic variants with colorectal cancer in Kazakhstan population // Oncotarget, Vol.12, Issue 21, 2021. – p. 2215-2222

efficiency of catalytic converter. // International Journal of Ambient Energy, Vol.37, Issue 5, 2015. – p. 507-512
[6] Kadyrov A., Zhunusbekova Z., Ganyukov A., Kadyrova I., Kukesheva A. General characteristics for loading the working elements of drilling and milling machines when moving in the clay solution // Communications - Scientific Letters of the University of Zilina, Vol. 23, Issue 2, 2021. – p. 97-105, doi: https://doi.org/10.26552/com.C.2021.2.B97-B105
[7] Kadyrov A., Kurmasheva B,. Kabikenov S., Kukesheva A., Kryuchkov Ye., Pak I. Development of Calculation Methodology for Optimizing the Operating Mode of an Electric Pulse Unit for Cleaning Exhaust Gases // Communications - Scientific Letters of the University of Zilina, Vol. 26, Issue 1, 2024. – p. 41-53
[8] Kadyrov, A., Sakhapov, R., Kukesheva, A. Kryuchkov, Y, Sinelnikov, K, Ganyukov, A. Studying the process of the internal combustion engine exhaust gas purification by an electric pulse. // Communications - Scientific Letters of the University of Zilina, Vol. 24, Issue 4, 2022. – p. 275-287
[9] Hocking M. B. B. Handbook of chemical technology and pollution control. University of Victoria: Elsevier, 2013. – 778 p.
[10] Kadyrov A., Sarsembekov B., Ganyukov A., Zhunusbekova Z., Alikarimov K. Experimental research of the coagulation process of exhaust gases under the influence of ultrasound. // Communications - Scientific Letters of the University of Zilina, Vol. 23, Issue 4, 2021. – p. 288-298
[11] Kukesheva A., Kadyrov A., Kryuchkov Y. Establishing the parameters of the operation mode of the electric pulse automobile muffler // Journal of Applied Engineering Science. Vol. 22, Issue 1, 2024. – p.89–99. doi: 10.5937/jaes0-45196
[12] Kyzylbaeva E.Zh., Kukesheva A.B., Kunaev V.A. Mathematical model of plate movement in thixotropic mud. // Material and Mechanical Engineering Technology, Vol. 2, Issue 2, 2020. – p. 26-30.
[13] Kadyrov A., Sakhapov R., Ganyukov A., Sinelnikov K., Kurmasheva B., Suyunbaev Sh. Studying the process of transport equipment cooling system ultrasonic cleaning // Communications - Scientific Letters of the University of Zilina, Vol. 24, Issue 4, 2022. – p. 288-300
[14] Kadyrov A., Sarsembekov B., Ganyukov A., Suyunbaev Sh., Sinelnikov K. Ultrasonic unit for reducing the toxicity of diesel vehicle exhaust gases. // Communications - Scientific Letters of the University of Zilina, Vol. 24, Issue 3, 2022. – p. 189-198
[15] Volnov A.S., Gerassimov E.M., Tretyak L.N. Method for cleaning exhaust gases of an internal combustion engine and a device for its implementation. *Patent RF*, No. 2563950, 2014.
[16] Khmelev V.N., Savin I.I., Tsyganok S.N., Barsukov R.V., Levin S.V., S.S. Khmelev. Ultrasonic vibration system. *Patent RF*, No. RU 2 323 788 C1, 2006.
[17] Menon G., Pego R.L. Approach to self-similarity in Smoluchowski's coagulation equations // Communications on pure and applied mathematics, Vol. 57, Issue 9, 2004
[18] Ernst M.H., Ziff R.M., Hendriks E.M. Coagulation processes with a phase transition // Journal of Colloid and Interface Science, Vol. 97, Issue 1,1984. – p. 266-277
[19] Pak I., Baurova N., Kurmasheva B., Karsakova A., Кadyrova I. Technical and Economic Efficiency of Devices for Ultrasonic Cleaning of City Bus Exhaust Gases. // Bulletin of L.N. Gumilyov Eurasian National University Technical Science and Technology Series. Vol.139, Issue 2, 2022. – p.133–142.
[20] Kadyrov A., Bembenek M., Sarsembekov B., Kukesheva A., Nurkusheva S. The Influence of the Frequency of Ultrasound on the Exhaust Gas Purification Process in a Diesel Car Muffler. // Appl. Sci. Vol.14, Issue 12, 2024, – p. 1-19.

Information of the author

Igor Pak, PhD, senior teacher, Abylkas Saginov Karaganda Technical University
e-mail: i.pak@mail.ru

DOI 10.52209/2706-977X_2024_2_64 **IRSTI 81.09.01** **UDC 616.314**

Reducing the Issues of Implements in the Human Body by Applying Hydroxyapatite (HAP) in Modern Biomedicine: Review

Al-Khafaji Z. [1, 2]*, Kazem M.A.[3], Radhi N.S.[4], Falah M[5], Hadi Z.M.[6]
[1]Universiti Kebangsaan Malaysia, Selangor, Malaysia
[2]Scientific Research Center, Al-Ayen University, Thi-Qar, Iraq
[3]Al-Zahraa University for women, Karbala, Iraq
[4]University of Babylon/ Materials Engineering College/ Babil. Babylon, Iraq
[5]College of Engineering and Engineering Techniques, AL-Mustaqbal University, Babylon, Iraq
[6] University of Babylon chemistry sciences, Babylon, Iraq
* corresponding author

Abstract. Hydroxyapatite (HAP) is a naturally occurring mineral that has received increasing attention as a biomaterial for use in biomedical applications. HAP is biocompatible and has excellent osteoconductivity and bone-bonding properties, making it a promising candidate for use in a range of medical applications, including bone regeneration, dental implants, and drug delivery. This comprehensive review provides an overview of the current state of knowledge on the use of HAP in biomedical applications. The review covers the basic chemistry and properties of HAP, as well as its synthesis and processing techniques. It also discusses the different forms in which HAP can be used, including powders, coatings, and composites, and their respective advantages and limitations. The review goes on to discuss the various biomedical applications of HAP, including bone regeneration, dental implants, and drug delivery. For each application, the review examines the specific properties of HAP that make it suitable for the given purpose, as well as the challenges associated with its use. The review also addresses some of the limitations and challenges associated with the use of HAP in biomedical applications. These include the relatively low mechanical strength of HAP compared to other materials, its susceptibility to degradation over time, and its potential to elicit an immune response in some patients. Overall, this review demonstrates the potential of HAP as a building block for better health and highlights the need for continued research and development in this field to fully realize its potential in biomedical applications.

Keywords: implements, human body, hydroxyapatite, biomaterials, corrosion reduction, biodegradable.

1. Introduction

The Egyptians developed a similar custom of cutting precious metals and pegging them onto the jawbone some 2,000 years later. In an Egyptian pharaoh from 1,000 B.C., a metal implant was discovered for the first time [1], [2], [3]. Numerous skulls with fake or transplanted teeth made of elephant ivory or precious stones like jade have also been discovered by archaeologists. Dr. Wilson Popenoe and his wife Dorothy Popenoe discovered a young woman's skull in Honduras in 1931. Three of her lower jaw's teeth were gone, and shells had filled the spaces. The shells were fashioned to resemble the form of teeth. These teeth were created for function rather than beauty since there was bone development and calculus. Dental implants are now the standard treatment for tooth loss, thanks to modern technology [4].

The study of biomaterials is crucial for humankind's survival and longevity, as well as that of the elderly population, who need biomedical implantation to extend their lives, and some of the less fortunate people born with congenital heart disease [5]. Geriatric doctors are needed to treat various illnesses in the elderly since the body's components have worn down after years of performing their intended functions. One of the most common ailments, arthritis, affects individuals of all ages, including sometimes young people. It damages their quality of life by making them immobile and causing excruciating pain. Despite significant scientific discoveries, the etiology of this illness is still unclear [6]. Young and active individuals, such as athletes, often need replacements owing to fractures and excessive strain, in addition to sick patients. The demand for biomaterials was particularly urgent following the two world wars, and in the modern environment of international terrorism, this topic has acquired considerably more relevance [7].

The usage of iron and gold in dentistry [8], wood for toe replacements, and linen for sutures by the Romans and Egyptians date back more than 4,000 years, although these civilizations had little understanding of the issue of corrosion at the time [9], [10]. After World War II, additional materials such as titanium, stainless steel [11], [12], [13], [14], silicone, Teflon, and nylon were utilized. Implantology has grown in importance, and bio-implants are frequently utilized in veterinary medicine, experimental surgery, histopathology, immunology, neurosurgery, cardiovascular surgery, ophthalmology, dentistry, orthopedics, and plastic and reconstructive surgery [15]. This is due to the availability of improved diagnostic tools and improvements in our knowledge of substances and surgical techniques (Fig. 1). For the fabrication of bioimplants, a variety of materials, including composites, ceramics, polymers, alloys, metals, were employed extensively. These implants interact with bones and tissues in various biological settings with extremely varied physic-chemical makeups, which is a challenging issue.

The biomaterial acceptance by the live body is the most important criterion for selecting. The implanted substance must not result in any negative side impacts, including toxicity, inflammation, or allergy, immediately after surgery or throughout recovery. In addition to fracture toughness and fatigue strength, biomaterials must have adequate mechanical strength to withstand the forces they are exposed to without breaking. A bioimplant must have extremely high wear and corrosion resistance in highly corrosive body environments and under different loading conditions. A biomaterial should last longer and not stop working before the individual dies. It is clear from this criterion that elderly patients must serve a min of 15 to 20 years, whereas younger patients must serve a min of more than 20 years. Three key elements greatly influence a biomaterial's or implant's success: i) the biomaterial's qualities (tribological, chemical, and mechanical); (ii) the implant's biocompatibility; and (iii) the recipient's health and the surgeon's skill. Despite working effectively in the human system [16], the presently utilized materials chosen based on the above characteristics often fail after 12 to 15 years, necessitating revision surgery to restore the system's performance. Their failure may be attributed to various factors, including production, biocompatibility, and surgical, chemical, mechanical, and tribological problems. The implant failure in corrosion has remained one of the most difficult clinical difficulties out of the complications.

The following is a comprehensive list of the many different applications that make use of biomaterials, which are used by medical professionals, academics, and bio-engineers [17]:

- implants in medicine include dental implants, implants for hearing loss, tendons, ligaments, prosthetic joints, grafts, stents, heart valves, and devices that stimulate nerves;
- techniques that hasten the recovery of human tissues, such as staples, clips, and sutures for the closure of wounds, as well as dressings that dissolve on their own;
- human tissue regeneration is accomplished by incorporating biomaterial supports or scaffolds, cells, and bioactive chemicals into the process. One example is a hydrogel that can regenerate bone, while another is a human bladder that was created in a lab;
- molecular probes and nanoparticles are capable of penetrating biological barriers and contributing to molecular-level imaging and treatment of cancer;
- biosensors that can determine the presence of a drug, as well as its concentration, and send that information. Instruments that measure blood glucose levels and sensors that track brain activity are two examples;
- systems for the delivery of pharmaceuticals that may either transport or administer drugs to a disease target.

A few instances of this would be drug-coated vascular stents and implanted chemotherapy wafers for patients with cancer.

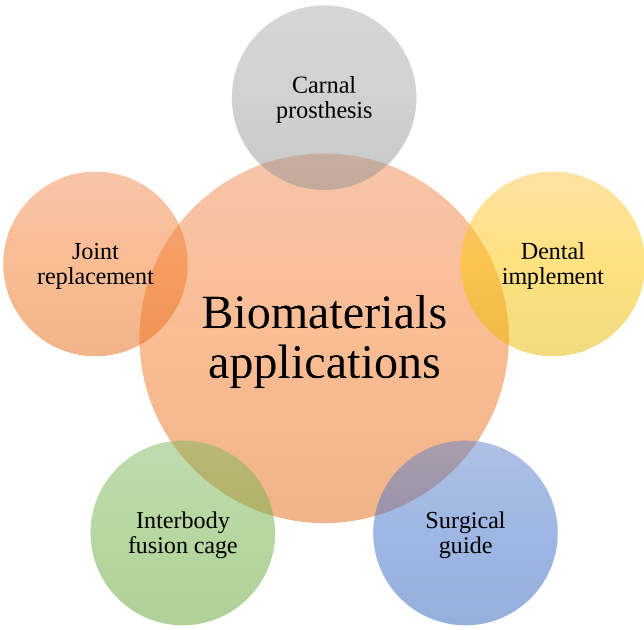

Fig. 1. - The biomaterials applications [18]

2. Types of biomaterials

2.1 Natural

Chitosan, bone, collagen, and starch are examples of natural materials, while ceramics, polymers, and metals are the raw ingredients that laboratories use to produce synthetic materials. With hybrid materials, both types of materials are included into the final product. Because of their one-of-a-kind mechanical, biological, chemical, and physical properties, these are the types of materials that are chosen to be used as biomaterials. These properties allow them to be used both within and outside of the human body. There are a variety of methods in which non-metallic and metallic biomaterials may be coupled, including ionically, covalently, and both ways. Cell therapy is an innovative approach that is still in the process of evolving as a strategy for healing a damaged heart. Tissue engineering may be used to make cardiac patches that have been modified and filled with bone marrow or mesenchymal stem cells to provide a repair that is as close to seeming natural as is humanly feasible. Research has been done in this field on both naturally occurring and artificially produced biomaterials.

Osteoinduction is a technique of bone healing that is gaining in popularity. This approach encourages the creation of bone by either changing the surface of the damaged location or infusing growth factors or bone marrow stem cells there. Without the need for invasive and uncomfortable surgery, this might speed up the process of bones healing. It's possible that mesenchymal stem cells are the parents of ligament fibroblasts. On the other hand, stem cells extracted from bone marrow have the potential to be of great use in the field of skin tissue engineering. It's possible that stem cells originating from fat might speed up the healing process in wounded tissue by boosting collagen production and the migration of skin fibroblasts.

2.2 Synthetic

2.2.1 *Bioceramics*

Bioceramics are frequently employed in a variety of medical procedures, including dental implants, bone transplants, artificial tendons, and hip replacements. Although black pyrolytic carbons are easy to produce and are extremely compatible with human tissues, they are not suitable for implant that is visible from the outside, like the ones employed in the mouth. This includes dental implants. Heart valves, ligaments, tendons, and composite implants are all examples of applications that need great tensile strength, and these materials are used in all of these areas. In addition, bioceramics are being investigated as a potential method for the delivery of medicines, genes (for use in gene therapy), and cancer therapies.

Bioceramics do not cause inflammation, are not carcinogenic, do not cause toxicity, and do not cause cancer. In addition to having a pleasing appearance, they have a high compressive strength and may be dyed to any color chosen. In addition to this, they are resistant to corrosion and generate excellent articulating surfaces. Nevertheless, they are limited in scope due to their brittleness, which renders them prone to shattering when subjected to significant force, as well as the difficulties associated with making them. They might be classified as inert, biodegradable, or bioactive based on their distinct characteristics. This section contains resorbable alumina [19], [20], zirconia [21], [22], carbons, glass ceramics, hydroxyapatites, aluminate, and calcium phosphate. In situations requiring electrical conductivity, inert metals of the third kind are often used. However, for suture materials, biodegradable options are preferable. When used in applications such as vascular stents, bioabsorbable materials offer a framework for healing processes that are both permanent and temporary at the same time. Tendons, ligaments, hips, artificial bones, teeth, and Knees are all examples of places that use resorbable materials. Resorbable materials are also used in orthopedic surgery (calcium aluminate) and dentistry (calcium phosphate). In areas where more bone is required, glass ceramics and several other materials that are either semi-inert or bioactive are applied.

On the other hand, hydroxyapatite is used to manufacture coatings, fillers, and bone grafts for metallic implants [23]. Inert bio-ceramics [24] such as zirconia and alumina are used in the construction of hip and dental implantation. Carbon may be found in bone scaffolds and heart valves, as well as in chemicals that stimulate cartilage regeneration. Silicon nitride is used in the fabrication of spinal fusion implant.

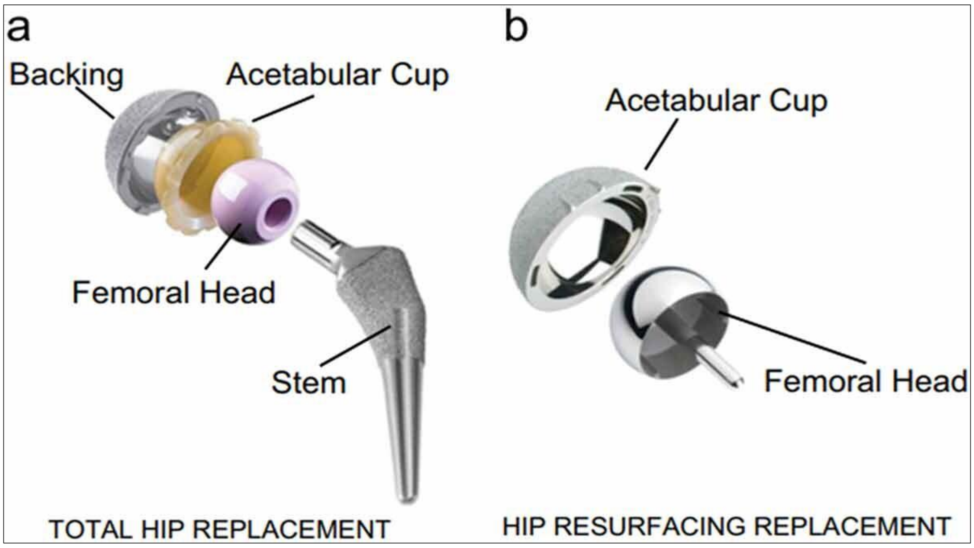

Fig. 2. - Hip implants can use bioceramics [25]

2.2.2 *Polymers*

Natural polymers, including collagen and starch, were accessible and degraded quickly, making them suited for use in biomaterials. Implants, single-use medical equipment, and dental and prosthetic components are increasingly often made utilizing synthetic polymers. Interestingly, materials like polyurethane (PU), polyethylene terephthalate

(PEEP), polymethyl methacrylate (PMMA), polyethylene (PE), and polypropylene (PP) were developed for non-medical uses in numerous biomedicine due to how closely their physical and mechanical properties resemble human body tissues.

PP may be utilized to make extra-corporeal membrane oxygenation (ECMO) membranes, hernia mesh, artificial blood vessel grafts, ECMO membranes, and suture material. PMMA and PEEP are also utilized to create vascular grafts for dental implants and bone types of cement. In addition to medication delivery mechanisms, PU is utilized to create wound dressings, breast implants, blood artery grafts, and patches for the heart muscle. PE is often utilized to create tubes for surgical implants, hip socket liners, and drainage for catheters.

Probes that potentially enhance positron emission tomography (PET) imaging are made from polymers. Polymer is utilized in Microelectron Mechanical Systems (MEMS), sometimes called lab-on-a-chip, which lowers the price of single-use devices. Because of their exceptional capacity for adsorption, polymers are increasingly being used in drug-eluting stents (DES). In order to strengthen the arterial wall, they might, among other things, be coated with anti-inflammatory drugs, anti-plaque steroids, or endothelial cells. Other possible coatings include: Gene-eluting stents are an example of a potential future breakthrough that might deliver a domestic production of RNA or DNA in order to inhibit certain genes that contribute to restenosis [26]. Polymers make it easy to create low-cost fibers, films, sheets, or synthetic latex. They are susceptible to pollution from outside the body because of their quick assimilation of protein and water [27]. Their sensitivity to heat and chemicals makes sterilizing more difficult. Another drawback is their propensity to release undesired substances into the fluids they touch with. They often wear out or break down as well. Eventually, due to their extreme misuse and delayed biodegradability, plastics have already been phased out.

2.2.3 Metals

Metals is frequently utilized in medical devices including pacemaker wires, vascular stents, and implants for hip and knee joints because it is very resistant to corrosion and has a high level of mechanical strength. When it comes to various applications, alloys and pure metals are both put to be used [28], [29]. As a protective coating, either bioceramics or very thin coatings of polymer are added to the metals. There are occasions when these qualities are innately incorporated into the surface. These biomaterials have a powerful memory, and it is not difficult to sterilize or create them according to the requirements. On the other hand, they could be inflexible and difficult to produce, both of which could make osseointegration more difficult. Even allergic reactions might possibly be triggered by them [30].

Most metallic biomaterials may be categorized as belonging to one of these three groups: alloys of cobalt and chromium; stainless steel; or pure titanium or its alloys. Titanium alloy is superior to the other two in terms of its low weight, strength, and resistance to corrosion in human tissues [31], [32]. These characteristics make titanium alloy a very useful material. Electrode leads, joint prostheses, and internal screws may all be fabricated using this material. Titanium, on the other hand, has a joint surface function that is inferior to that of other materials, which results in quick wear and increases the risk of osteoarthritis. Vanadium, which is often included in these alloys, is known to cause tissue damage over time. Along the same lines as aluminum, it may also have a role in the development of neurological diseases such as Alzheimer's disease (AD). Stainless steel has shown to be a useful material for a variety of medical applications, including bone plates, guide wires for endoscopic procedures, and blood vessel transplants. Cobalt-chromium alloys are used in the treatment of fractures and may be found in artificial heart valves, joint prostheses, dental implants, screws, and plates.

3. Metallic Implants

Surgical stainless steel 316 L (SS-316L) [33], cobalt-chromium (CoCr) alloys, and Titanium (Ti) alloys seem to be the bio-metallic inert metals that are the most often used for bone remodeling, angioplasty, and fracture repair [34]. Due to its better mechanical qualities and long-term stability under highly reactive in-vivo environments [34], this is a significant factor. While it is believed that these materials have a low rate of corrosion, it is essential to bear in mind that material deterioration may be caused by wear, friction, and a very hostile microenvironment [35]. This might result in the release of metallic ions that are undesirable. Inflammatory reactions, local tissue damage, including progressive osteolysis of adjacent tissues, systemic injury, and metal hypersensitivity are some of the potential outcomes of this. Osteolysis has the potential to affect the fixation of the implant as well as, in the long run, its loading and force transmission, which may lead to the failure of the implant, the need for corrective surgery, or issues following the treatment [36].

3.1 Challenges with Permanent Metals Implants

We have previously demonstrated that 3D printing can adequately support the load-bearing capacity of injured musculoskeletal tissue, better matching the anatomical specifics of each patient. Researchers have also discussed the controlled introduction of porosity to match the implant's Young's modulus and stiffness to the nearby cancellous and cortical bone (Table 1), thereby limiting stress shielding. This severe issue frequently leads to the refracture of the already weak bone. The stresses on that region of bone tissue directly affect bone development and density. Because titanium alloys are more than ten times stronger than cortical bone, utilizing them drastically reduces the stresses applied to the bone, leading to loss of density and deterioration [37]. These advantages may be achieved while maintaining strong compressive resistance and adequate compressive strengths and the added advantage of better osseointegration.

Hard-tissue replacement implies that the bioceramic device will be used for load-bearing applications. Although it is desirable to have a device with a sufficient porosity for the surrounding tissue to infiltrate and attach to the device, the most important and immediate property is the strength of the device. In order to accomplish this, one must manufacture a bioceramic implant with a density and strength sufficient to mimic that of bone. However, if the bioceramic part is significantly stronger than the surrounding bone, one runs into the common problem seen with metals called stress shielding. The density of the bioceramic greatly determines its overall strength. As the density increases so does the overall strength of the bioceramic. Some of the techniques used to manufacture dense bioceramics are injection molding, gel casting, bicontinuous microemulsion, inverse microemulsion, emulsion, and additives [38].

Table 1. The differences between the mechanical characteristics of metal implants with bone tissue [39], [40]

Tissue/Material	Modulus of Young (GPa)	Yield Strength (MPa)	Compression Strength (MPa)	Tensile Strength (MPa)
Cortical bone	7–30		(1–2.3) x10^2	(1.64–2.4) x10^2
Cancellous bone	0.01–3.0		2–12	
Ti_6Al_4V (cast)	1.14 x10^2	(7.6–8.8)x10^2		(8.95–9.30) x10^2
Ti_6Al_4V (wrought)	1.14 x10^2	(8.27–11.03) x10^2	(8.96–11.72) x10^2	(8.6–9.65) x10^2
SS-316L	1.93 x10^2	(1.7–3.1) x10^2	480–620	(5.4–10) x10^2
CoCrMo Alloy	2.4 x10^2	(5–15)x10^2		(9–15.4) x10^2
Mg (99.9%, cast)	41	21	40	87
Mg (99.9%, wrought)	41	1 x10^2	(1–1.4) x10^2	1.8 x10^2
Hydroxyapatite	50	6.91 x10^2	9.17 x10^2	10.2

On the other hand, inert metal scaffolds could not be easily filled in situ with bioactive chemicals or cells, which partly restricts their application for full tissue regeneration. This is in contrast to biodegradable ceramic and polymer [41]. Consequently, controlling surface chemistry necessitates post-processing, including functionalizing the surfaces with pharmaceutically relevant biomolecules, including paracetamol [42], coupled onto phosphonic acid-based self-assembled monolayers.

Moreover, there is a possibility that the leaching of metallic ions from SS, Ti, and Co-Cr and Ti alloys [43] into the peri-implant milieu may rise due to the insertion of interconnected pores, which considerably increases the surface-to-volume proportion. Since surface oxide coatings are recognized to restrict ion release in-vivo, this might be especially important once utilized in situations with low levels of dissolved oxygen [44]. The presence of proteins, cells, and inorganic ions in bodily fluids may speed up ion release even more. Worrying and stress-related wear may encourage the production of metallic ions and the elimination of the oxide. The interactions between anions, water molecules, and highly reactive ions might also be influenced by the inorganic salts, oxides, hydroxides, and other chemicals that emerge from these reactions. Sarcoma might form because of ions' interactions with host cells.

3.2 Biodegradable Biometals

When full tissue regeneration is anticipated, utilizing biodegradable metals instead of permanent metallic implants may result in considerably superior methods of fracture fixing. For cardiovascular and orthopedic uses, zinc (Zn) [22], iron (Fe), and magnesium (Mg) alloys seem to be currently the best investigated biodegradable metals because they provide good in-vivo biocompatibility, a controlled degradation profile, and enough mechanical strength to support bone throughout the regeneration process. Bioresorbable polymers, such as polylactic-glycolic acid (PLGA), polyglycolide (PGA), or copolymer polylactide (PLA), are brittle and might not be appropriate for applications in which significant forces have been applied to the implant. In contrast, bioresorbable metals exhibit superior mechanical behavior [37], [45]. In addition, unlike Mg, Fe, and Zi, whose biodegradation byproducts are readily metabolized by the host cells, polymer breakdown byproducts may cause necrosis and inflammatory tissue reactions [39].

3.3 Toxicity

A Biomaterial should carry out its intended task inside a live organism without harming other tissues and organs. Biomaterials should be non-toxic to avoid unintended interactions with organs and tissues. The compounds that are released from a biomaterial when it is in-vivo are considered to be poisonous. A biomaterial should not release any substances into the environment unless that is what it is designed to accomplish. Nontoxicity refers to a biomaterial's lack of pyrogenicity, allergenicity, carcinogenicity, compatibility with blood, and inflammogenicity [46]. A biomaterial may be created with toxicity for a specific purpose. For instance, hazardous biomaterials are investigated during cancer immunotherapy testing, both in vivo and in vitro, and toxic biomaterials are utilized to manipulate and control cancer cells [47]. According to a recent study: "Advanced nano biomaterials including liposomes, polymers, and silica are essential for the transport of immunomodulators and pharmaceuticals. These nano biomaterials-based delivery methods have the potential to concurrently lessen harmful side effects while successfully promoting antitumor immune responses [48]." This illustrates how a biomaterial's biocompatibility may be changed to generate any desired function.

4. Hydroxyapatite

A common bioceramic utilized as a biomaterial for bone replacement is hydroxyapatite (HA), which is the calcium phosphate with the chemical formula $Ca_{10}(PO_4)_6(OH)_2$. HA has many applications, such as bone fillers, scaffolds for bone tissue creation, implant coatings, soft tissue healing, and drug delivery systems [49]. It is also intriguing due to its biocompatibilities, osteoconductivity, non-inflammatory qualities, and mechanical properties. About 60–70% of the inorganic material in bone tissue is hydroxyapatite [50]. According to Figure 3, the calcium phosphate compound family is made up of molecules with the molecular formula $Ca_{10}(PO_4)_6(OH)_2$, which are mostly made up of the elements phosphorus and calcium.

Because of its bio-mimicking qualities, this bioceramic is compatible with natural bone. For the manufacture of HA, several synthetic approaches have been widely described [51]. Although several synthetic techniques have been devised to produce HA with certain properties, it is still difficult since harmful intermediate intermediates might arise. The sol-gel technique, hydrothermal reaction, co-precipitation reaction, and mechano-chemical approaches may all be utilized to synthesize HA [52].

Fig. 3. - HAp-Coated Femoral Stem of Hip Surgery Implants [53]

4.1 Crystal Structure of HAP

With the chemical formula $Ca_{10}(PO_4)_6(OH)_2$, hydroxyapatite (HAP) seems to have a crystalline hexagon structure. Hydroxyapatite nanoparticles (nano-HAP) have two different binding sites. For instance, nano-HAP contains positively charged calcium cations (Ca^{2+}) on the sides and negative charges phosphate anions (PO_4^{3-}) at both ends, as seen in Figure 4. Human bones need HAP since they are made up of 30percent collagen, 70percent low-crystalline or amorphous apatite, and 5% bone marrow cells [54].

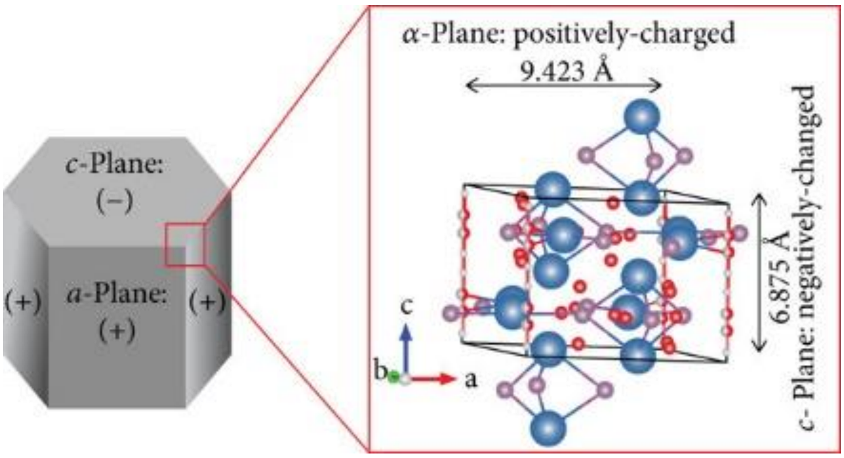

Fig.4. - The Crystalline Structure of HAP [55]

4.2 Properties and Advantages of HAP

The Magnitudes provided for HAP's physical characteristics, its mechanical and physical qualities, and some of its benefits are demonstrated in Table 2. The fracture toughness, tensile strength, and bending strength of an extremely dense HAP. The ranges of HAP's tensile strength, compressive strength, and bending Magnitudes are 38-300 MPa, 120-150 MPa, and 38-250 MPa, respectively. Numerous elements, including the random strength distribution and the impacts of ion impurities, grain size, and residual micro-porosity, all contribute to the huge scatter. The strength rises with increasing Ca/P proportion, peaks at Ca/P of 1.67, and then rapidly falls to Ca/P less than 1.67. In dense HAP, Young's modulus ranges from 35 to 120 GPa based on impurities and residual porosity. Because of grain boundary slip, dense HAP ceramics demonstrate super-plasticity at temperatures between 1000 and 1100 degrees centigrade [56].

Bone's mechanical characteristics are significantly influenced by humidity, the kind and direction of the applied force, and the bone's position inside the body. When it comes to direct bonding with bones, osteoconductivity, bioactivity, and biocompatibility, HAP demonstrates important features as a biomaterial. However, its mechanical characteristics were subpar, as demonstrated by its low fracture toughness (K_{IC} is 0.7 to 1.2 MPa m0.5). As a result, this drastically limits its scope of use in orthopedics. Nevertheless, it is still a fantastic choice for covering metal prostheses or fixing tiny bone flaws [32], [56].

Table 2. Principal characteristics of HAP [56]

Characteristics	**Magnitude**	**Characteristics**	**Magnitude**
Density	3.16 g/cm^3	Poisson's proportion	0.27
Decomposition temp	Less than 1000 degree centigrade	Fracture Energy	2.3-20 J/m^2
Dielectric constant	7.40-10.47	Fracture toughness	0.7-1.2MPa.$m^{0.5}$ (reduction in porosity)
Thermal conductivity	0.013 W/cm.K	Fracture hardness	3-7 GPa (dense)
Melting point	1614 degree centigrade	Bio-compatibility	High
Tensile strength	38-300MPa (dense) ~3MPa (porous)	Bio-degradations	Low
Bending strength	38-250 MPa (dense) 2-11 MPa (porous)	Bioactivity	High
Compressive strength	120-900 MPa (dense) 2-100 MPa (porous)	Osteo-conduction	High
Young's elastic modulus	35-120 GPa	-----	-----

Due to its advantageous biological features, such as osteoconduction, bioactivity, bioaffinity, biocompatibility [57], osteoinduction [58], and osteointegration [59], HAP bioceramics have found widespread use as artificial bone replacements (in certain conditions). Because HAP only possesses calcium and phosphate ions, no adverse reports of either local or systemic toxicity have been from any studies conducted. When the implant is placed, the newly created bone bonds directly to the HAP via a layer of carbonated calcium-deficient apatite that is located at the bone-implant contact [60], [61]. The HAP surface allows for osteoblastic cell adhesion, proliferation, and differentiation. As a result, new bone is produced by creeping substitution from the live bone that is next to the defect. HAP scaffolds have the ability to bind to and concentrate bone morphogenetic proteins (BMPs) in vivo, making them suitable candidates for use as delivery vehicles for cytokines [62].

A vital component of the process of regeneration is the interaction of apatite with the biological tissues of the body. Changes in manufacturing technique, size, the nature of materials, and other factors are causing conceptual shifts in mineralization and tissue contact. These shifts are bringing about new ways of thinking about these processes. Scaffolding has been used to initiate the earliest stages of bone regeneration. Otto Herbert Schmitt is credited with first using the word "biomimetics" in the 1950s. This biological process causes the creation of highly ordered materials with hybrid composition. It starts by designing and synthesizing molecules that can self-organize spontaneously to higher-order structures [60]. This biological process also causes the production of highly ordered materials with hybrid composition.

The HAP's interactions with the tissues are very significant. Understanding the in vivo host reactions while dealing with HAP is essential. In general, the action mechanism of a biomaterial is regarded to be biocompatible, bioinert, biotolerant, and bioactive, and it also includes materials that are bioresorbable. These modifications in knowledge result from improvements in the characteristics and manufacturing technology, as well as a greater comprehension of how materials interact with the tissues. The most recent developments in nanotechnology have led to the creation of HAP in a more bioactive or bioresorbable form, leading to this field's cutting edge. Even if the foreign body is biocompatible, the tissue response to it will still create a capsule, resulting in the foreign entity being isolated. Bioinert materials will not demonstrate any beneficial interactions and will not release any hazardous elements. Encapsulation describes the measurement of the bioinert-ness of a substance, and the body or host tissue will separate such compounds via encapsulation [60].

4.2.1 *Disadvantages*

Because synthetic HAP has desirable qualities as a biomaterial, including osteoconductivity, bioactivity, and biocompatibility, this material has found widespread use as a replacement for bone, a covering for metallic implants, a scaffold for tissue engineering, and a carrier for the transport of drugs. For use in biomedical applications, HAP may be formulated into various forms, including coatings, cement, paste, granules, and dense and porous blocks [63]. One of the most significant drawbacks of HAP is its low strength, which makes it impossible to manufacture high load-bearing implants wholly out of HAP [64]. This is the case even though HAP has various beneficial properties. The nanocrystalline HAP found in bones and teeth is the primary structural component. Grafting with HAP is performed in sinus augmentation, ridge reconstruction, and bone defect repair procedures.

Brittleness, poor tensile strength, and fracture toughness are just some of the issues associated with HAP. Nevertheless, because of its weak mechanical qualities, hydroxyapatite cannot be employed in its bulk form for load-bearing applications, including orthopedics. Specifically, the material's fatigue properties are to blame for this limitation. When utilizing HAP as a delivery system, one of the most significant drawbacks is that the sintering process may lead to the particles' agglomeration, which, in the context of gene delivery, results in a reduction in the effectiveness of the delivery system's ability to transfect cells. Simple ultrasound-assisted precipitation with the addition of glycosaminoglycans was used in the research carried out by Han et al. [65], which resulted in the production of well-dispersed HAP nanoparticles.

Typical bursitis or tendinitis of the shoulder may be caused by the deposition of hydroxyapatite crystals in the tendons and bursae of the shoulder. The area above the greater trochanter is the second most prevalent place for the deposition of this substance [66]. Additionally, it may produce discomfort in the region of the wrist or elbow. Hydroxyapatite has been reported to deposit in soft tissues in several systemic disorders, including renal osteodystrophy, dermatomyositis, and scleroderma. This phenomenon has been seen. Nevertheless, individuals have lately appeared with hydroxyapatite deposition in many tendinous and soft tissue locations despite the absence of an underlying systemic illness [67].

The ineffective adhesion of HAP to the metallic surface is the primary source of worry throughout the process of applying HAP coatings. This is because the adhesive connection between the metallic load-bearing locations and the HAP layer is weak [68]. As a result of HAP's less-than-perfect crystalline structure, the HAP film connection on the metallic surface begins to weaken and abruptly breaks down [69]. Due to this failure, metallic ions are discharged into the bodily environment as the metal surface becomes exposed to the surrounding environment [70]. To improve the adherence of HAP films, surface modifying agents are necessary. These agents contribute to creating a durable coating atop the metallic surface, which helps achieve the desired goal. Because of its biocompatibility, HAP, the primary inorganic component of hard tissues (bones), has been used in various biomedical applications over the last half-century. On the other hand, research conducted in the past and published found that HAP has the characteristics of brittle ceramics that cannot resist the weight of a load [71].

4.3 HAP Preparation Methods

Techniques that are often used to manufacture HAP include, but are not limited to, the hydrothermal process, the precipitation technique, the solvothermal technique, the spontaneous combustion technique, the micro-emulsion technique, the ultrasonic synthesis technique, the bionic approach, and the solid-state reaction technique, which includes both the wet technique and the dry method. The hydrothermal technique, the solvent, the thermal technique, and the precipitation chemical technique [72] are the main techniques used by scientific research workers in recent years. These three procedures also have the most widespread application, the lowest cost, and the best HAP complete properties achieved. The HAP was produced by Chaudhari et al. [73] by the use of the following reaction:

$$10\mathrm{CaO} + \mathrm{K_2HPO_4} + 4\mathrm{H_2O} \rightarrow \mathrm{Ca_{10}(PO_4)_6(OH)_2} + 12\mathrm{KOH}$$

Some of the processes demand a high processing temperature, a significant investment in the necessary raw materials, and an intricate procedure for the actual synthesis. The chemical precipitation approach provides several benefits, including the capacity to create nanosized HAP powder in large quantities and with a high degree of purity, as well as simple equipment and a cheap cost. The primary properties of HAP, such as its Ca/P proportion, crystal size, and morphology, determine the particular applications that may be carried out with this material [74].

Many research investigations have shown that using high-power ultrasound during the wet-chemical synthesis process may increase hydroxyapatite levels [75]. Sono-synthesis, also known as ultrasonically aided synthesis, has shown to be an extremely effective method for the manufacture of nanostructured hydroxyapatite of a high grade [76]. The manufacturing of nanospheres with a core and a shell, as well as composites, is made possible through the ultrasonic approach, which results in the formation of nanocrystalline and changed hydroxyapatite particles [77].

A technique for synthesizing hydroxyapatite nanoparticles was created utilizing Ca and P sources from a chemical reaction of 99.0% $Ca(OH)_2$ and 85 percent H_3PO_4. This approach aimed to decrease or eliminate hazardous emissions, often the results of most synthetic methods used to make hydroxyapatite. Because these chemicals do not leave behind any leftover hazardous anions, there was no requirement for extra cleaning [78].

4.4 Applications of HAP

The interaction between protein molecules and inorganic materials is of pivotal interest in industry, biochemistry, biosensors, biomineralization, and biomaterials. As mentioned earlier, HAP crystals have two binding sites, for example, calcium cations (Ca^{2+}) and phosphate anions (PO_4^{3-}), owing to their chemical composition and specific orientation. A depiction of the most significant applications is placed below [79], [80], [81]:

4.4.1 *HAP as a Coating Material*

Designing a bone-implanting material that may be utilized to repair a bone defect and rebuild the bone is essential for restoring a damaged bone. The process of creating appropriate materials for bone implants is not without its challenges. For example, the first challenge often arises when synchronizing the implanting material and bone throughout the bone remodeling process (resorption and reparative). The implant substance should not negatively impact the immune system. Nevertheless, the materials utilized for implanting sometimes resorb prior to osteogenesis, making them useless. Other times, infections brought on by the implants cause illness and even death, which is exceedingly expensive for the patient and society. Due to these factors, a method for creating acceptable bone tissue regenerating implantation must be developed. Recently, a method of enhancing the bioactivity and compatibility of the implanting material included coating an implant with a biocompatible and bioactive substance. HAP is the most often utilized coating agent. Additionally, applying HAP to the surfaces of implanting substances (such as titanium alloys) improves osteointegration with bone [80], [82].

4.4.2 *HA P as a Drug Delivery Carrier*

The "P" and "Ca" locations on HAP and its rough surface make it easier for proteins to attach to them during mineralization. The interactions of amino acids with HAP have demonstrated the significance of the rough surface. HAP nanorods and nanoparticles are utilized as a medium for the transport of different medicines and proteins (growth factors). For instance, the drug-loaded/modified HAP nanorods/nanoparticles have been combined with a polymeric solution to deliver the drug-loaded HAP to the target region [83].

4.4.3HAP-Based Composite Materials

Most polymeric composites employ HAP as an enforcer to give the composite material mechanical strength and bioactivity. There has been much written on HAP's role in bone tissue regeneration. By grafting proteins and medications onto the surface of HAP, scientists have created HAP/polymer scaffolds that may be utilized to distribute pharmaceuticals, promote bone tissue repair, and treat conditions like osteoporosis. [23], [84].

4.4.4 HAP-Based Ceramics in Bone Tissue Regeneration

The use of HAP in pristine, composite, or ceramic types for the regeneration of bone tissue was already made possible by the resemblance between HAP and the inorganic cement of real bone. The chosen materials for an implantation must-have qualities comparable to those of natural bone to accomplish the intended aim (safe and acceptable bone regeneration). Several HAP bio-ceramics were developed that resemble real bone. Nevertheless, as was already said, the implantation should provide a setting similar to the natural one. For instance, in addition to other things, the implant must be mechanically strong near the bone [23], [85].

In addition to being an implantable material, HAP has been employed in cancer treatment, gene delivery, and bio-imaging. Gene therapy has long been recognized as holding promise for the treatment of a variety of incurable diseases by replacing the missing or damaged genes, catalyzing the destruction of cancer cells, usually causing the cancer cells to transform back into normal tissue, encouraging the growth of new tissue, or stimulating regeneration of the damaged tissue [86]. Nevertheless, largely due to the absence of a reliable and capable vehicle for the delivery of genes, this promise remains unmet [23], [85].

5. Methodology

The current review presents the behavior of pure implements and the improvements in these implements after applying HAP [87]

6. Results and discussion

To increase the biocompatibility of metal dental implants and bone osteointegration, Fathi and Azam [87] developed and manufactured a unique surface composite coating on metal substrate. In order to create a unique double-layer hydroxyapatite/tantalum (HAP/Ta) coating, SS-316L was employed as the metallic substrate. Physical vapor deposition was utilized to create the tantalum coating, while plasma spraying was utilized to apply the HAP layer. X-ray diffraction (XRD) and scan electron microscopy (SEM) methods were utilized to study the coating characteristics. In order to assess the corrosion behavior of the coated and uncoated samples as a sign of biocompatibility, electrochemical polarisation experiments have been carried out in two kinds of physiological solutions at 37±1degree centigrade. According to the findings, corrosion current density significantly decreased for specimens coated with HAP/Ta and was substantially lower than the value measured for SS-316L that had not been coated. The innovative double-layer HAP/Ta composite coating may enhance the SS-316L dental implant's biocompatibility by reducing corrosion.

Figure 5 depicts the HAP/Ta composite coating on SS-316L XRD Pattern. There have been many sharp peaks and a low backdrop in the plot of intensity against 2θ, which is a sign of the HAP/Ta composite coating's crystalline structure HAP coating.

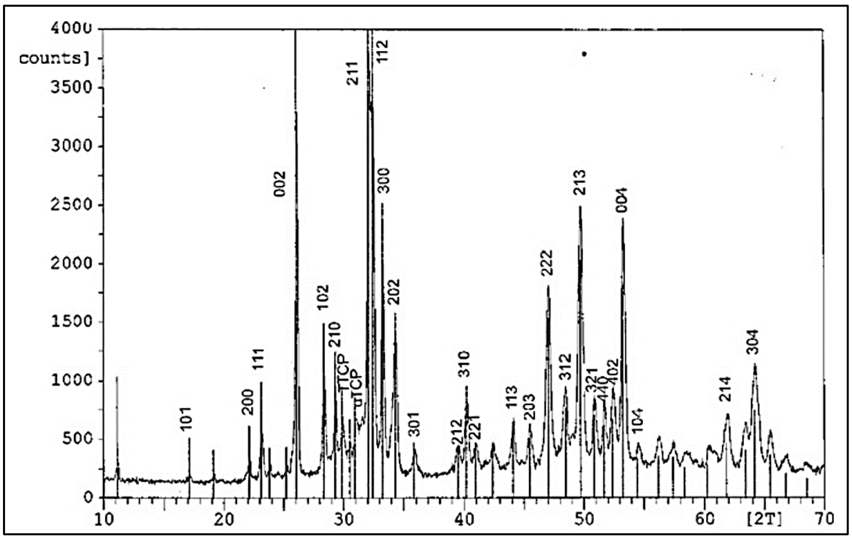

Fig.5. - XRD pattern of the composite coating on SS-316L with HAP/Ta [87]

Figure 6 displays the potentiodynamic polarisation curves of the SS in the normal saline solution with and without the HAP/Ta composite coating. Figure 7 demonstrates the parallel curves that Ringer's solution produced. Since the retrieved data from these curves were the closest to the average magnitude of the present densities of every set of samples, they were chosen. The corrosion current density of HAP/Ta coated SS-316L in Ringer's, and normal saline solutions are reduced due to the HAP/Ta coating's good impact on the metal substrate's resistance to corrosion. Additionally, it can be demonstrated that the uncoated SS-316L has a lower potential for pitting corrosion than the HAP/Ta coated SS-316L [curves (a) and (b), respectively]; this suggests that the corrosion will be inhibited at a certain potential by utilizing the HAP/Ta coating. As a result, utilizing the innovative HAP/Ta coating would lower the current density of corrosion and increase the propensity for pitting corrosion compared to SS-316L that is not coated. The innovative HAP/Ta coating's greater pitting corrosion potential demonstrates that it is efficient at preventing corrosion[87].

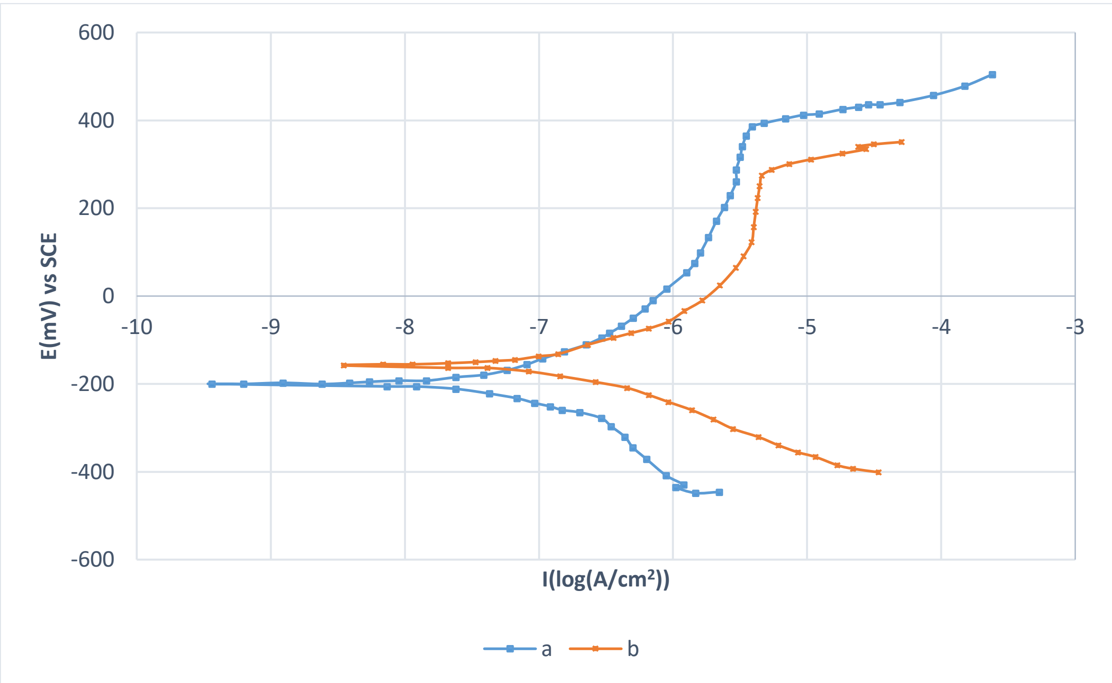

Fig. 6. - Polarization curve: (a) uncoated SS-316L,(b) coated by HAP/Ta in normal saline solution (0.9 wt.% NaCl) [87]

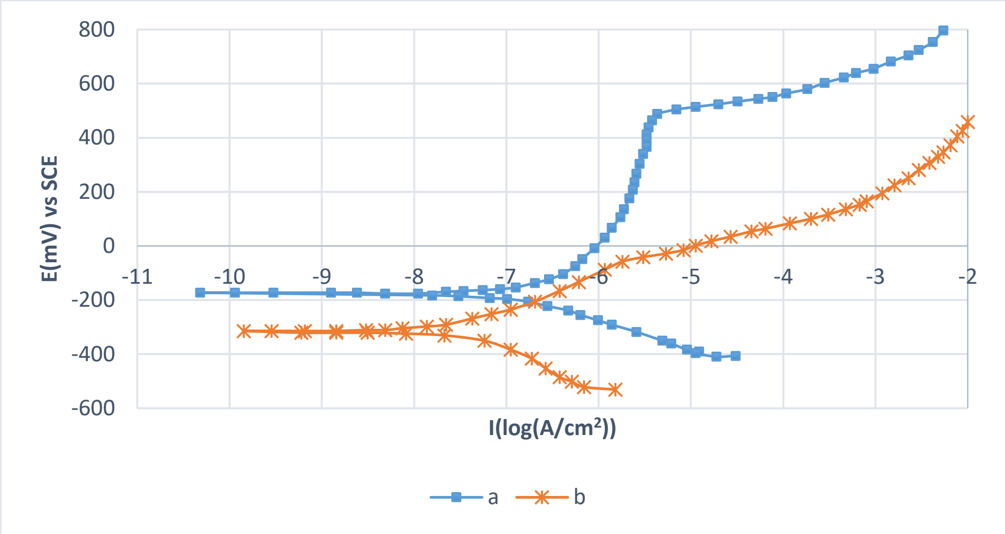

Fig. 7. - Polarization curve: (a) uncoated SS-316L,(b) coated by HAP/Ta in Ringer's solution [87]

Gnanavel et al. [88] utilized the pulsed laser deposition approach to deposit hydroxyapatite (HAP) ceramics on Ti-6Al-4V and SS-316L. XRD, scanning electron microscopy with energy-dispersive spectroscopy (EDS), and atomic microscopy were utilized to evaluate the coated thin film. Correction investigations on uncoated and coated samples were conducted utilizing potentiodynamic polarisation tests in a simulated bodily fluid (Hanks' solution). Their bioactivity was assessed by submerging the HAP-coated specimens in Ti-6Al-4V and SS-316L for nine days in simulated bodily fluid. The existence of HAP was verified by XRD and EDS investigations. According to the corrosion investigations, treated specimens exhibit excellent resistance to corrosion than substrates made of SS-316L and Ti-6Al-4V. The HAP-coated substrate bioactivity was indicated by the development of apatite on treated specimens. Ti-6Al-4V substrates with HAP coating provide greater corrosion resistance than those made of SS-316L.

The XRD pattern's crystalline phase of Ti-6Al-4V and SS-316L has been examined. CuK radiation ($\lambda = 0.1548$ nm) has been utilized, and the specimens have been scanned at a rate of 0.5°/min from 20° to 70°. XRD analysis was utilized to analyze the phases that developed on the surfaces of HAP-coated Ti-6Al-4V and SS-316L, and the results are demonstrated in Fig. 8. The SS-316L with calcium phosphate (Ca/P) XRD forms are consistent with JCPDS#00-003-0429. Calcium phosphate is present, as demonstrated by the peaks at 27.02°, 20.38°, 24.33°, and 39.39°. Furthermore, the XRD pattern of the Ti-6Al-4V of Ca/P are consistent with JCPDS#01-086-1585. The peaks at 44.25°, 45.21°, 48.63°, and 60.20° demonstrate that calcium phosphate is present. The coating contains calcium phosphate, which resembles the composition of bone and has the extra benefit of promoting osseointegration.

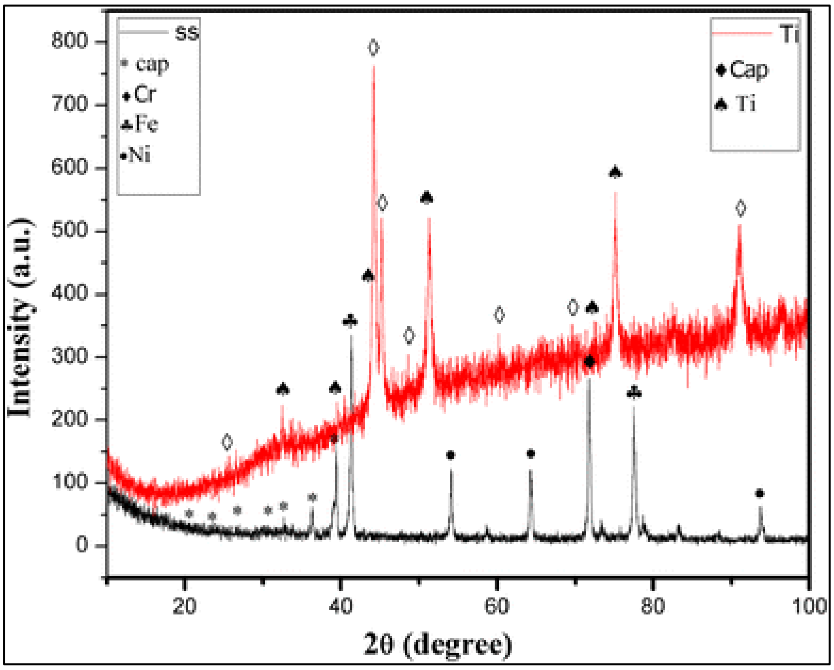

Fig.8. - XRD pattern of Ti–6Al–4V alloy and SS-316L coated by HAP [88]

In Hanks' solution (pH ranges from 7.2 to 7.6), the potentiodynamic polarisation curves of the material and HAP-coated specimens (Ti-6Al-4V and SS-316L) are demonstrated. On specimens coated with SS-316L and Ti-6Al-4V, the Ecorr magnitudes changed to a more favorable magnitude. This finding concludes that, once compared to HAP-coated SS-316L, Ti-6Al-4V alloys have greater resistance to corrosion [89]. These findings demonstrated that the HAP-coated Ti-6Al-4V combination outperforms the SS-316L in corrosion resistance (Figure 9).

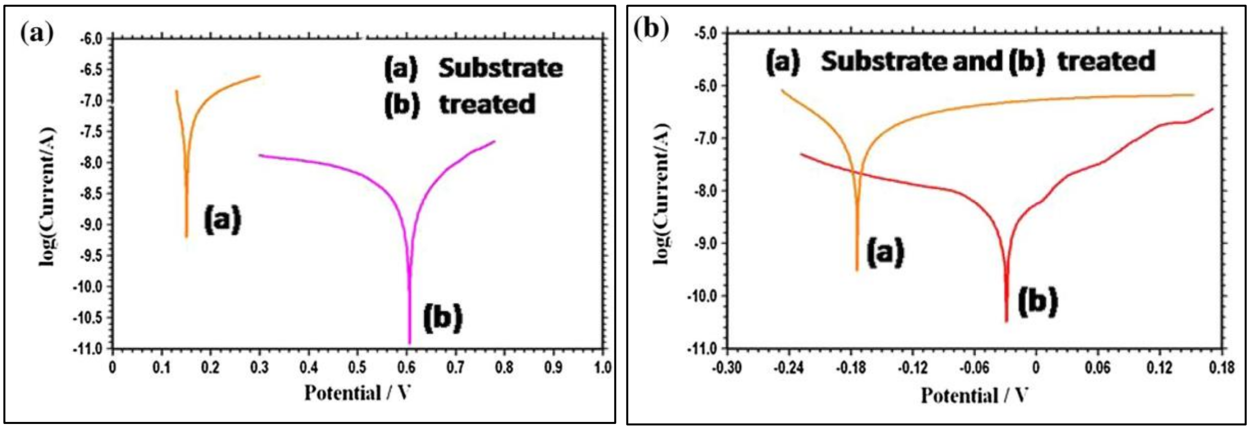

Fig. 9. - Potentiodynamic polarisation a) SS-316L, b) Ti–6Al–4V substrate before and after treatment by HAP [89]

Conclusion

Except for the calcium carbonate otoconia of the inner ear, HAP represents the chemical counterpart of biogenic apatite, the main constituent of all hard tissues in the human body because of the great degree of crystallographic and chemical similarity between the inorganic component of teeth and bone. It drew attention to itself in the early stages of biomaterials science due to the biocompatibility predicted from this similarity. Additionally, HAP has a benefit over biocompatible but bioinert ceramics like titania, alumina, and silica because of its bioactivity, which enables it to interact more closely with the cells and tissues in the biological environment. Additionally, several very straightforward synthesis techniques for HAP were developed, enabling the researchers to create particles with precisely defined shapes and sizes. Moreover, utilizing the powerful physisorption capacity of the polyvalent ions that make up the surface of the HAP particle, functionalization and surface modification of HAP may be accomplished by similarly straightforward, noncovalent interactions.

Thanks to all these benefits, HAP is a good option for various biomedical applications in tissue engineering, medical implants, medication delivery, gene therapy, and bioimaging. Although utilizing HAP has many advantages, there are certain drawbacks and side effects that must be carefully considered before a particular application is chosen. For instance, HAP particles' osteoconductivity is necessary for tissue engineering scaffolds and medical implants, yet this property is insufficient to provide a useful and effective tissue replacement. In certain tissues, it is necessary to create prostheses and scaffolds that can withstand high loads and cyclic stresses. To get around this problem, HAP must be combined with polymers or other kinds of nanoparticles to improve its brittleness and poor fracture toughness. Most of the suggested solutions are still in the research stage, and the consensus is that additional study is necessary before the therapeutic objectives are reached.

Acknowledgments

This work was supported by Al-Mustaqbal University (grant number MUC-E-0122).

Reference

[1] Redford D. B. From slave to pharaoh: the black experience of ancient Egypt. JHU Press, 2004.

[2] Rasouli R., Barhoum A., Uludag H. A review of nanostructured surfaces and materials for dental implants: surface coating, patterning and functionalization for improved performance // Biomater. Sci., vol. 6, no. 6, 2018, P. 1312–1338

[3] Al-khafaji Z. S., Radhi N. S., Mohson S. A. Preparation and modelling of composite materials (polyester-alumina) as implant in human body // Int. J. Mech. Eng. Technol., vol. 9, no. 4, 2018, P. 468–478

[4] Guillaume B. Dental implants: A review //Morphologie, vol. 100, no. 331, 2016, P. 189–198

[5] Manivasagam G., Dhinasekaran D., Rajamanickam A. Biomedical implants: corrosion and its prevention-a review // Recent patents Corros. Sci., vol. 2, no. 1, 2010

[6] Spilsbury K., Nelson A., Cullum N., Iglesias C., Nixon J., Mason S. Pressure ulcers and their treatment and effects on quality of life: hospital inpatient perspectives //J. Adv. Nurs., vol. 57, no. 5, 2007, P. 494–504

[7] Anderson J., Neary F., Pickstone J. Surgeons, manufacturers and patients: A transatlantic history of total hip replacement. Springer, 2007.

[8] Radhi N. S., Sahi N. M., Al-Khafaji Z. Investigation Mechanical and Biological Properties of Hybrid PMMA Composite Materials as Prosthesis Complete Denture //Egypt. J. Chem., 2022

[9] Rahaman M. N., Brown R. F. Materials for Biomedical Engineering: Fundamentals and Applications. John Wiley & Sons, 2021.

[10] Abed Janabi Z. M., Jaber Alsalami H. S., Al-Khafaji Z. S., Hussien S. A. Increasing of the corrosion resistance by preparing the trivalent nickel complex //Egypt. J. Chem., 2021
[11] Rajih A. K., Ahmed J. K., Radhi N. S. Investigation some properties of (Zn-Ni-SiC) composites coating on low carbon steel //IRAQI J. Mech. Mater. Eng., vol. 18, no. 2, P. 363–374
[12] Al-Zubaidy B., Radhi N. S., Al-Khafaji Z. S. Study the effect of thermal impact on the modelling of (titanium-titania) functionally graded materials by using finite element analysis //Int. J. Mech. Eng. Technol., no. 1, 2019.
[13] Sattar S. et al. Corrosion reduction in steam turbine blades using nano-composite coating // J. King Saud Univ., vol. 35, no. 8, 2023, P. 102861
[14] Sattar S., Alaiwi Y., Radhi N. S., Al-khafaji Z. Numerical Simulation for Effect of Composite Coating (TiO_2 + SiO_2) Thickness on Steam Turbine Blades Thermal and Stress Distribution //Acad. J. Manuf. Eng., vol. 21, no. 4, 2023.
[15] Krishnakumar S., Senthilvelan T. Polymer composites in dentistry and orthopedic applications-a review // Mater. Today Proc., vol. 46, 2021, P. 9707–9713,
[16] Al-Khafaji Z. S., Falah M. W. Applications of high density concrete in preventing the impact of radiation on human health //J. Adv. Res. Dyn. Control Syst., vol. 12, no. 1 Special Issue, 2020
[17] Raut H. K., Das R., Liu Z., Liu X., Ramakrishna S. Biocompatibility of biomaterials for tissue regeneration or replacement," Biotechnol. J., vol. 15, no. 12, 2020, P. 2000160
[18] Pires A. L. R., Bierhalz A. C. K., Moraes A. M. Biomaterials: types, applications, and market //Quim. Nova, vol. 38, 2015 ,P. 957–971
[19] Radhi N. S., Al-Khafaji Z. S. Preparation and Investigation composite coating (Ni-nano hydroxyapatite) on low carbon steel samples // 6th International Scientific Conference on Nanotechnology, Advanced Materials and its Applications, 2018
[20] Hussain A. J., Al-khafaji Z. S., Hamza W. A. An Investigation into the Distribution of Internal Residual Stresses of Aluminum Plate Subjected to Thermal Load by Using Hole Drilling Technique //J. Mech. Eng. Res. Dev., vol. 44, no. 5, 2021, P. 402–411,
[21] Abed K. M., Radhi N. S., Jasim A. H., Al-Khafaji Z. S., Radhi S., Hussien S. A. Study the effect of adding zirconia particles to nickel–phosphorus electroless coatings as product innovation on stainless steel substrate //Open Eng., vol. 12, no. 1, 2022, P. 1038–1045
[22] Jasim A. H., Joudi W. M., Radhi N. S., Saud A. N. Mechanical properties and wear characteristic of (Aluminum-Zinc Oxide) metal matrix composite prepared using stir casting process //Materials science forum, Trans Tech Publ, 2020, P. 175–184.
[23] Zhou H., Lee J. Nanoscale hydroxyapatite particles for bone tissue engineering /Acta Biomater., vol. 7, no. 7, 2011, P. 2769–2781
[24] Radhi N. S. Preparation, characterization, and modeling functionally graded materials in bio-application // PhD thesis. University of Technology. Iraq, 2015.
[25] Bhawe A. K. and et al. Static structural analysis of the effect of change in femoral head sizes used in Total Hip Arthroplasty using finite element method //Cogent Eng., vol. 9, no. 1, 2022, P. 2027080
[26] Kadhim I. A. U., Sallal H. A., Al-Khafaji Z. S.A Review in Investigation of Marine Biopolymer (Chitosan) for Bioapplications //ES Mater. Manuf., vol. 21, 2023
[27] Sallal H. A., Radhi M. S., Mahboba M. H., Al-Khafaji Z. Impact of embedded sol-gel synthesized triple composites on polymer's mechanical properties //Egypt. J. Chem., 2022
[28] Al-khafaji Z. S., Radhi N. S., Mohson S. A. Preparation and modelling of composite materials (polyester-alumina) as implant in human body //Int. J. Mech. Eng. Technol., vol. 9, no. 4, 2018.
[29] Radhi N. S., Al-Khafaji Z., Mareai B. M., Radhi S., Alsaegh A. M. Reducing oil pipes corrosion by (zn-ni) alloy coating on low carbon steel substrate by sustainable process //J. Eng. Sci. Technol., vol. 18, no. 3, 2023, P. 1624–1638
[30] Radhi S. S., Al-Khafaji Z. S., Falah M. W. Sustainable heating system by infrared radiators, vol. 4, no. 1, P. 42–52, 2022
[31] Radhi N. S., Jamal Al-deen H. H., Safaa Hadi R., Al-Ghaban Nada, Al-Khafaji Z. S. Preparation and investigation a hydroxyapatite layer coating on titanium substrate for surgical implants //J. Nanostructures, 2023, [Online]
[32] Radhi N. S., Al-Khafaji Z. Investigation biomedical corrosion of implant alloys in physiological environment //Int. J. Mech. Prod. Eng. Res. Dev., vol. 8, no. 4, 2018
[33] Dawood N. M., Radhi N. S., Al-Khafaji Z. S. Investigation Corrosion and Wear Behavior of Nickel-Nano Silicon Carbide on Stainless Steel 316L," vol. 1002, P. 33–43, 2020
[34] Saini M., Singh Y., Arora P., Arora V., Jain K. Implant biomaterials: A comprehensive review //World J. Clin. Cases WJCC, vol. 3, no. 1, 2015, P. 52,
[35] Radhi N. S., Marza M., Al-Khafaji Z. S. Modification of Nickel-phosphor Electroless Coatings by adding particles of Zirconia //Solid State Technol., vol. 63, no. 2, 2020.
[36] Mears S. C., Kates S. L. A guide to improving the care of patients with fragility fractures, edition 2," Geriatr. Orthop. Surg. Rehabil., vol. 6, no. 2, 2015, P. 58–120
[37] ZhaoD W. Current status on clinical applications of magnesium-based orthopaedic implants: A review from clinical translational perspective," Biomaterials, vol. 112, 2016, P. 287–302
[38] Park J. B., Bronzino J. D. Biomaterials: principles and applications. Crc press, 2002.
[39] Bowen P. K. et al. Biodegradable metals for cardiovascular stents: from clinical concerns to recent Zn-Alloys //Adv. Healthc. Mater., vol. 5, no. 10, 2016, P. 1121–1140
[40] Paxton N. C., Powell S. K., Woodruff M. A. Biofabrication: The future of regenerative medicine //Tech. Orthop., vol. 31, no. 3, 2016, P. 190–203
[41] Fahad N. D., Radhi N. S., Al-Khafaji Z. S., Diwan A. A. Surface modification of hybrid composite multilayers spin cold spraying for biomedical duplex stainless steel //Heliyon, 2023
[42] Vaithilingam J., Kilsby S., Goodridge R. D., Christie S. D. R., Edmondson S., Hague R. J. M. Functionalisation of Ti6Al4V components fabricated using selective laser melting with a bioactive compound //Mater. Sci. Eng. C, vol. 46, P. 52–61, 2015
[43] Radhi N., Hafiz M., Atiyah A. Preparation and investigation of corrosion and biocompatibility properties for functionally graded materials (NiTi) //Ind Eng Manag. S, vol. 3, 2018, P. 316–2169

[44] Jabor M., Radh N. S., Al-Kinani M. A., Al-Khafaji Z. S. Optimization of Electro less of Nickel base coating for Cermet Cutting Tools Substrate //J. Mech. Eng. Res. Dev., vol. 44, no. 3, 2021, P. 30–40

[45] Heiden M., Walker E., Stanciu L. Magnesium, iron and zinc alloys, the trifecta of bioresorbable orthopaedic and vascular implantation-a review //J. Biotechnol. Biomater., vol. 5, no. 2, 2015, P. 1

[46] Eliaz N. Corrosion of metallic biomaterials: A review //Materials (Basel)., vol. 12, no. 3, 2019

[47] Wang H., Mooney D. J. Biomaterial-assisted targeted modulation of immune cells in cancer treatment //Nat. Mater., vol. 17, no. 9, 2018, P. 761–772,

[48] Chen F. et al. Nanobiomaterial-based vaccination immunotherapy of cancer //Biomaterials, vol. 270, 2021, P. 120709

[49] Radhi N. S. Using Hydroxyapatite Powder (HAP) in Coating of Stainless-Steel Substrate for Bio-appliation (A Review) //RAQI J. Mech. Mater. Eng., vol. 19, no. 2, 2019, P. 173–182

[50] Neacsu I. A., Stoica A. E., Vasile B. S., Andronescu E. Luminescent hydroxyapatite doped with rare earth elements for biomedical applications //Nanomaterials, vol. 9, no. 2, 2019, P. 239,

[51] Radhi N. S. Preparation And Modeling (Titanium-Hydroxyapatite) Functionally Graded Materials For Bio-Medical Application //Int. J. Civ. Eng. Technol., vol. 9, no. 6, 2018, P. 28–39,

[52] Pividal P. Carrasco Surface functionalization of titanium with antifouling and inhibition of bacterial adhesion treatment in the human body //Universitat Politècnica de Catalunya, 2015. [Online]

[53] Kutzner K. P., Freitag T., Bieger R. Defining 'undersizing'in short-stem total hip arthroplasty: the importance of sufficient contact with the lateral femoral cortex //Hip Int., vol. 32, no. 2, 2022, P. 160–165

[54] Hadi R. S., Al-Deen H. H. J., Radhi N. S. Investigation the Coating of Hydroxyapatite on Titanium Substrate by Pulse Laser Deposition //J. Univ. Babylon Eng. Sci., vol. 26, no. 10, 2018, P. 299–311

[55] Galindo T. G. P., Chai Y., Tagaya M. Hydroxyapatite nanoparticle coating on polymer for constructing effective biointeractive interfaces //J. Nanomater., vol. 2019

[56] Boilet L. et al. Processing and properties of transparent hydroxyapatite and β tricalcium phosphate obtained by HIP process //Ceram. Int., vol. 39, no. 1, 2013, P. 283–288

[57] Dubok V. A. Bioceramics-yesterday, today, tomorrow //Powder Metall. Met. Ceram., vol. 39, P. 381–394, 2000

[58] Weiner S., Wagner H. D. The material bone: structure-mechanical function relations //Annu. Rev. Mater. Sci., vol. 28, no. 1, 1998, P. 271–298,

[59] Hench L. L., Thompson I. Twenty-first century challenges for biomaterials //J. R. Soc. Interface, vol. 7, no. suppl_4, 2010, pp. S379–S391,

[60] Dorozhkin S. V. Calcium orthophosphates in nature, biology and medicine," Materials (Basel)., vol. 2, no. 2, 2009, P. 399–498

[61] LeGeros R. Z. Calcium phosphate-based osteoinductive materials //Chem. Rev., vol. 108, no. 11, 2008, P. 4742–4753

[62] Ohgushi H., Dohi Y., Tamai S., Tabata S. Osteogenic differentiation of marrow stromal stem cells in porous hydroxyapatite ceramics //J. Biomed. Mater. Res., vol. 27, no. 11, 1993, P. 1401–1407

[63] Beachley V., Wen X. Polymer nanofibrous structures: Fabrication, biofunctionalization, and cell interactions," Prog. Polym. Sci., vol. 35, no. 7, 2010, P. 868–892

[64] Gupta D., Venugopal J., Mitra S., Dev V. R. G., Ramakrishna S. Nanostructured biocomposite substrates by electrospinning and electrospraying for the mineralization of osteoblasts //Biomaterials, vol. 30, no. 11, 2009, P. 2085–2094

[65] Han Y., Wang X., Li S. A simple route to prepare stable hydroxyapatite nanoparticles suspension // J. Nanoparticle Res., vol. 11, 2009, P. 1235–1240

[66] Lane N. E., Wallace D. J. All about Osteoarthritis: The definitive resource for arthritis patients and their families. Oxford University Press, 2002.

[67] Freire V., Moser T. P., Lepage-Saucier M. Radiological identification and analysis of soft tissue musculoskeletal calcifications," Insights Imaging, vol. 9, 2018, P 477–492

[68] Mohseni E., Zalnezhad E., Bushroa A. R. Comparative investigation on the adhesion of hydroxyapatite coating on Ti–6Al–4V implant: A review paper //Int. J. Adhes. Adhes., vol. 48, 2014, P. 238–257

[69] Lacefield W. R. Hydroxyapatite coatings //Ann. N. Y. Acad. Sci., vol. 523, 1988, P. 72–80

[70] Mahapatro A. Bio-functional nano-coatings on metallic biomaterials //Mater. Sci. Eng. C, vol. 55, 2015, P. 227–251

[71] Bakar M. S. A. et al. Tensile properties, tension–tension fatigue and biological response of polyetheretherketone–hydroxyapatite composites for load-bearing orthopedic implants //Biomaterials, vol. 24, no. 13, 2003, P. 2245–2250, 2003

[72] Loo S. C. J., Siew Y. E., Ho S., Boey F. Y. C., Ma J. Synthesis and hydrothermal treatment of nanostructured hydroxyapatite of controllable sizes //J. Mater. Sci. Mater. Med., vol. 19, 2008, P. 1389–1397, 2008

[73] Chaudhuri B., Mondal B., Modak D. K., Pramanik K., Chaudhuri B. K. Preparation and characterization of nanocrystalline hydroxyapatite from egg shell and K_2HPO_4 solution //Mater. Lett., vol. 97, 2013, P. 148–150, 2013

[74] Swain S. K., Dorozhkin S. V., Sarkar D. Synthesis and dispersion of hydroxyapatite nanopowders //Mater. Sci. Eng. C, vol. 32, no. 5, 2012, P. 1237–1240

[75] Shah A. T., Zahoor M., Muhammad N., Kamutzki F., Schmidt J., Görke O. Rapid wet chemical synthesis of bioactive glass with high yield by probe sonication //J. Mater. Chem. B, 2023

[76] Soltani T., Entezari M. H. Sono-synthesis of bismuth ferrite nanoparticles with high photocatalytic activity in degradation of Rhodamine B under solar light irradiation //Chem. Eng. J., vol. 223, 2013, P. 145–154,

[77] Panda S., Biswas C. K., Paul S. A comprehensive review on the preparation and application of calcium hydroxyapatite: A special focus on atomic doping methods for bone tissue engineering //Ceram. Int., vol. 47, no. 20, 2021, P. 28122–28144,

[78] Kim D. W. et al. Simple large-scale synthesis of hydroxyapatite nanoparticles: in situ observation of crystallization process," Langmuir, vol. 26, no. 1, 2010, P. 384–388,

[79] Fihri A., Len C., Varma R. S., Solhy A. Hydroxyapatite: A review of syntheses, structure and applications in heterogeneous catalysis," Coord. Chem. Rev., vol. 347, 2017, P. 48–76,

[80] Haider A., Haider S., Han S. S., Kang I.-K. Recent advances in the synthesis, functionalization and biomedical applications of hydroxyapatite: a review //Rsc Adv., vol. 7, no. 13, 2017, P. 7442–7458

[81] Ong J. L., Chan D. C. N. Hydroxyapatite and their use as coatings in dental implants: a review //Crit. Rev. Biomed. Eng.,

vol. 28, no. 5&6, 2000
[82] Chocholata P., Kulda V., Babuska V. Fabrication of scaffolds for bone-tissue regeneration //Materials (Basel)., vol. 12, no. 4, 2019, P. 568
[83] Nithya R., Sundaram N. M. Biodegradation and cytotoxicity of ciprofloxacin-loaded hydroxyapatite-polycaprolactone nanocomposite film for sustainable bone implants, //Int. J. Nanomedicine, vol. 10, no. Suppl 1, 2015, P. 119
[84] Du M., Chen J., Liu K., Xing H., Song C. Recent advances in biomedical engineering of nano-hydroxyapatite including dentistry, cancer treatment and bone repair //Compos. Part B Eng., vol. 215, 2021, P. 108790
[85] Pompe W. et al. Functionally graded materials for biomedical applications //Mater. Sci. Eng. A, vol. 362, no. 1–2, 2003, P. 40–60
[86] Tiberghien P. Use of suicide genes in gene therapy //J. Leukoc. Biol., vol. 56, no. 2, 1994, P. 203–209
[87] Fathi M. H., Azam F. Novel hydroxyapatite/tantalum surface coating for metallic dental implant," Mater. Lett., vol. 61, no. 4–5, 2007, P. 1238–1241
[88] Gnanavel S., Ponnusamy S., Mohan L., Muthamizhchelvan C. In vitro corrosion behaviour of Ti–6Al–4V and 316L stainless steel alloys for biomedical implant applications //J. Bio-and Tribo-Corrosion, vol. 4, no. 1, 2018, P. 1–8
[89] Anandan C., Mohan L. In vitro corrosion behavior and apatite growth of oxygen plasma ion implanted titanium alloy β-21S //J. Mater. Eng. Perform., vol. 22, no. 11, 2013, P. 3507–3516

Information of the authors

Al-Khafaji Zainab, PhD, lecturer, Universiti Kebangsaan Malaysia, Scientific Research Center, Al-Ayen University, Thi-Qar, Iraq
e-mail: p123005@siswa.ukm.edu.my

Kazem Mustafa, msc., assistant lecturer, Al-Zahraa University for women
e-mail: mustafa.abdhussein@alzahraa.edu.iq

Radhi Nabaa, PhD, professor, University of Babylon/ Materials Engineering College/ Babil. Babylon
e-mail: mat.nabaa.sattar@uobabylon.edu.iq

Falah Mayadah, PhD, Asst.professor, College of Engineering and Engineering Techniques, AL-Mustaqbal University
e-mail: mayadah.waheed@uomus.edu.iq

Hadi Zainab, msc., asst. lecturer, University of Babylon chemistry sciences
e-mail: modetena35@gmail.com

DOI 10.52209/2706-977X_2024_2_79 **IRSTI 55.03.14** **UDC 621.396**

Weight Reduction of a Speed Reducer using Modified Particle Swarm Optimization and Shuffled Frog Leaping Algorithm

Dalavi A.*, Gomes A., Husain A.
Symbiosis Institute of Technology, Pune, India
*corresponding author

Abstract. Gear drives are extremely critical elements of transmission systems. Designing gears that satisfy the application's requirements like load carrying capacity and strength whilst also being compact, lightweight, and economical is quite a challenging task. In recent times, a lot of research has been dedicated to optimizing speed reducers by making use of metaheuristic nature-inspired algorithms. The present work optimizes the weight of a spur speed reducer by employing two modified nature-inspired algorithms: Particle Swarm Optimization (PSO) and Shuffled Frog Leaping Algorithm (SFLA). Parameter optimization was carried out to select the best combination of c_1, c_2 and ω for the selected case study. It was found that there was a 1.1619% and 13.41% decrease in the cost function evaluation, as compared to the Crude Monte-Carlo and Stray Process methods used in the original case study, and around an 11% decrease as compared to results in published literature.

Keywords: gearbox optimization, particle swarm optimization, shuffled frog leaping algorithm, parameter optimization, spur gear.

Introduction

Gears are extremely critical elements in mechanical systems and are typically used for short-distance power transmission between elements having different torque and speeds. Gears have been employed in a wide range of applications, including automobiles, aircraft, wind turbines, and industrial machines, among others. Designing gears with the least possible amount of volume is critical because it reduces energy consumption and the amount of material required to manufacture them [1]. Over the years, there have been great advances in research for achieving dimensional optimality while also preventing failure. Further, the ever-growing environmental concerns have led to the need for high efficiency of the designed product. As a result, design optimization is often regarded as the most crucial step in the design and development of a new gearbox [2].

Nature-inspired optimization techniques were introduced over half a century ago and have hence been used to optimize engineering problems using the myriad of algorithms developed. The most implemented algorithms for design problems include Genetic Algorithm (GA), Simulated Annealing (SA), Particle Swarm Optimization (PSO), and their variants [3]. In this paper, gear data from a previously investigated case of a spur reducer proposed by Dr Jan Golinski was considered [4]. The Golinski speed reducer problem is also a part of the NASA Langley Multidisciplinary Design Optimization (MDO) Test Suite [5]. Over the years, this case study has been extensively attempted using various optimization algorithms, both deterministic and metaheuristic. Modified versions of the PSO and SFLA algorithms were implemented on the reduced set of equations provided by [6]. The results obtained were then compared with those presented in previously published works.

2 Materials and Methods

2.1 Modified Particle Swarm Optimization Algorithm

The particle swarm optimization algorithm, a meta heuristic algorithm for optimising non-linear continuous functions [7]. It is based on the social behavior of swarm animals like birds and fish and depends on factors such as avoiding predators, seeking food, and environmental parameters like temperature, etc. The collective knowledge gathered and shared by the swarm members is known as social knowledge which is an integral part of the practice followed by these swarms to ensure their survival. The end goal is to find a spot that will maximise their survival advantage along with the food they are seeking. To achieve this, each member explores and judges using several criteria.

The PSO algorithm simulates this swarm behaviour, wherein the position and velocity vectors are given by X_i and V_i respectively, and n is the total number of variables in the problem. Soon after PSO was introduced, [8] proposed a modified version with a new parameter called inertia weight (ω), which greatly improved its performance by balancing out the local and global search of the algorithm. A larger ω tends to improve the global search, while a smaller ω tends to improve the local search. This modified PSO (with the inertia weight included) is considered as the canonical PSO. This was further modified to include limits for the minimum (Min V) and maximum (Max V) velocity [9].

Initially, the population is randomly generated within the specified ranges for each variable and V_i is set to 0. Then the cost function *f(X)* is calculated, and the initial positions of the population is set as the personal best for each particle. The position with the least *f(X)* value is set as the global best. Then the maximum and minimum allowed velocity limits are calculated using equations (1) and (2) and the velocity limits are applied as per equations (3) and (4):

$$Max\,V = 0.2(VarMax - VarMin) \tag{1}$$

$$Min\,V = -Max\,V \tag{2}$$

$$V_i = \max(V_i,\ Min\,V) \tag{3}$$

$$V_i = \min(V_i,\ Max\,V) \tag{4}$$

Then the algorithm proceeds by generating the new set of positions for the particles. For this, the velocity of the particle is calculated using equation (5) and is constrained as per equations (6) and (7):

$$V_{i+1} = \omega V_i + c_1 r_1\left(p_{best,i} - X_i\right) + c_2 r_2\left(g_{best,i} - X_i\right) \tag{5}$$

$$X_i = \max(X_i,\ VarMin) \tag{6}$$
$$X_i = \max(X_i,\ VarMax) \tag{7}$$

Where, $p_{best,i}$ = best personal particle position, $g_{best,i}$ = global best particle position, c_1 and c_2 = acceleration constants used to regulate the cognitive and social elements respectively, r_1 and r_2 = randomly generated numbers between 0 and 1 (to avoid early convergence).

The first term in equation (5) represents the particle's preceding velocity, the second term is the difference between the particle's own best position (cognitive term), and the third term oversees the process of sharing knowledge between particles (social term). This ensures that the best position is found regardless of which particle finds it. Then the new positions for the population are determined using equation (8) and the cost function is evaluated:

$$X_{i=1} = X_i + V_{i+1} \tag{8}$$

For any given particle, if the cost function evaluation for the new position is better than the previous one, the personal best is updated and set to the new position. Similarly, if the new cost function evaluation is better than the global best, this particle position is set as the new global best position. This procedure is repeated till the convergence criteria is met. The flowchart of the modified PSO algorithm used in this paper is shown in Figure 1.

2.2 Modified Shuffled Frog Leaping Algorithm

The Shuffled Frog Leaping Algorithm (SFLA) is a memetic metaheuristic method that seeks the global optimum of an optimization problem [10]. It is based on the concept of frogs leaping across stones in a swamp, wherein the frogs represent the population, which in turn represents feasible solutions to the optimization problem. The stones are at discrete locations in the swamp and have varying amounts of food on them. The frogs try to locate the stone that has the largest amount of food available as quickly as possible. They do this by improving their memes, which correspond to their coordinate position, and can only be altered by discrete values. The population is further subdivided into subsets called memeplexes, within which the frogs share information with each another and improve their memes. Based on this, the frog's leaping step size is adjusted, thus changing their positions. SFLA combines the local search methodology of PSO and the competitive nature and mixed information methodology of the Shuffled Complex Evolution (SCE) algorithm.

Initially the frog population X_i is randomly generated containing *n* number of frogs. Then the cost function is evaluated and the frogs in the population are arranged in descending order of the results obtained. Next, the population is divided into m number of memeplexes. The first frog will be sorted into the 1st memeplex, the second frog in the 2nd memeplex, …., the m^{th} frog to the m^{th} memeplex, the $(m+1)^{th}$ frog to the 1st memeplex, and so on. Then the worst (X_w) and best (X_b) frogs within each memeplex, and the global best frog (X_g) from the entire population are identified.

To avoid early convergence at a local optimum, [11] suggested the use of a parameter called the 'search acceleration factor', denoted by c, which is used in the modified SFLA algorithm. At the beginning of the search, a larger c value would accelerate the global search, thus widening the search space. Once a probable optimal location is identified, c would focus on an in-depth local search. Hence, c balances the local and global search of the algorithm. [12] suggested the use of an inertia factor ω, similar to the inertia factor in PSO. The inertia factor in SFLA would help avoid premature convergence and widen the search space.

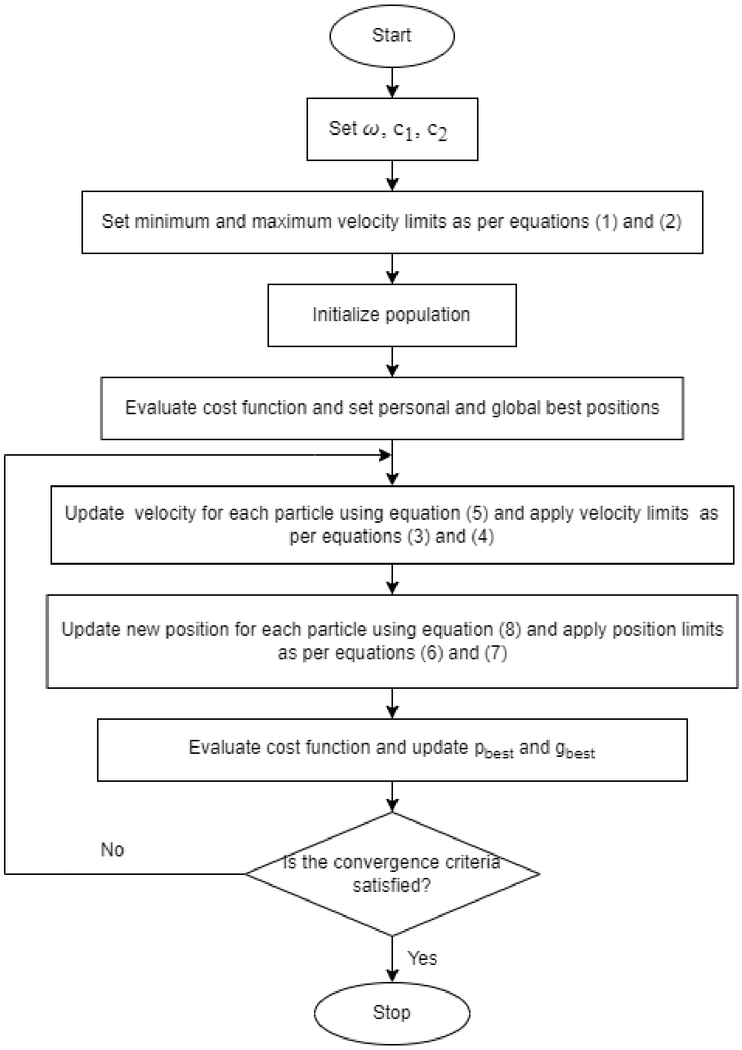

Fig. 1. - Flowchart for modified PSO algorithm

Now, the local search step is initiated using equation (9), by which the new position (X_{i+1}) of the frog is calculated. Every new frog generated is subject to the position range conformance criteria mentioned in equation (11) [13]. If this condition is satisfied, the cost function is evaluated, and if the evaluation is better, the new frog replaces the worst one. If not, the local search evaluation is skipped and the global search step is initiated using equation (10), by which the new position (X_{i+1}) is generated. Once again, the condition in equation (11) is checked. If satisfied, the cost function is evaluated, and if the evaluation is better, the new frog replaces the worst one. If equation (11) is not satisfied again, the global search step is skipped, and the frog is generated randomly.

$$X_{i+1} = \omega X_i + c_1 r(X_b - X_w) \tag{9}$$

$$X_{i+1} = \omega X_i + c_2 r\left(X_g - X_w\right) \tag{10}$$

$$all(x \geq VarMin) \quad \text{AND} \quad all(x \leq VarMax) \tag{11}$$

Where, X_{i+1} = new position, X_i = previous frog position, r = randomly generated number between 0 and 1.

This conditional procedure reduces the number of unnecessary cost function evaluations, thus speeding up the algorithm. The local / global search steps are repeated a set number of times, following which, the memeplexes are shuffled for meme (information) exchange at the global level. This sequence is repeated till convergence is achieved. An overview of the Modified SFLA algorithm is given in Figure 2.

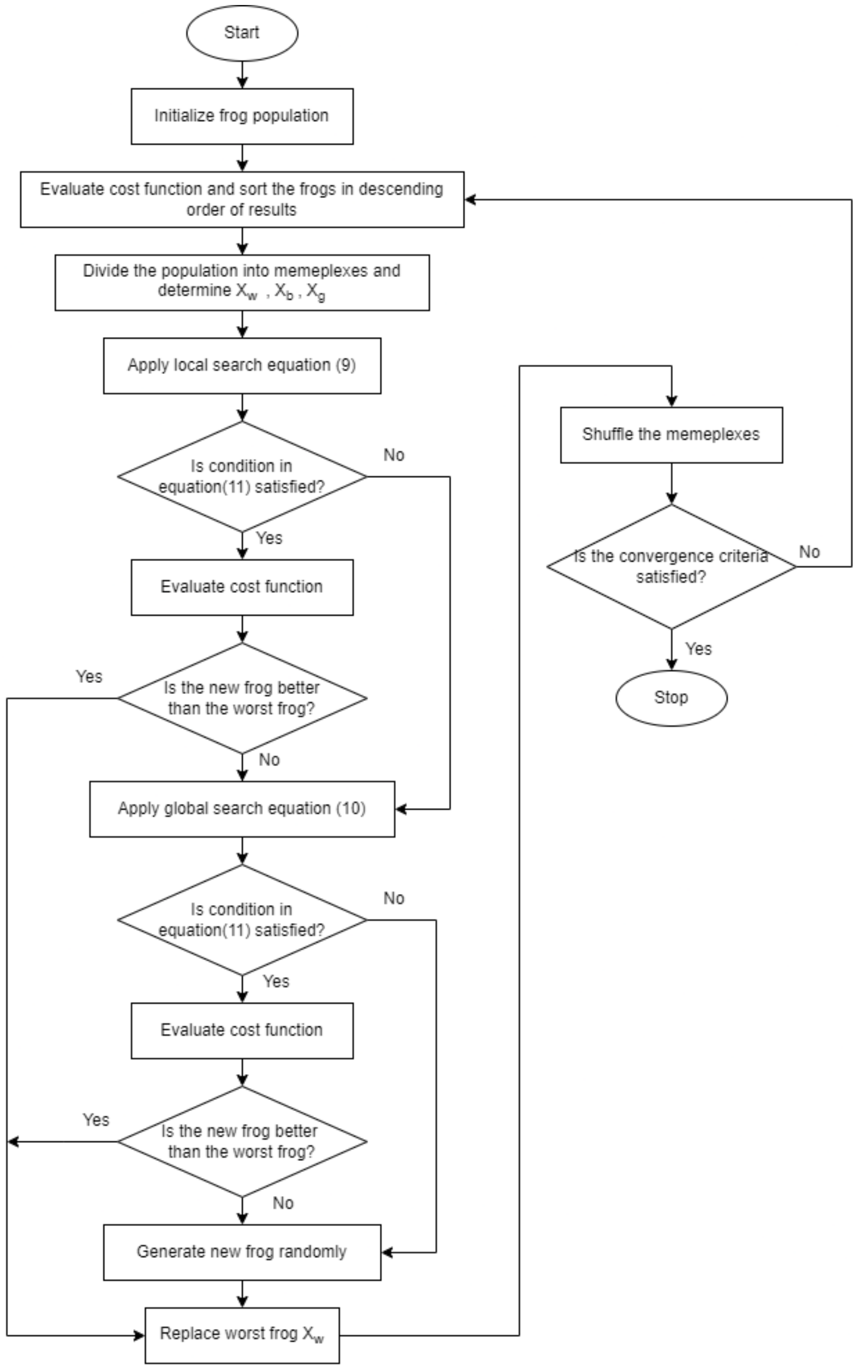

Fig. 2 - Flowchart for modified SFLA algorithm

3. Theory and Calculation

3.1 Benchmarking and Validation

The code for PSO and SFLA was validated using 15 benchmark functions (refer to the Supplementary Materials for the 3D plots), which included both unimodal (functions 7, 1, and 2) and multimodal (functions 6, 9, and 12), functions with many local optima (functions 1, 7-9, 11, 13-14) and many global optima (functions 13 and 15). Each benchmark function was run 30 times, with 1000 iterations each. The total population size for both algorithms was 50 (5 memeplexes with 10 frogs per memeplex for SFLA).

The statistical results for the benchmark functions are given in Table 1. The main focus of this analysis was on the mean and standard deviation of the cost function evaluations since they are indicative of the repeatable optimality of the algorithms. This is especially important because the populations generated for each run of the algorithm differ.

From Table 1, we can see that in general, the mean results obtained using SFLA were better than those obtained through PSO. The exceptions to this observation were functions 11 (5d and 10d), 12, and 14, where the PSO results were better, and function 13, where the mean was the same. Consequently, the general trend observed for standard deviation was that it was lower for SFLA as compared to PSO. The average number of convergence iterations for

SFLA were lesser compared to PSO, except for functions 1, 2 and 5. Conversely, the average run time (for 1000 iterations) for SFLA is higher.

Table 1 - Results of benchmark functions

N.	Function	Range	d	PSO | ω = 0.65, c_1 = 1.65, c_2 = 1.75				SFLA | ω = 1, c_1 = c_2 = 2			
				Avg RT	Avg CI	Mean	Std. Dev.	Avg RT	Avg CI	Mean	Std. Dev.
1	Sphere	[-100, 100]	30	1.1457	999	3.8051E-17	6.7902E-17	8.7681	1000	3.4576E-71	7.4977E-71
		[-10, 10]		1.1803	999	3.8051E-19	6.7902E-19	7.9281	1000	2.4754E-71	7.6592E-71
		[-5.12, 5.12]		1.2557	999	9.9749E-20	1.7800E-19	8.1669	1000	4.4202E-71	2.3782E-70
2	Sum Square	[-100, 100]	30	0.9550	990	3.3333E+02	1.8257E+03	5.9185	1000	1.1498E-65	6.2831E-65
		[-10, 10]		0.7007	990	3.3333E+00	1.8257E+01	6.1128	1000	1.0022E-70	3.7445E-70
		[-5.12, 5.12]		1.1036	990	8.7381E-01	4.7861E+00	6.0267	1000	1.2627E-69	6.8912E-69
3	Matyas	[-10, 10]	2	0.6696	996	1.4622E-97	7.3964E-97	5.6252	996	1.5040E-311	0.0000E+00
4	Booth	[-10, 10]	2	0.6571	261	0.0000E+00	0.0000E+00	6.3799	52	0.0000E+00	0.0000E+00
5	Zakharov	[-5, 10]	10	0.6560	998	2.4123E-32	5.3329E-32	5.8687	1000	3.7042E-98	1.9266E-97
			30	0.6969	996	1.5002E+01	3.1180E+01	6.1667	1000	3.3074E-06	1.5700E-05
6	Beale	[-4.5, 4.5]	2	0.6428	312	5.0805E-02	1.9334E-01	6.4111	86	9.2445E-34	5.0634E-33
7	Easom	[-100, 100]	2	0.6225	137	-1.0000E+00	0.0000E+00	6.6426	21	-1.0000E+00	0.0000E+00
8	Eggholder	[-512, 512]	2	0.6371	223	-8.3256E+02	1.0610E+02	6.2042	138	-8.8937E+02	7.5537E+01
9	Michale-wicz	[0, pi]	2	0.6618	159	-1.8013E+00	9.0336E-16	6.3598	38	-1.8013E+00	9.0336E-16
			5	0.7071	343	-4.5584E+00	1.9100E-01	6.2610	221	-4.4645E+00	1.9075E-01
			10	1.0580	546	-8.8041E+00	5.1623E-01	9.3777	367	-8.6069E+00	5.5608E-01
10	Dixon-Price	[-10, 10]	4	1.0869	396	3.6978E-32	0.0000E+00	8.4646	133	1.1710E-31	1.4504E-31
			10	1.0375	451	6.0000E-01	2.0342E-01	8.5383	265	4.2222E-01	3.2676E-01
			30	0.7108	983	6.6667E-01	3.7383E-05	6.5714	611	6.6667E-01	3.8246E-13
11	Ackley	[-32.768, 32.768]	2	0.5017	255	8.8818E-16	0.0000E+00	5.8666	36	8.8818E-16	0.0000E+00
			5	0.4981	507	1.9540E-15	1.6559E-15	5.8998	141	2.0724E-15	1.7034E-15
			10	0.5163	561	4.6777E-15	9.0135E-16	5.8978	159	4.8490E-01	6.7197E-01
12	Drop-Wave	[-5.12, 5.12]	2	0.4952	143	-1.0000E+00	0.0000E+00	5.9452	82	-9.8725E-01	2.5938E-02
13	Shubert	[-10, 10]	2	0.5047	250	-1.8673E+02	4.4157E-14	5.7148	228	-1.8673E+02	3.2534E-14
		[-5.12, 5.12]		0.5031	149	-1.8673E+02	2.4755E-14	5.7619	29	-1.8673E+02	2.4755E-14
14	Griewank	[-600, 600]	2	0.5010	327	2.4653E-04	1.3503E-03	9.2549	144	6.2457E-03	5.5594E-03
			5	0.5110	617	2.0609E-02	1.2647E-02	7.5310	269	1.2376E-01	8.2825E-02
			10	0.5272	700	7.0055E-02	3.9644E-02	5.8209	273	8.9725E-02	6.1086E-02
15	Cross-in-Tray	[-10, 10]	2	0.5025	127	-2.0626E+00	9.0336E-16	5.7631	20	-2.0626E+00	9.0336E-16

Out of the 15 benchmark functions evaluated, it is evident that 1000 iterations were insufficient to achieve complete convergence for functions 1, 2, 3, and 5. This was the case even after the search space was reduced. Nonetheless, the solutions obtained for these functions were within desirable limits, but there was scope for further improvement if the number of iterations were increased. The only outlier to this observation is the results obtained for function 2 using PSO, even with reduced search space. Apart from this, the results obtained for function 14 (both algorithms) and 6 (using PSO) could have been better. On the other hand, both algorithms were unable to achieve optimality for functions 8 and 9 (10d). Based on the promising results obtained for the benchmark functions, the algorithms were used to attempt the case study.

3.2 Case Study

Figure 3 provides a diagrammatic representation of the speed reducer case study attempted. The original constraints, objective function, and assumptions by [4] can be found in the Supplementary Materials. These equations were simplified and re-written as listed below by [6] and were used in this case study.

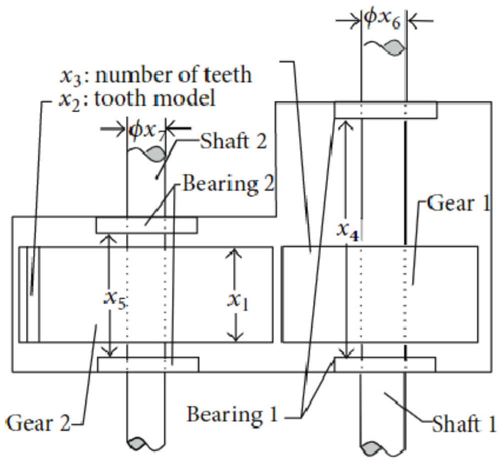

Fig. 3 - Schematic of the Golinski speed reducer [6]

Objective Function:

$$f(x_1,\ldots,x_7) = (0.7854 \times 3.3333)x_1x_2^2x_3^2 + (0.7854 \times 43.0934)x_1x_2^2x_3 - 1.508x_1x_6^2 - 1.508x_1x_7^2 + 7.4777x_6^2 - 7.4777x_7^2 + 0.7854x_4x_6^2 + 0.7854x_5x_7^2$$

Constraints:

$$g_1 = 27x_1^{-1}x_2^{-2}x_3^{-1} - 1 \le 0,$$
$$g_2 = 397.5x_1^{-1}x_2^{-2}x_3^{-2} - 1 \le 0,$$
$$g_3 = 1.93x_4^3x_2^{-1}x_3^{-1}x_6^{-4} - 1 \le 0,$$
$$g_4 = 1.93x_5^3x_2^{-1}x_3^{-1}x_7^{-4} - 1 \le 0,$$
$$g_5 = 745^2x_4^2x_2^{-2}x_3^{-2} - 100^2x_6^6 + (16.9 \times 10^6) \le 0,$$
$$g_6 = 745^2x_5^2x_2^{-2}x_3^{-2} - 85^2x_7^6 + (157.5 \times 10^6) \le 0,$$
$$g_7 = x_2x_3 - 40 \le 0,$$
$$g_8 = 5x_2 - x_1 \le 0,$$
$$g_9 = x_1 - 12x_2 \le 0,$$
$$g_{10} = 1.5x_6 - x_4 + 1.9 \le 0,$$
$$g_{11} = 1.1x_7 - x_5 + 1.9 \le 0,$$

$$2.6 \le x_1 \le 3.6,$$
$$0.7 \le x_2 \le 0.8,$$
$$1.7 \le x_3 \le 28,$$
$$7.3 \le x_4 \le 8.3,$$
$$7.3 \le x_5 \le 8.3,$$
$$2.9 \le x_6 \le 3.9,$$
$$5 \le x_7 \le 5.5$$

Where x_1 = face width, x_2 = module, x_3 = number of pinion teeth, x_4 = length of the first shaft between bearings, x_5 = length of the second shaft between bearings, x_6 = diameter of the first shaft, x_7 = diameter of the second shaft.

The penalty approach employed by [14] was used to deal with the constraints of this optimization problem. The following are the steps involved:

- the cost function and constraints are evaluated for the set of variables obtained by the algorithm;
- if a constraint is violated, the penalty for that constraint is set to the value obtained on evaluating that constraint equation; else the penalty is set to zero. For example, if the evaluation of constraint g_8 is equal to 9, the constraint would be violated, and hence, the penalty for g_8 would be set to 9;
- after all the constraints are evaluated, the penalty for each constraint (if any) is added up and multiplied by a penalty factor R_m, which is chosen on a case-to-case basis. The basic purpose is to prevent the algorithm from converging too early. In cases where the constraint violation is miniscule, larger penalty factors are picked, and vice versa;
- lastly, the product of total penalty and R_m are added to the cost function of that evaluation as shown in equation (12):

$$z = f(x) + (R_m \times \sum penalty) \quad (12)$$

The value of z was used as the cost function value for each evaluation of the objective function. In this way, every time the set of variables violated a constraint, the possibility of that evaluation being the global optimum was reduced, hence ensuring that the global optimum parameter combinations obtained had little to no constraint violation.

4. Results and discussion

4.1 Parameter Optimization

For benchmarking and validation of the code, certain standard values were used for the c_1, c_2, and ω parameters of the modified PSO and SFLA algorithms. Due to the affect c_1, c_2, and ω have on the progression of the algorithm, different combinations of these parameters work well for different search spaces [15, 16].

Table 2. Effect of number of memeplexes and frogs per memeplex on convergence

No.	n	m	m × n	Min Cost	Max Cost	Mean Cost	Std Dev	Avg RT	Avg CI
1	10	2	20	2886.2279	2898.6941	2889.1941	3.9741E+00	3.1562	575
	10	3	30	2886.2279	2891.2402	2886.6852	1.1414E+00	4.4641	743
	10	4	40	2886.2279	2890.5270	2886.5325	9.8403E-01	5.7683	782
	10	5	50	2886.2279	2886.2628	2886.2291	6.3689E-03	7.0996	833
	10	6	60	2886.2279	2886.2280	2886.2279	2.2190E-05	11.9682	799
	10	7	70	2886.2279	2886.2279	2886.2279	7.0253E-10	12.5813	778
	10	8	80	2886.2279	2886.2279	2886.2279	3.6808E-12	14.9407	816
	10	9	90	2886.2279	2886.2279	2886.2279	4.4197E-11	12.6021	847
	10	10	100	2886.2279	2886.2279	2886.2279	4.0868E-11	13.8452	834
2	5	4	20	2886.2279	2886.3430	2886.2348	2.3653E-02	5.4799	309
	5	6	30	2886.2279	2886.2318	2886.2280	7.2008E-04	8.1512	314
	5	8	40	2886.2279	2886.2279	2886.2279	2.6503E-12	15.0238	321
	5	10	50	2886.2279	2886.2279	2886.2279	1.1852E-12	16.3917	327
	5	12	60	2886.2279	2886.2279	2886.2279	1.3978E-12	16.6759	344
	5	14	70	2886.2279	2886.2279	2886.2279	3.3778E-13	19.0712	345
	5	16	80	2886.2279	2886.2279	2886.2279	8.3596E-13	22.2465	350
	5	18	90	2886.2279	2886.2279	2886.2279	1.8882E-13	23.8131	364
	5	20	100	2886.2279	2886.2279	2886.2279	1.1942E-13	26.1906	367

Note: n = number of frogs per memeplex, m = number of memeplexes.

Hence, an experiment was carried out to understand the relation between number of memeplexes, frogs per memeplex, and convergence for the SFLA algorithm. These results are presented in Table 2 for a parameter combination of ω = 1, and $c_1 = c_2 = 2$. The results highlighted that the standard deviation of the cost function evaluations for each set of 30 runs in SFLA reduced with increasing total population size (Table 2). The average run time and number of iterations to achieve converge for 1000 iterations also increased with the increase in total population. Another important observation was that the standard deviation reduced when the number of memeplexes were increased (for the same total population size). The average run time increased as the total population increased, but the time taken for the experimental set with increased number of memeplexes was higher as compared to the ones with lesser number of memeplexes (for the same total population). One interesting observation was that, although the average number of iterations to achieve convergence was increased as the total population increased, the number of iterations required were far lesser than the number required with lesser memeplexes.

From Table 2, it can be noted that the optimal solution is around 2886 (including penalty). An experiment was carried out to select the best combination of parameters for both, PSO as well as SFLA, within the defined ranges for c_1, c_2, and ω. Since the value of c_1 and c_2 should lie between 0 and 2, and w, 0 to 1, this was done with increments of 0.5. The total number of combinations were 75. This experiment was also repeated for different total population sizes to check the effect of population size on the optimal solutions obtained. For SFLA, as per the results obtained in Table 2, the number of memeplexes was increased (with 10 frogs per memeplex). The complete result table for this experiment is given in the Supplementary Materials. Based on the results obtained, suitable combinations of parameters were selected for the modified PSO and SFLA algorithms.

It was observed that whenever any of the three parameters in the combination was set to zero for PSO, the minimum, maximum, and mean value of the cost function evaluations obtained were higher, as compared to combinations that were non-zero. This observation can be visualized from the sharp peaks in Figure 4 (a). A very similar trend can be seen for the standard deviation in Figure 4 (b). From Figure 4 (a) and (b), it is evident that the values of ω, c_1, and c_2 increase from 0, the number of iterations required for the solution to converge is higher. It was observed that as a general trend, as the values for the 3 parameters increases, the average CI required also increases. The elimination method was used to decide the best combination of parameters for modified PSO to solve this case study. This combination was: $\omega = 0.5$, $c_1 = 1.5$ and $c_2 = 1.5$, for a population size of 30.

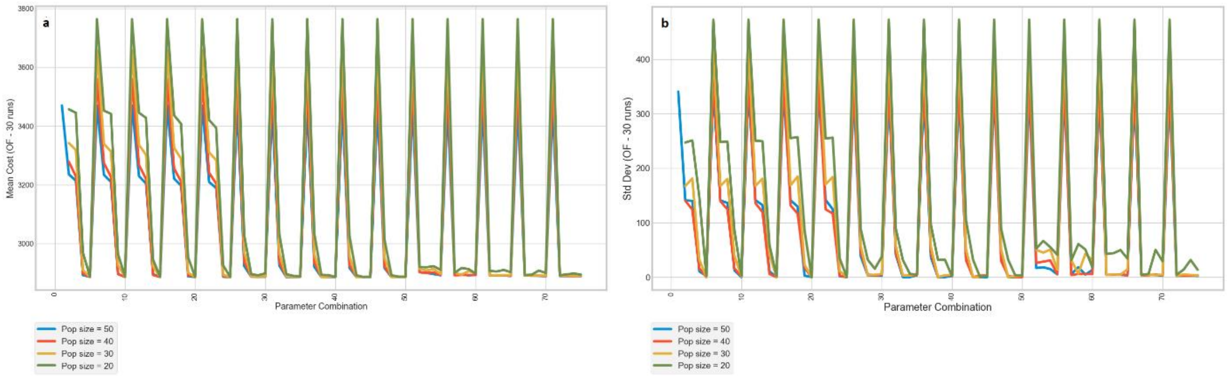

Fig. 4 - Effect of ω, c_1, c_2 on (a) Mean Cost, (b) Standard Deviation for Modified PSO

Note: The values on the x-axis represent the serial number for the parameter combination. Further information can be obtained in the Supplementary Materials.

Analysis of the results for SFLA indicate that for every combination where $\omega < 1$, there was negligible change in the cost function evaluations, standard deviation, average run time, and number of convergence equations required (supplementary materials). For combinations with $\omega = 1$, there is a trend similar to the one observed for PSO, except that the rise in the mean cost function value is more gradual, unlike the sharp peaks observed for PSO (Figure 5 (a)). This trend continues for 3 cycles and then converges once $c_1 \geq 1.5$. It can be noted that, the smaller the total population size, the greater is the cost function evaluation, for the same set of parameters (Figure 5, (a) and (b)). As was the case for modified PSO, the elimination method was used to identify the best combination of parameters for modified SFLA for this case study: $\omega = 1$, $c_1 = 2$ and $c_2 = 0.5$, for a population size of 150 (15 memeplexes with 10 frogs each).

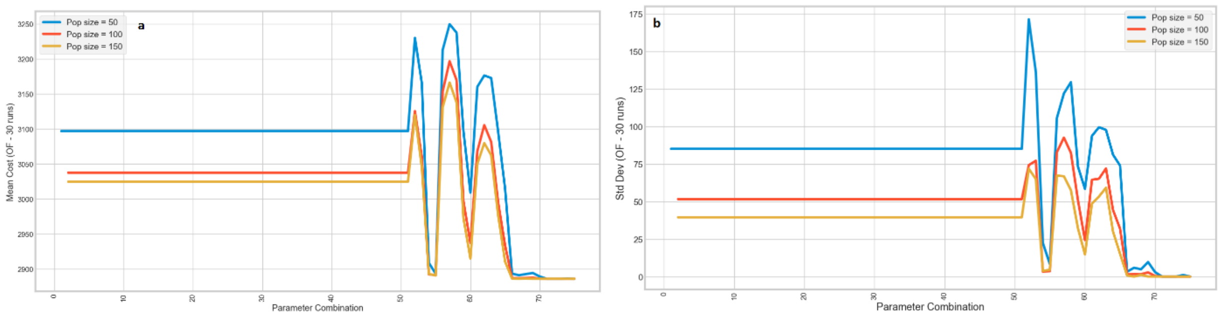

Fig. 5 - Effect of ω, c_1, c_2 on (a) Mean Cost, (b) Standard Deviation for Modified SFLA

Note: The values on the x-axis represent the serial number for the parameter combination. Further information can be obtained in the Supplementary Materials.

4.2 Comparison of Results with Previous Literature

The results of the case study using the modified PSO and SFLA algorithms were the same - 2886.2279 (with penalty) and 2640.9739 (without penalty). The total penalty was 1.2292 for PSO and 1.2263 for SFLA, for a penalty factor (r_m) of 200.

Table 3 gives us a broad comparison of the different reported optimal solutions for the Golinski speed reducer problem obtained by researchers over the years [6,17–26]. The OF and constraint equation values were re-calculated for each of the previous results (Table 4). As is clearly visible in Table 3, the results obtained using the modified PSO and SFLA algorithms (the OF value with the penalty added, i.e., 2886.2279) is one of the best solutions.

Table 3. Comparison of case study variables and OF (with penalty) with previous literature

No	Authors	Algorithm	Variables	OF (with penalty, if any)
1	K'uang J. Ku et al.	Taguchi method	$x_1 = 3.6$, $x_2 = 0.7$, $x_3 = 17$, $x_4 = 7.3$, $x_5 = 7.8$, $x_6 = 3.4$, $x_7 = 5.0$	2876.2200
2	Akhtar et al.	Socio-Behavioural Simulation Model	$x_1 = 3.506122$, $x_2 = 0.700006$, $x_3 = 17$, $x_4 = 7.549126$, $x_5 = 7.859330$, $x_6 = 3.365576$, $x_7 = 5.289773$	3008.1974

3	Rao and Xiong	Mixed Discrete Hybrid Genetic Algorithm (MDHGA)	x_1 = 3.5, x_2 = 0.7, x_3 = 17, x_4 = 7.3, x_5 = 7.8, x_6 = 3.36, x_7 = 5.29	3000.8300
4	Leticia C. Cagnina et al.	Simple Constrained Particle Swarm optimizer (SiC-PSO)	x_1 = 3.5, x_2 = 0.7, x_3 = 17, x_4 = 7.3, x_5 = 7.8, x_6 = 3.350214, x_7 = 5.286683	2996.3482
5a	Jaberipour and Khorram	Proposed Harmony Search Algorithm (PHS)	x_1 = 3.5, x_2 = 0.7, x_3 = 17, x_4 = 7.3, x_5 = 7.71533233833903, x_6 = 3.35021510925684, x_7 = 5.28666403545462	2994.4775
5b		Improving Proposed Algorithm Harmony Search (IPHS)	x_1 = 3.5, x_2 = 0.7, x_3 = 17, x_4 = 7.3, x_5 = 7.71599501113801, x_6 = 3.35025375091328, x_7 = 5.28690759750734	2994.9000
6	Li and Papalabros	Production System for Global Knowledge	x_1 = 3.5, x_2 = 0.7, x_3 = 17, x_4 = 7.3, x_5 = 7.71, x_6 = 3.35, x_7 = 5.29	2994.4000
7	Tosserams et al.	Augmented Lagrangian Decomposition Method	x_1 = 3.5, x_2 = 0.7, x_3 = 17, x_4 = 7.3, x_5 = 7.72, x_6 = 3.35, x_7 = 5.29	2996.6458
8	Lu & Kim	Regularized Inexact Penalty Decomposition Algorithm	x_1 = 3.5, x_2 = 0.7, x_3 = 17, x_4 = 7.3, x_5 = 7.670396, x_6 = 3.542421, x_7 = 5.245814	3019.5834
9	Huang C	Geometric Programming (GP)	x_1 = 3.495652, x_2 = 0.7000002, x_3 = 17, x_4 = 7.30000007, x_5 = 7.7120386, x_6 = 3.343372, x_7 = 5.285352	2990.1244
10	Lin M. et al.	Convexification strategies and piecewise linearization methods	x_1 = 3.5, x_2 = 0.7, x_3 = 17, x_4 = 7.3, x_5 = 7.715319, x_6 = 3.350282, x_7 = 5.286654	2994.4719
11a	**Golinski (Original case study)**	Crude Monte-Carlo	x_1 = 4.4, x_2 = 0.6, x_3 = 17, x_4 = 7.3, x_5 = 8.1, x_6 = 3.4, x_7 = 5	2236.3500
11b		Stray Process	x_1 = 3.6, x_2 = 0.7, x_3 = 18, x_4 = 6.6, x_5 = 8.2, x_6 = 2.8, x_7 = 5.2	2247.7900
A1	**Our solutions**	Modified PSO	x_1 = 2.6, x_2 = 0.7, x_3 = 17, x_4 = 7.3, x_5 = 7.715319911, x_6 = 3.350214666, x_7 = 5.286654465	2886.2279
A2		Modified SFLA	x_1 = 2.6, x_2 = 0.7, x_3 = 17, x_4 = 7.3, x_5 = 7.715319911, x_6 = 3.350214666, x_7 = 5.286654465	2886.2279

Note: OF represents the evaluation of the Objective Function – (with penalty values added for No. A1 and A2). x_1 to x_7 represent the values for each of the 7 variables.

The only two solutions with comparable results were those obtained using the Taguchi Method by [17] and the Crude Monte-Carlo and Stray Process algorithms by [4]. However, on closer observation, it is obvious from Table 4 that the constraint violations for these algorithms are far greater than the violations using the modified PSO and SFLA algorithms in the present work. Also, from Table 4, it is evident that the cost function value presented by [4] does not match the results presented in their paper. Based on these observations, the values obtained in the present work using modified PSO and SFLA as relatively more optimal.

Table 4. Comparison of results of re-calculated OF and constraint equations (values obtained from previous literature)

No	f(x)	Constraints
1	2876.219475	g(1) = -0.09964, g(2) = -0.220276, g(3) = -0.527868, g(4) = -0.876856, g(5) = -1.5833E+06, **g(6) = 4.4848E+07**, g(7) = -28.1, g(8) = -0.1, g(9) = -4.8, g(10) = -0.3, g(11) = -4.0000E-01
2	3008.19744	g(1) = -0.075548, g(2) = -0.199413, g(3) = -0.456175, g(4) = -0.899442, g(5) = -4.6162E+05, g(6) = -5.5031E+05, g(7) = -28.099898, g(8) = -0.006092, g(9) = -4.89395, g(10) = -0.600762, g(11) = -1.4058E-01
3	3000.959715	g(1) = -0.073915, g(2) = -0.197999, g(3) = -0.504981, g(4) = -0.901719, g(5) = -3.0203E+05, g(6) = -5.9471+05, g(7) = -28.1, g(8) = 0, g(9) = -4.9, g(10) = -0.36, g(11) = -8.1000E-02
4	2996.347849	g(1) = -0.073915, g(2) = -0.197999, g(3) = -0.499172, g(4) = -0.901472, **g(5) = 2.0410E+01**, **g(6) = 4.1132E+01**, g(7) = -28.1, g(8) = 0, g(9) = -4.9, g(10) = -0.374679, g(11) = -8.4649E-02
5a	2994.477531	g(1) = -0.073915, g(2) = -0.197999, g(3) = -0.499173, g(4) = -0.904644, g(5) = -1.3579E+01, g(6) = -1.7125E+03, g(7) = -28.1, g(8) = 0, g(9) = -4.9, g(10) = -0.374677, g(11) = -1.8993E-06
5b	2994.656655	g(1) = -0.073915, g(2) = -0.197999, g(3) = -0.499196, g(4) = -0.904637, g(5) = -1.1976E+03, g(6) = -4.5280E+04, g(7) = -28.1, g(8) = 0, g(9) = -4.9, g(10) = -0.374619, g(11) = -3.9665E-04
6	2996.425995	g(1) = -0.073915, g(2) = -0.197999, g(3) = -0.499044, g(4) = -0.905082,

		g(5) = 6.5765E+03, g(6) = -6.0018E+05, g(7) = -28.1, g(8) = 0, g(9) = -4.9, g(10) = -0.375, **g(11) = 9.0000E-03**
7	2996.645783	g(1) = -0.073915, g(2) = -0.197999, g(3) = -0.499044, g(4) = -0.904712, **g(5) = 6.5765E+03**, g(6) = -5.9959E+05, g(7) = -28.1, g(8) = 0, g(9) = -4.9, g(10) = -0.375, g(11) = -1.0000E-03
8	3019.583344	g(1) = -0.073915, g(2) = -0.197999, g(3) = -0.599338, g(4) = -0.903348, g(5) = -6.8015E+06, **g(6) = 7.1687E+06**, g(7) = -28.1, g(8) = 0, g(9) = -4.9, g(10) = -0.086369, g(11) = -6.0000E-07
9	2990.124384	g(1) = -0.072764, g(2) = -0.197001, g(3) = -0.49506, g(4) = -0.904672, **g(5) = 2.0860E+05**, **g(6) = 2.3282E+05**, g(7) = -28.099997, **g(8) = 0.004349**, g(9) = -4.90435, g(10) = -0.384842, **g(11) = 1.8486E-03**
10	2994.48791	g(1) = -0.073915, g(2) = -0.197999, g(3) = -0.499213, g(4) = -0.904644, g(5) = -2.0633E+03, **g(6) = 8.3184E+01**, g(7) = -28.1, g(8) = 0, g(9) = -4.9, g(10) = -0.374577, **g(11) = 4.0000E-07**
11a	2672.019394	**g(1) = 0.002674,** g(2) = -0.131671, g(3) = -0.44918, g(4) = -0.839109, g(5) = -1.5078E+06, **g(6) = 4.4959E+07**, g(7) = -29.8, g(8) = -1.4, g(9) = -2.8, g(10) = -0.3, g(11) = -7.0000E-01
11b	3049.97544	g(1) = -0.14966, g(2) = -0.304506, g(3) = -0.283549, g(4) = -0.884491, **g(5) = 1.1221E+07**, **g(6) = 1.4892E+07**, g(7) = -27.4, g(8) = -0.1, g(9) = -4.8, g(10) = -0.5, g(11) = -5.8000E-01
A1	2640.97393	**g(1) = 0.246653,** **g(2) = 0.0796174,** g(3) = -0.499172, g(4) = -0.904644, g(5) = -7.0781E-08, **g(6) = 2.9802E-07**, g(7) = -28.1, **g(8) = 0.9**, g(9) = -5.8, g(10) = -0.374678, g(11) = -7.5495E-15
A2	2640.97393	**g(1) = 0.246653,** **g(2) = 0.0796174,** g(3) = -0.499172, g(4) = -0.904644, g(5) = -7.0781E-08, **g(6) = 2.9802E-07**, g(7) = -28.1, **g(8) = 0.9**, g(9) = -5.8, g(10) = -0.374678, g(11) = -7.5495E-15

Note: f(x) is the evaluation of the OF (Objective Function) – without penalty values added for No. A1 and A2. g(1) to g(11) represents the evaluation of the 11 constraints. The cells highlighted in bold text represent the constraints that were violated.

The percentage difference in the results obtained using modified PSO and SFLA (without penalty) in comparison with previous results is shown in Table 5.

Table 5. Percentage improvement in results

No.	Author(s)	OF (without penalty)	% Improvement
1	K'uang J. Ku et al.	2876.2200	8.1790%
2	Akhtar et al.	3008.1974	12.2074%
3	Rao and Xiong	3000.8300	11.9919%
4	Leticia C. Cagnina et al.	2996.3482	11.8602%
5a	Jaberipour and Khorram	2994.4775	11.8052%
5b		2994.9000	11.8176%
6	Li and Papalabros	2994.4000	11.8029%
7	Tosserams et al.	2996.6458	11.8690%
8	Lu and Kim	3019.5834	12.5385%
9	Huang	2990.1244	11.6768%
10	Lin et al. (2012)	2994.3410	11.8012%
11	Lin et al. (2013)	2994.4719	11.8050%
12a	Dr Jan Golinski (Original case study)	2236.3500	-18.0931%
12b		2247.7900	-17.4920%
12a*		2672.0194	1.1619%
12b*		3049.9754	13.4100%
A1	Modified PSO	2640.9739	
A2	Modified SFLA	2640.9739	

*Note: * indicates the actual OF values obtained after re-calculating results*

The results of this project indicate that there is a negative difference in the cost function value (18.0931%) as compared to the result obtained by [4] using the Crude Monte-Carlo algorithm, and a 17.4920% difference in comparison with the Stray Process result. But as mentioned earlier, the values of the OF evaluations presented by Golinski do not match the re-calculated values. Based on these re-calculated values, the percentage difference between Golinski's results and the results obtained in this project is 1.1619% and 13.41% for both algorithms respectively. Apart from the results presented by Golinski, the smallest percentage improvement is 8.1790%, in comparison with the Taguchi method suggested by [17]. A total of 4 constraints (constraints 1, 2, 6, and 8) were violated by the combination of parameters obtained using the modified PSO and SFLA algorithms. Since the violation in the constraints are negligible, the design of the speed reducer can be considered satisfactory:

- constraint 1 (Bending condition) violation: 0.246653;
- constraint 2 (Compressive stress limitation) violation: 0.079617;
- constraint 6 (Stress condition for shaft 2) violation: 0.00000029802;
- constraint 8 (Relative face width condition) violation: 0.9.

Conclusions

Modified PSO and SFLA are both powerful nature-inspired algorithms that can obtain optimal results for a variety of benchmark functions (unimodal, multimodal, multiple local and global optima). However, it is important to note that different parameter combinations work better for different optimization problems with different search spaces.

The results obtained using modified PSO and SFLA described in the present work had an 8.1790% reduction in cost function evaluation as compared to the Taguchi method by [17], 1.1619% reduction compared to the Crude Monte-Carlo method and 13.41% reduction compared to the Stray Process used by [4], and around an 11% reduction compared to results obtained by other researchers. Modified SFLA generally takes lesser number of convergence iterations (CI) on average as compared to modified PSO, but the average run time (RT) for the same number of iterations (1000) is greater for modified SFLA. So, it's essentially a trade-off between average CI and average RT.

Further, the results for variables x_1 to x_7 obtained using modified PSO and SFLA can be verified by developing CAD models and conducting finite element analysis (FEA). In this way, the minor constraint violations can be evaluated to check the degree of damage caused by them.

As per the No Free Lunch theorem, no single algorithm is best suited for all optimization problems. Along the same lines, certain nature-inspired algorithms work better than others for speed reducer problems. The algorithms with promising results can be analysed to understand their components/mechanisms that support their optimal results. For example, the inertia weight factor in PSO is attributed to its success in a variety of applications. Similarly, in memetic algorithms like SFLA, since information can be directly transmitted among frogs within the same iteration instead of waiting for the next one, the propagation of optimal memes is faster, which contributes to the faster convergence observed in this algorithm. For future work, these algorithm-specific mechanisms could be identified and combined in the form of a hybrid algorithm that could be used to solve families of similar optimization problems.

References

[1] Zolfaghari A., Goharimanesh M., Akbari A.A. Optimum design of straight bevel gears pair using evolutionary algorithms //Journal of the Brazilian Society of Mechanical Sciences and Engineering, 39, 2017, 2121–2129

[2] Qin Z., Wu Y.T., Lyu S.K. A Review of recent advances in design optimization of gearbox //International journal of precision engineering and manufacturing, 19, 2018, 1753–1762

[3] Dalavi A.M., Gomes A., Javed Husain A. Bibliometric analysis of nature inspired optimization techniques //Comput Ind Eng, 169, 2022,108161

[4] Golinski J. Optimal synthesis problems solved by means of nonlinear programming and random methods, Journal of Mechanisms 5,1970, P. 287–309. https://doi.org/10.1016/0022-2569(70)90064-9.

[5] Ray T. Golinski's speed reducer problem revisited //AIAA Journal, 41, 2003, P. 556–558

[6] Lin M.H., Tsai J.F., Hu N.Z., Chang S.C. Design optimization of a speed reducer using deterministic techniques //Math Probl Eng, 2013, 2, P.1-7

[7] Kennedy J., Eberhart R. Particle Swarm Optimization, 1995.

[8] Shi Y., Eberhart R. Modified particle swarm optimizer, Proceedings of the IEEE Conference on Evolutionary Computation, ICEC, 1998, P. 69–73

[9] Heris M.K. Particle Swarm Optimization (PSO) in MATLAB - Video Tutorial, Yarpiz, 2016.

[10] Eusuff M.M., Lansey K.E. Optimization of water distribution network design using the shuffled frog leaping Algorithm // J Water Resour Plan Manag, 129, 2003. P. 210–220

[11] Elbeltagi E., Hegazy T., Grierson D. A modified shuffled frog-leaping optimization algorithm: Applications to project management, Structure and Infrastructure Engineering 3, 2007, P. 53–60. https://doi.org/10.1080/15732470500254535.

[12] Dalavi A.M., Pawar P.J., Singh T.P. Tool path planning of hole-making operations in ejector plate of injection mould using modified shuffled frog leaping algorithm //J Comput Des Eng, 3, 2016, P. 266–273

[13] Heris M.K. Shuffled Frog Leaping Algorithm in MATLAB, Yarpiz, 2015

[14] Parsopoulos K., Vrahatis M.N. Particle Swarm Optimization Method for Constrained Optimization Problems, in: P. Sincak, J. Vascak, V. Kvasnicka, J. Pospichal (Eds.), Intelligent Technologies: Theory and Applications: New Trends in Intelligent Technologies, IOS Press (Frontiers in Artificial Intelligence and Applications series), Fairfax, VA, U.S.A., 2002: P. 1–7.

[15] Rao R.V., Savsani V.J. Mechanical Design Optimization Using Advanced Optimization Techniques, Springer-Verlag London, 2012

[16] Van Den Bergh F., Engelbrecht A.P. A study of particle swarm optimization particle trajectories //Inf Sci (N Y), 176, 2006, P. 937–971

[17] Ku K.J., Rao S.S., Chen L. Taguchi-aided search method for design optimization of engineering systems //Engineering Optimization 30, 1998, P. 1–23

[18] Akhtar S., Tai K., Ray T. A socio-behavioural simulation model for engineering design optimization //Engineering Optimization 34(4), 2002, P.341–354

[19] Rao S.S., Xiong Y. A hybrid genetic algorithm for mixed-discrete design optimization, //Journal of Mechanical Design, Transactions of the ASME 127, 2005, P. 1100–1112

[20] Tomassetti G., Cagnina L. Particle swarm algorithms to solve engineering problems: A comparison of performance, Journal of Engineering, 2023, P. 1–13

[21] Jaberipour M., Khorram E. Two improved harmony search algorithms for solving engineering optimization problems, Undefined 15, 2010, P.3316–3331

[22] Li H.L., Papalambros W. A Production System for Use of Global Optimization Knowledge //Journal of Mechanisms, Transmissions, and Automation in Design, 107, 1985, P.277–284

[23] Tosserams S., Etman L.F.P., Rooda J.E. An augmented Lagrangian decomposition method for quasi-separable problems in MDO //Structural and Multidisciplinary Optimization, 34, 2007, P. 211–227

[24] Lu S., Kim H.M. A Regularized inexact penalty decomposition algorithm for multidisciplinary design optimization problems with complementarity constraints // Journal of Mechanical Design, Transactions of the ASME, 2010, P. 0410051–04100512

[25] Huang C.H. Engineering design by geometric programming //Math Probl Eng, 2013,

[26] Lin M.-H., Tsai J.-F., Wang P.-C. Solving Engineering optimization problems by a deterministic global optimization approach //Applied Mathematics & Information Sciences, 2012, P. 1101–1107.

Information of the authors

Amol Dalavi, PhD, assistant professor, Symbiosis Institute of Technology, Pune, India
e-mail: amol.dalavi@sitpune.edu.in

Alyssa Gomes, BTech student, Symbiosis Institute of Technology, Pune, India

Aaliya Husain, BTech student, Symbiosis Institute of Technology, Pune, India

DOI 10.52209/2706-977X_2024_2_91 **IRSTI 55.09.29** **UDC 620.178.193.16**

Wear Resistance Criteria for Various Types of Wear

Seitkazenova K.K, Pechersky V.N., Arapov B.R., Myrzaliev D.S., Kholmakhanov B.S.*
M. Auezov South Kazakhstan University, Shymkent, Kazakhstan
*corresponding author

Abstract. The behavior of the material under cavitation and abrasive wear is considered. An analysis of easily determined wear resistance criteria is given. It has been shown that the resistance of metals to fracture under micro-impact loading is determined not by ordinary mechanical characteristics, but by the strength of individual micro-sections or structural components. And with cavitation erosion, corrosion makes a significant contribution, which is not taken into account when determining mechanical characteristics. The prospects for assessing the erosion resistance of materials using energy criteria are shown, since their specific values depend on factors characterizing the system that is under external influence: the stress state pattern of the wear layers, the deformation rate, the micro- and submicrostructure of the deformed volumes, as well as the cyclic of the external loading.

Keywords: abrasive (hydroabrasive) wear, cavitation erosion, wear resistance criterion, energy criterion, material destruction, structure of materials

Introduction

Cavitation, abrasive, and water-abrasive wear is one of the reasons for reducing the reliability of ship equipment, turbine blades of power plants, various pumping equipment, internal combustion engine parts and aircraft.

The criteria for the wear resistance of materials during cavitation, abrasive (water abrasive) wear are taken, both individually and in complexes, to be the mechanical, physicochemical and other properties of deformable volumes of materials, which (according to some scientists) best resist the destructive effects of the external environment on them [1-3] .When studying the patterns of these types of wear, numerous attempts were made to establish the relationship between wear and the properties of wear materials. At the same time, it was proposed to use a significant number of simple, easily determined and more complex parameters as a criterion for wear resistance.

Depending on the level of energy of external influence during wear, the wear resistance of samples with different hardness, even of the same grade of steel, not to mention materials with sharply different microstructures, can depend on various mechanical properties: hardness and the ratio of tensile strength to yield strength: H and ${}^{\sigma_u}/_{\sigma_{0.2}}$, elastic modules E and G, etc. However, none of these characteristics, as well as indicators of standard plastic properties, unambiguously determine the wear resistance of materials in a fairly wide range of changes in external energy levels. Considering the comparative simplicity of determining the standard mechanical properties of materials, such a characteristic as hardness H can be used as a particular criterion for assessing wear resistance for known levels of external loading energy for materials that are similar in microstructure and properties.

Studies have shown that in materials with different hardness and microstructure, the processes of accumulation of specific energy E_u, sufficient for the destruction of deformable volumes, have their own characteristics. Irreversible structural changes preceding the stage of preliminary destruction will occur through various mechanisms [4]. And the depth of the plastically deformed zone, according to modern physical and mechanical models, determines the large-scale levels of deformation and subsequent destruction (wear) of materials.

If we consider abrasive (water abrasive) wear and cavitation erosion, then they have a lot in common. Cavitation creates high pressures on wear surfaces and causes complex physical and chemical processes. What is common is the cyclical and dynamic nature of external loading, the locality of elastic-plastic deformations in zones of impact of abrasive particles and micro-jet of liquid, the random (stream) nature of external influence and the wave nature of energy transfer in deformable material objects.

1. Research methodology

A general criterion for wear resistance should take into account the characteristics of the destruction of materials under single and repeated external force, take into account the effects associated with the pulsed nature of loading, be sensitive to structural changes occurring in materials with different microstructures during wear and, finally, should reflect the uniform saturation of the wear layers internal energy. In this formulation of the problem, expressing the general criterion in analytical form is extremely difficult. However, modern achievements in metal physics, fracture mechanics of continuous media, dislocation theory and a number of other sciences, together with physical and mechanical research methods, now make it possible to approach the solution of this problem.

2. Results and discussion

In order to identify conditions sufficient for the onset of cavitation erosion, a series of samples made of soft materials ($\sigma_т \leq$ 300 MPa) were tested: steel 1010, 1015, alloys based on aluminum composition (Al + 5.4% Mg) and tin bronze composition (Cu +7% Sn+5% Zn) on impact erosion stand at a speed of impact of a water jet with the surface of the samples $\vartheta \leq$ 40 m/s. For the above materials, criterion dependence was established:

$$\vartheta_i \sim \vartheta_{cr} = 0{,}53\sqrt{\sigma_m}, \qquad (1)$$

in which ϑ_{cr} is the jet speed, less than which there is no erosion on the surface of the material, and the jet pressure corresponds to the surface fatigue limit.
Raising the right and left sides of the last relation to the third power and considering the proportionality

$$\vartheta_{cr}^2 \sim E_u \sim \sigma_{0.2}$$

to be valid, were E_u - specific energy intensity, we obtain the relations:

$$\Delta V \sim \vartheta_i^3 \big/ \sigma_{0.2} \cdot \vartheta_{cr} \sim E_{in} \cdot \vartheta_i \big/ E_u \cdot \vartheta_{cr}, \qquad (2)$$

which indicate the prospects of using structural and energy criteria for the wear resistance of materials for any type of erosion.

The condition for the onset of cavitation-erosive wear during hydrodynamic cavitation, obtained earlier [5] in the form of a relation:

$$K_E = \rho_t / 0{,}5\rho_l \cdot \vartheta_x^2 = const, Re^{1/3} \ , \qquad (3)$$

where K_E is the number of beginning erosion; ρ_l is the fluidity pressure of the material during cavitation pulses; Re is the Reynolds number, by analogy it is easily converted into a fairly accurate wear equation, which, in contrast to (1), takes into account the friction path of the fluid flow along the wear surface to the power of 0.5, i.e. $\sqrt{L_{fr}}$, which is consistent with the damped nature of the kinetic curves of cavitation erosion of materials observed in practice.
After taking into account the friction path, volumetric losses of materials are determined by the equation:

$$\Delta V \sim E_{in}\vartheta_i\, L_{fr}^{1/2} / E_U \vartheta_{cr} \ , \qquad (4)$$

The validity of expression (3) is confirmed by the results of numerous experimental studies, in particular, works [6,7] and [5], which indicates the correctness of energy relations (2) and (3).

Attempts to connect the amount of cavitation wear with one of the mechanical characteristics of materials should be considered unsuccessful.This is explained, on the one hand, by the fact that the resistance to metal destruction under micro-impact loading is determined not by ordinary mechanical characteristics, but by the strength of individual micro-sections or structural components, and on the other hand, by the fact that during cavitation exposure in aggressive environments, along with the mechanical factor, the wear process can have a great influence on the corrosion factor, which conventional mechanical characteristics do not take into account.

Considering the direct dynamic penetration of a spherical abrasive particle into a less hard wear material and considering the volume of holes formed per unit time on a deformable surface to be directly proportional to the volume of wear products, it is not difficult to obtain an approximate expression for estimating volumetric wear.

$$\Delta V \sim \left(\frac{E_{in}}{p_Y}\right)^{3/2} \cdot \frac{(\pi D_a)^{1/2}}{A_N} \cdot N \ , \qquad (5)$$

whereE_{in} - energy of an individual abrasive particle with diameter D_a;
p_Y– dynamicyield pressure of the material;
A_N– nominal contact area at maximum penetration particles;
N – number of impacts of abrasive particles.

The denominator of equation (5) contains the specific energy of deformation, which is proportional top_Y - dynamic yield pressure of the material. Therefore, the relative wear resistance of metals under the impact of abrasive particles can be determined by the relation:

$$k_{\Delta V} = \frac{\Delta V_{ref}}{\Delta V_i} = \left(\frac{E_{Ui}}{E_{Uref}}\right)^{3/2}, \qquad (6)$$

whereE_u is the specific energy of deformation; indices *i*and *ref*to the test and reference material respectively.

Comparing the result obtained in Figure 1 with the experimental data given in [8-11], one can be convinced that the wear resistanceof carbon tool steel (0.7%C) and alloy wear-resistant steel during impact-abrasive wear depends on the specific energy intensity, to the power of 3/2.

Considering that the speed and impact energy are interrelated and at the same time, expression (5) with linear wear kinetics can be given the following form:

$$\Delta V = const_3 \frac{E_{in}\vartheta}{E_U \vartheta_{cr}} N, \quad (7)$$

whereϑ_{cr} - critical speed of blow causing destruction of material at N_{cr} = 1 in specific conditions of tests;

E_U – the critical strain power density characterizing wear resistance of materials;

N – number of external dynamic actions.

Wear ΔG^{-1},1|g

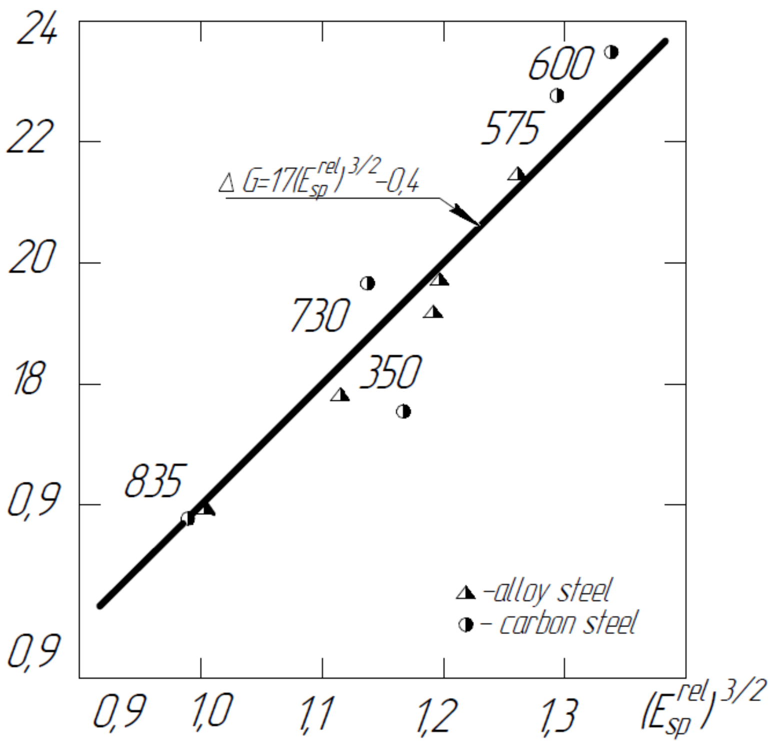

Specific energy intensity, $(E_U^r)^{3/2}$

Fig.1. – Dependence of wear resistance of steels during impact-abrasive wear of carbon tool steel when tested on the ST-4 sclerometer [6] and alloy wear-resistant steel on the MINE and GP installation [4]. Near the experimental points, the hardness of the samples is Vickers

Conclusions

Thus, an analysis of modern ideas about the criteria for wear resistance of materials and dependencies [5-7] indicate the prospects of developing a structural-energy model of water-abrasive wear.

It seems quite reasonable and promising to use specific energy intensity and latent energy of hardening as parameters that determine the wear resistance of materials, since their specific values depend on the pattern of the stress state of the wear layers, the rate of deformation, the micro- and sub microstructure of the deformed volumes, as well as on the cyclic of external loading.

Numerical values of the energy criterion for wear resistance of materials can be obtained in two ways:

- as a result of determining the limiting properties of materials and the degree of energy saturation of wear layers;

- when determining the properties of materials averaged by wear volumes, for example, micro hardness and degree of plastic deformation, reflecting the state of these volumes under specific external loading conditions with a steady wear process.

It should be noted that over the past few decades, the search for sufficiently physically based, objective and workable criteria for wear resistance and durability of materials has not been successful. This means that at present there are no reliable methods for calculating the behavior of materials under abrasive and cavitations' erosion. A similar situation occurs with other types of wear. These unsolved problems, as before, force us to use the results of labor-intensive and, as a rule, expensive laboratory and bench tests.

A general criterion for wear resistance should take into account the characteristics of the destruction of materials under single and repeated external force, take into account the effects associated with the pulsed nature of loading, be sensitive to structural changes occurring in materials with different microstructures during wear and, finally, should reflect the uniformity of saturation of wear layers internal energy.

It seems quite reasonable and promising to use a structural-energy model of cavitation and water-abrasive wear, the parameters of which depend on the pattern of the stress state of the worn layers, the rate of deformation, the micro- and sub microstructure of the deformed volumes, as well as on the cyclic of external loading.

References

[1] Tsvetkov Yu.N. Cavitation wear of metals and equipment. – SPb.: Publishing House of SPbGPU, 2003. - 154 p.
[2] Bykov D.L. Method of structural-energy analysis of the stress-strain state of viscoelastic materials // Vestn. Moscow State University. Ser. 1. Mathematics, mechanics, No. 1, 2006. - P. 59-62.
[3] Vinogradov V.N., Sorokin G.M., Kologninov M.G. Abrasive wear. – M.: Mechanical Engineering, 1990. - 224 p.
[4] Vladimirov V.I. The physical nature of the destruction of metals. – M.: Metallurgy, 1984. - 280 p.
[5] Eisenberg P., Preiser S., Thiruvengadam A., On the Mechanism of Cavitation Damage and Methods of Protection – Transactions of SNAME, 2005, vol. 73.
[6] Pogodaev L.I. Kuzmin V.N. Structural and energy models of reliability of materials and machine parts. – St. Petersburg: Academy of Transport of the Russian Federation, 2006. - 608 p.
[7] Seytkazenova K.K., Myrzaliev D.S., Suendykova M.M. Asylbek M., Ergali K.E. Analysis of wear resistance of materials during cavitation depending on mechanical and kinetic characteristics.News of higher educational institutions //Textile industry technology, No. 5 (389), 2020. – P.33-39
[8] Pogodaev L.I. Wear resistance of materials and machine parts during waterjet and cavitation wear: dissertation. doc. tech. Sciences. – M.: MINKh and State Enterprise named after I.M.Gubkina, 1979. – 534 p.
[9] Pogodaev L. I., Kuzmin A. A. Erosion of materials and ship technical means in inhomogeneous liquid and gaseous media. - St. Petersburg: University of Water Communications, 2004. - 378 p.
[10] Pogodaev L.I., TsvetkovYu.N., Golubev N.F. Dependence of wear resistance and durability of materials under micro-impact loading on the mechanical properties of the surface // Problems of mechanical engineering and machine reliability, No. 3, 1977. – P. 40-51.
[11] Springer J. S. Erosion under the influence of liquid drops - M.: Mechanical engineering, 1981. - 200 p.

Information of the authors

Seitkazenova Kazira Kameshovna, d.t.s., professor, M.Auezov South Kazakhstan University
e-mail: kseitkazi@mail.ru

Pechersky Vladimir Nikolaevich, d.t.s., professor, M.Auezov South Kazakhstan University
e-mail: vn-pecherskiy@mail.ru

Arapov Batyrbek Rakhmetovich, d.t.s., professor, M.Auezov South Kazakhstan University
e-mail: b.arapov@rambler.ru

Myrzaliev Darkhan Saparbaevich, c.t.s., associate professor, M.Auezov South Kazakhstan University
e-mail: darkhan-m7@mail.ru

Kholmakhanov Bekzhan Saparali ugli, master student, M. Auezov South Kazakhstan University
e-mail: bekzhankalmakhan@gmail.com